A Study of Methodology and Technology for Wireless Monitoring of Blood Pressure inside a Stent

by

Daniel S. Brox

BSc, University of British Columbia, 2005

M. Eng., California Institute of Technology, 2008

A THESIS SUBMITTED IN PARTIAL FULFILLMENT

OF THE REQUIREMENTS FOR THE DEGREE OF

DOCTOR OF PHILOSOPHY

in

The Faculty of Graduate and Postdoctoral Studies

(Electrical and Computer Engineering)

THE UNIVERSITY OF BRITISH COLUMBIA

(Vancouver)

July, 2014

Abstract

This thesis presents research on systems for wirelessly monitoring blood pressure inside a vascular stent. Such systems are of interest because changes in the blood pressure gradient across a stent are indicative of a blockage caused by growth of scar tissue (restenosis). No cheap and non-invasive method for detecting the onset of restenosis currently exists, and in-stent wireless blood pressure monitoring may provide a solution.

In this work, several monitoring methods are explored. The first utilizes a specially designed stent integrated with a capacitive pressure sensor to form a pressure sensitive inductor-capacitor (LC) resonant circuit (tank) with wireless sensing capability. This approach follows previous work successful in producing a proof-of-principle prototype, but makes several modifications directed at achieving clinical relevance. A custom designed inductive stent and capacitive pressure sensor are developed, and new integration techniques are explored. *In vitro* resonant frequency responses of integrated devices with applied pressure are measured in the range of 50 - 200 ppm/mmHg.

Device characterization reveals reader-device communication range, sensor performance variation, and stent mechanical reliability as areas of concern. Therefore, a dedicated study of the wireless range achievable with inductive stent monitoring and related monitoring approaches is undertaken, finding a maximum read range of 2.75 cm for an inductive stent in air. A surface micromachined capacitive pressure sensor is developed to improve upon the original sensor, and a miniaturized monitoring device formed by integrating this sensor with a micro-inductor is proposed as a means of avoiding wiring problems and expansion non-uniformities encountered when utilizing inductive stents.

Finally, as an alternative route to increasing wireless sensing range and resolution, a third system design approach employing a complementary metal-oxide-semiconductor (CMOS) integrated circuit (IC) is explored An IC is designed to mount on a stent to read and transmit pressure information from a micro-electro-mechanical systems (MEMS) pressure sensor. The IC may be driven by using the stent as an antenna to harvest power from an external radio frequency (RF) transmitter. Characteristics of the antenna-IC interface are studied by electromagnetic modeling and circuit simulation.

Preface

I contributed to the publication of the following journal and conference papers over the duration of my doctoral research.

Journal papers:

1. D. Brox, A.R. Mohammadi, and K. Takahata, "Non-Lithographically Microfabricated Capacitive Pressure Sensor for Biomedical Applications," *IET Electronics Letters*, 47(18), 2011, pp. 1015 - 1017.
2. K. Keikhosravy, D. Brox, P. Kamalinejad, S. Mirabbasi, and K. Takahata, "An Ultra-Low-Power 35nW Wireless Monitoring System for Biomedical Applications," under review, 2014.
   Contribution: IC testing, including PCB test board assembly, IC-sensor wire bonding, and verification of IC performance using electronic test equipment (oscilloscope, spectrum analyzer).
3. X. Chen, D. Brox, B. Assadsangabi, Y. Hsiang, and K. Takahata, "Intelligent Telemetric Stent for Wireless Monitoring of Intravascular Pressure and its In-Vivo Testing," *Biomedical Microdevices*, (2014), doi: 10.1007/s10544-014-9879-8.
   Contribution: Fabrication process development, sensor-stent integration, all aspects of *in vitro* testing.
4. D. Brox, X. Chen, S. Mirabbasi, and K. Takahata, "Ring-Down Wireless Reading of Resonant Smart Stents," under review, 2014.
5. B. Assadsangabi, X. Chen, D. Brox, and K. Takahata, "Ferrofluid Sacrificial Microfabrication of Capacitive Pressure Sensors," *IEEE Sensors*, accepted, 2014.
   Contribution: Design/fabrication of stainless steel sensor chips.

Conference papers:

1. D. Brox, A.R. Mohammadi, K. Takahata, "Non-Lithographically Micromachined Capacitive Pressure Sensor Based on Stainless Steel for Biomedical Applications," *IEEE Sensors, 2011,* pp. 312 - 315.
2. B. Assadsangabi, X. Chen, D. Brox, "Microfabrication of Capacitive Pressure

Sensors using Ferrofluid Sacrificial Layers*," IEEE Sensors, 2013*, pp. 703 - 706. Contribution: Design/fabrication of stainless steel sensor chips.

This thesis is submitted in partial fulfillment of the requirements for the degree of Doctor of Philosophy in Electrical and Computer Engineering and contains works done from January 2010 to January 2014. I have prepared this thesis in its entirety under the supervision of Dr. Kenichi Takahata. All work presented henceforth was conducted at the University of British Columbia (Vancouver campus), and represents work to which I directly contributed. Device fabrication and characterization (Chapters 2, 3, and 5) was performed in the laboratories of professors Kenichi Takahata, Mu Chiao, and at UBC's Advanced Materials Process and Engineering Laboratory. Range testing (Chapter 4) and integrated circuit design (Chapter 6) were performed in the laboratory of professor Shahriar Mirabbasi. Parts of text in Chapters 2 and 3 are based on previously published articles which I coauthored, and no other text is taken from previously published articles.

Table of Contents

List of Tables

List of Figures

List of Abbreviations

ALD atomic layer deposition

ASIC application specific integrated circuit

APS ammonium persulfate

AWG American wire gauge

CMOS complementary metal-oxide-semiconductor

FCC federal communications commission

FFR fractional flow reserve

HF hydrofluoric acid

IC integrated circuit

IF intermediate frequency

IPA isopropyl alcohol

LC inductor-capacitor

LCP liquid crystal polymer

LNA low noise amplifier

MEMS micro-electro-mechanical system

MOSFET metal-oxide-semiconductor field-effect transistor

µEDM micro-electro-discharge machining

PCB printed circuit board

PECVD plasma enhanced chemical vapor deposition

RBW resolution bandwidth

RF radio frequency

RMS root mean square

TGV through glass via

VFO variable frequency oscillator

Acknowledgements

I wish to take this opportunity to acknowledge a number of individuals who have been instrumental in my progression through my doctoral degree. Firstly, I would like to thank my supervisor, Dr. Kenichi Takahata, and the University of British Columbia for their financial support and the educational opportunity they provided me with. Because of this opportunity, I have had the privilege to publish original work, attend and present at conferences, and develop my own independence as a researcher through the challenge of solving a real world problem. I would also like to thank Dr. York Hsiang for his valuable assistance in my research, and generosity in answering any questions that I or other team members had. It was a great experience to work closely with a physician and learn how technologies in research labs can evolve towards clinical use. I'd also like to acknowledge the members of my proposal committee, Professors Edmond Cretu, Shahriar Mirabbasi, John Madden, and Lutz Lampe for their help in critiquing and directing my research, and the members of the AMPEL cleanroom staff, Mario Beaudoin, Alina Kulpa, and Jim McKenzie for their hard work and endless source of expertise. Finally, I'd like to express my gratitude to fellow members of the Takahata lab past and present, Babak Assadsangabi, Xing Chen, Kamyar Keikhosravy, Saquib Mirza, Yi Luo, Masoud Dahmardeh, Jeffrey Fong, Akio Taniguchi, Zhiming Xiao, Anas Bsoul, Mohamed Sultan, and Yan Wang. Thank you for sharing your ideas and offering moral support throughout the course of my studies.

To my parents...

Chapter 1: Introduction

This chapter introduces the objective of my doctoral research. It begins with a brief overview of coronary stenting and the problem of restenosis, and then explains why a wireless system for detecting restenosis would be useful. Previously developed systems are discussed, and motivation is given for different design approaches taken. The chapter ends by outlining the content of the rest of the thesis.

1.1 Coronary Stenting

Coronary artery disease is the progressive narrowing of coronary arteries due to the buildup of plaque on the arterial walls. If narrowing reaches a critical level, blood flow through the arteries is reduced, potentially causing a heart attack. For patients who suffer from this condition, doctors frequently suggest the implantation of a coronary stent to restore healthy blood flow. The medical term for this procedure is percutaneous coronary intervention (PCI). In 2004, the Canadian Institute for Health Information recorded 33,408 PCI procedures performed across Canada [1], and in each of the years 2002-2009, over 300,000 PCI procedures were billed to the Medicare population in the United States [2].

Fig. 1.1 [3] shows a drawing of a narrowed artery, and how a coronary stenting procedure is used to fix it. The material on the arterial walls causing the narrowing is a waxy substance called a plaque. Its primary constituents are macrophage cells, smooth muscle cells, and a complicated extracellular material that includes sulfated glycosaminoglycans, collagen, fibrin, and cholesterol [4]. The coronary stent is the metal scaffold expanded at the blockage site to force the artery open. When deployed, the stent is fixed on a balloon catheter and fed along a guide wire to the blockage site through an incision in one of the patient's femoral

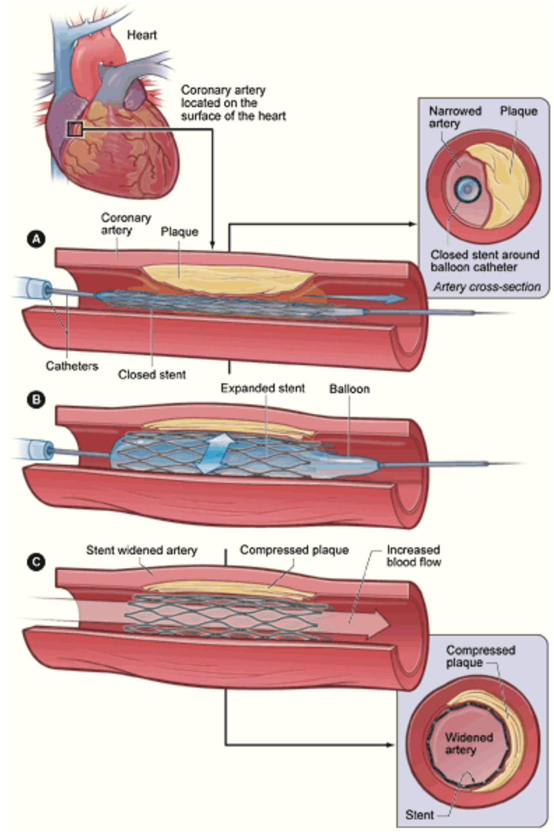

FIGURE 1.1: Coronary Stenting Procedure [3]

arteries (upper leg). The guide wire is pre-inserted using another catheter. Visualization and correct placement of the guide wire and stent catheters is achieved by repeatedly injecting x-ray absorbing dye into the blood stream through the catheter tips and x-ray imaging. Once the stent is correctly located, the balloon catheter is inflated to expand the stent to its full diameter, and then deflated so it can be removed. The remaining stent provides a permanent support against collapse of the vessel wall and removes any obstruction to blood flow caused by the plaque [5].

1.2 In-Stent Restenosis

The term ‘stenosis’ refers to narrowing of a blood vessel, and ‘in-stent restenosis’ refers to the re-narrowing of the interior of a stent that has been deployed to hold open a blood vessel.

This re-narrowing is caused by neointimal proliferation (growth of scar tissue) inside and around the stent which occurs as part of the body's immune response to implantation of a foreign object [6]. In a clinical context, in-stent restenosis refers to a $\geq 75\%$ reduction in stent cross sectional area since its insertion. With this level of occlusion, blood flow to the heart can be restricted, potentially causing a patient to experience chest pain or have a heart attack.

Numerous clinical trials have been conducted with different types of stents to determine which best prevent the onset of restenosis. The best results have been observed in studies with drug eluting stents [7-8], which are specially coated to release a drug that suppresses cell proliferation. In each of these studies, within 9 months of surgery, approximately 4% of patients had problems with their drug eluting stents that required revascularization procedures to fix. Both studies showed similar outcomes for the control populations, finding that about 15% of patients implanted with bare metal stents needed revascularization of the stented location within 9 months. Although these results suggest superiority of drug eluting stents, questions exist regarding the cost effectiveness of drug eluting versus bare metal stents [9], and whether or not drug eluting stents increase the likelihood of in-stent thrombosis (blood clotting within the stent) [10], so at present it is not clear what the full potential of drug eluting stents is for solving the problem of restenosis.

Given the number of patients receiving PCI procedures and the rates of in-stent restenosis, it is important to diagnose its onset before it causes deterioration in patient health. One method of diagnosing the state of a stented blood vessel is to take an x-ray of it and the surrounding area after x-ray absorptive dye is injected into the area (angiography). However, this procedure is invasive, requiring a similar catheter insertion to that used in stent placement, and can be dangerous to patients with kidney problems who have difficulty expelling the dye [11]. Also, it is quite expensive, costing 2200$ in British Columbia in 2007 [12], and thus is not ideal for routinely monitoring patients to determine their condition. The result is that most patients who are stented do not receive a test to determine the condition of the stent inside their body unless they experience chest pain or some other symptom indicative of advanced restenosis. In the case of diabetic patients who may not experience chest pain, this is particularly dangerous [13]. Therefore, a new method of accurately interrogating a stent's condition after implantation is required to reliably diagnose in-stent restenosis in order to tailor effective treatment.

To this end, work has been done adding pressure sensing capability to stents, to enable monitoring of their internal condition [14-16]. The reason for this is that when the heart is in a particular physiological state (maximum vasodilation) induced by heavy exercise or administration of a drug, knowledge of the blood pressure up and downstream of the stent is adequate assess the severity of an in-stent blockage [17].

To see this, a simple circuit model of the coronary blood flow is helpful (Fig. 1.2 [17]). In a state of maximum vasodilation, the coronary resistances R_s (occlusion resistance), R_c (collateral resistance), and R (vascular bed resistance), are constant, and R is minimal. In fact, R may be a factor of 4 or 5 lower than its average resting value in this state. With no stenosis present, the total vascular resistance is dominated by R, since large arteries make up only ~1%

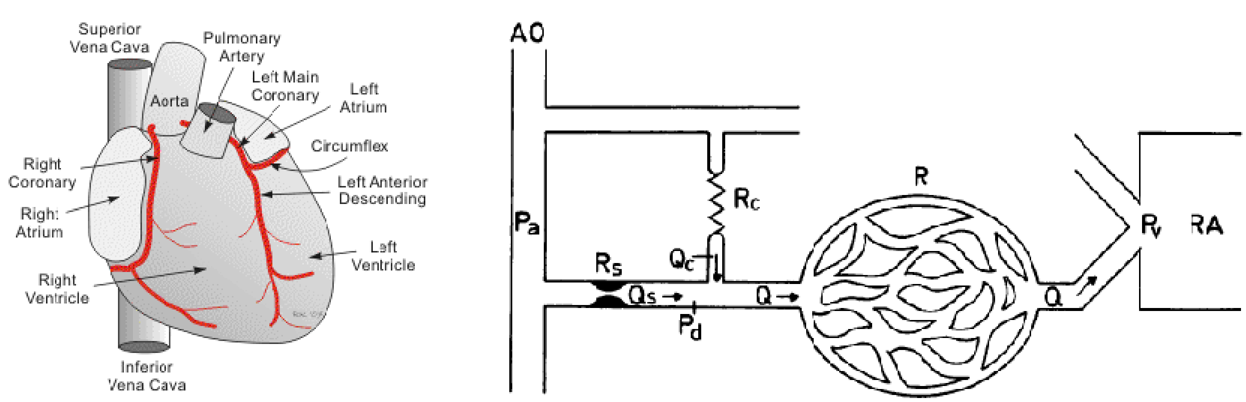

FIGURE 1.2: Coronary Blood Flow Schematic [17]

of the total resistance. In this case, $P_a = P_d$. However, when stenosis occurs, R_s may increase orders of magnitude, causing a pressure drop across the stenosis.

The fractional flow reserve, defined as:

$$FFR = \frac{Q_{stenosis}}{Q_{without}} = \frac{P_d - P_v}{P_a - P_v} \quad (1)$$

is the ratio of maximal blood flow with stenosis to maximal blood flow without stenosis, and is a common figure of merit for characterizing the biological relevance of an occlusion. One study of 60 patients correlated FFR and trans-stenotic pressure gradients with the onset of chest pain during heavy exercise [18]. This study asserted a strong correlation between chest pain and the conditions:

$$FFR < 0.66, \qquad \Delta P_{vasodilation} > 30\ mmHg, \qquad \Delta P_{resting} > 12\ mmHg \quad (2)$$

although the correlation between $\Delta P_{resting}$ and chest pain was asserted to be weaker than the correlation between FFR and chest pain, because of variations in vascular bed resistance.
A second study of 101 patients [19] suggested a correlation between $\Delta P_{vasodilation} > 30\ mmHg$ and a significant change in blood flow velocity between proximal and distal ends of a stenosis, suggesting re-routing of blood flow due to the blockage. Therefore, taking $\Delta P_{vasodilation} > 30\ mmHg$ and $\Delta P_{resting} > 12\ mmHg$ as diagnostics for the presence of restenosis, it is reasonable to require a restenosis monitoring sensing system measure translesional blood pressure with $\sim 1\ mmHg$ resolution to detect restenosis. This resolution must be achieved at smart stent-reader distances of at least 3.5cm to successfully monitor coronary arteries [16]. A 'smart stent' capable of reading and transmitting blood pressure information wirelessly outside the body at this distance might provide a means of detecting in-stent restenosis early on, at lower

cost and risk than angiography [20]. The development of such a smart stent and associated wireless reader is the subject of this thesis.

1.3 Implantable Pressure Monitoring Systems

To date, no system for wireless in-stent pressure monitoring has performed successfully *in vivo*, although several research papers on the subject have been published, and pressure monitoring implants for other medical applications have been commercialized. A common feature of all these systems is a miniature pressure sensing element that leaves a small footprint inside the human body; this requirement is typically met using micro-electro-mechanical systems (MEMS) pressure sensing technology [21]. All systems also have an antenna for wireless transmission of pressure information outside the body, and for wireless powering in the event that the implant does not use batteries.

1.3.1 LC Tank Systems

One of the simplest such pressure monitoring systems uses an implant consisting of a MEMS capacitive pressure sensor and inductor in an inductor-capacitor (LC) tank configuration [22]. The resonant frequency of the LC tank then depends on the pressure, and can be determined wirelessly from measurements of the electrical impedance of a loop antenna placed in proximity (magnetically coupled) to the tank [23]. A wide variety of devices for pressure sensing in aneurysms [24], the eye [25], and cerebrospinal fluid [26] have taken this sensing approach, utilizing a small spiral inductor with lateral dimensions on the order of millimeters to obtain a very small footprint. These devices work well when implanted close to the surface of the body, but have a read range of only a few centimeters due to limitations in magnetically coupling to small inductors. A photo of such a device is shown in Fig. 1.3 [23]. This device uses a gold electroplated spiral inductor and anodically bonded capacitive pressure sensor.

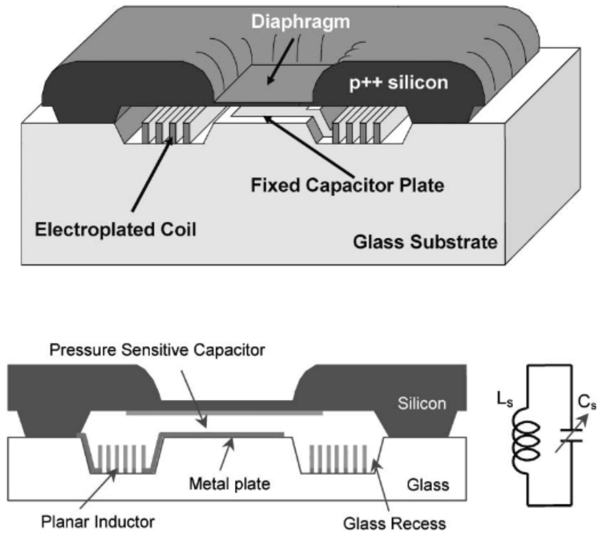

FIGURE 1.3: MEMS LC Tank Device [23]

Similar devices vary considerably in their fabrication and material composition.

Commercial products have also been designed based on this approach. An LC MEMs resonator for intraocular pressure sensing is produced by LaunchPoint Technologies [27]. It can be attached to the intraocular lens or injected into the vitreous humour at the back of the eye. Another commercial device for monitoring blood pressure in the pulmonary or aortic arteries is offered by CardioMEMs [28]. Its inductor has dimensions on the order of centimeters rather than millimeters to enable powering by magnetic coupling from several centimeters away (Fig.

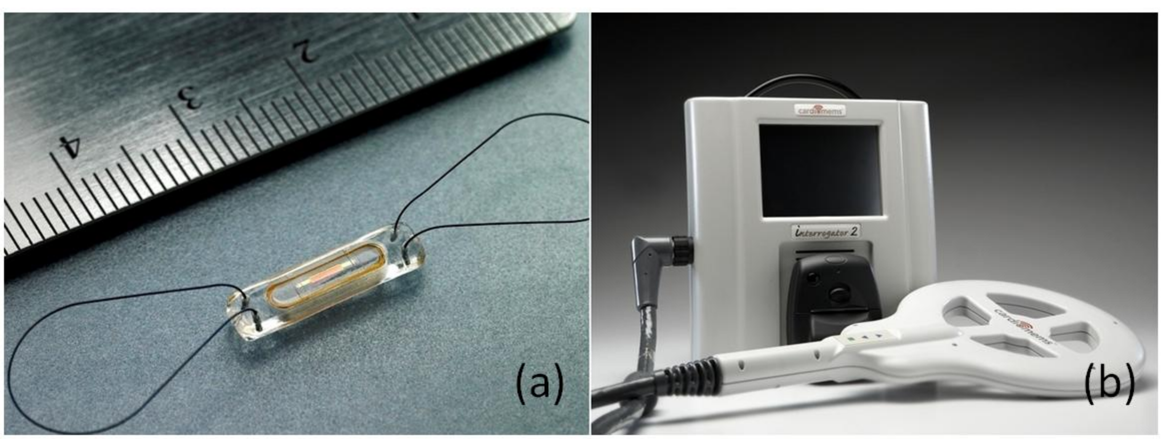

FIGURE 1.4: CardioMEMs Aortic Aneurysm Monitor [29]
CardioMEMs (a) pressure sensing device and (b) wireless reader.

1.4 [29]). However, neither of these commercialized monitors has both the required size and read range to monitor blood pressure inside the coronary artery, which is a relatively narrow vessel (~5 mm in diameter) residing several centimeters within the body.

To circumvent this problem, an interesting alternative is to try using the stent itself as an inductor. This has the apparent advantages of not requiring any separate inductor fabrication, and potential for better magnetic coupling with a reader because of the relatively large dimensions of the stent (1 - 3 cm length, 3 - 5 mm diameter). An illustration of such a system is shown in Fig. 1.5. Optimization of this design approach and addressing the challenges associated with its practical application are central topics of this thesis.

1.3.2 CMOS Systems

Because of the way in which they operate, LC tank pressure sensing devices do not require any complementary metal-oxide-semiconductor (CMOS) integrated circuits (ICs) to

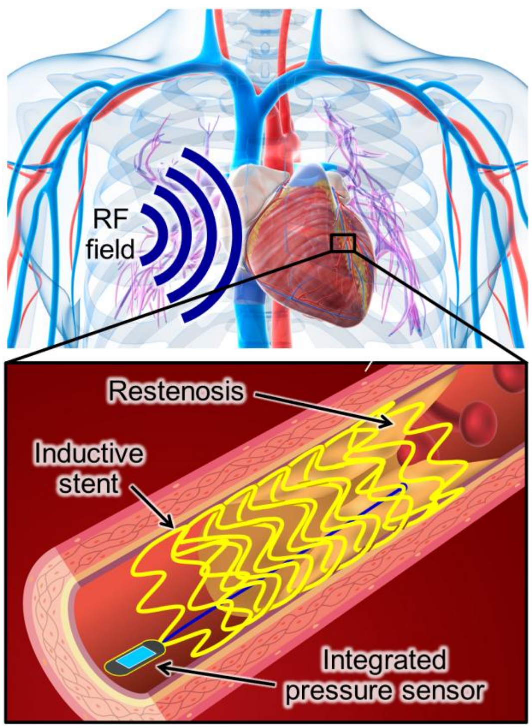

FIGURE 1.5: Smart Stent Sensing System (LC Tank)
Conceptual diagram of a stent/sensor (LC tank) smart sensing system.

function.   This has the benefit of simplifying device design, but is restrictive to the choice of wireless protocol, bandwidth, and communication range. Therefore, many pressure sensing systems have been developed using application specific integrated circuits (ASICs) for reading and transmitting data from pressure sensor(s). Applications include monitoring restenosis [15, 30], congestive heart failure [31], glaucoma [32], abdominal aortic aneurysms [33-34], the bladder [35], the carotid artery [36], and hydrocephalus [37]. The architecture of these systems varies considerably, but all of them rectify an external RF signal to power their ASIC. This RF signal is received by the implant using a built-in antenna, which is typically a loop antenna, but in the case of in-stent restenosis monitors is the stent itself. The same antenna is used for receiving power and transmitting pressure data out of the implant in all cases except [31], in which a second loop antenna is used.

Most of the aforementioned CMOS based systems use capacitive pressure sensors, although the bladder monitor uses an off the shelf piezoresistive pressure sensor. There are a couple of advantages to using capacitive pressure sensors in these monitoring applications: (1) they show less temperature dependence than piezoresistive sensors at human body temperatures [38] (35 - 42 ºC) and (2) it is possible to integrate their fabrication with a CMOS IC fabrication process to produce compact CMOS-MEMS hybrid chips [32, 33, 36]. This second possibility removes the necessity of bonding the ASIC and MEMS sensor together, which is important for size-critical applications.

For wireless transmission of pressure information, backscatter modulation is the most common technique used by ASIC based systems. This is the technique widely employed in radio frequency identification (RFID) [39], and works by using the CMOS IC to switch the impedance of the implant antenna between two states as it receives the RF signal powering the chip. These two states are identified by an external reader as differences in reflected signal amplitude, so that an amplitude-shift keying (ASK) data link is established between reader and implant. The glaucoma and abdominal aortic aneurysm monitors operate in this manner at standard industrial, scientific, and medical (ISM) carrier frequencies (13.56 MHz and 133 kHz respectively), while the bladder, carotid, and hydrocephalus monitors operate similarly at other carrier frequencies. Notably, the two restenosis monitor ASICs are designed to be powered by much higher frequency signals in the GHz range, and do not use backscatter modulation to transmit information. Instead, each monitor has its own integrated oscillator, and uses frequency modulation (binary frequency-shift keying (BFSK) [16] or capacitance to frequency conversion [30]) to communicate. These GHz operating frequencies are also much higher than the operating frequencies employed by inductive stent (LC tank) restenosis monitors to date (< 300 MHz), and further research into tradeoffs between tissue penetration depth and power transfer efficiency is needed to identify which range is optimal for this application. To help investigate this issue, the design of a capacitance to frequency converting ASIC based system will be discussed later in detail. Fig. 1.6 shows a previously developed ASIC based smart stent [16], where the CMOS IC and capacitive pressure sensor are contained in a liquid crystal polymer package bonded to a stent.

1.4 Thesis Outline

- **Chapter 2** discusses the fabrication and characterization of a capacitive pressure sensor. One novel characteristic of this sensor is that it is fabricated on a stainless steel substrate, as opposed to silicon. The advantages and drawbacks of this approach are explained.
- **Chapter 3** discusses the process of integrating stainless steel based capacitive sensors with coronary stents to form LC tank devices with wireless in-stent pressure monitoring

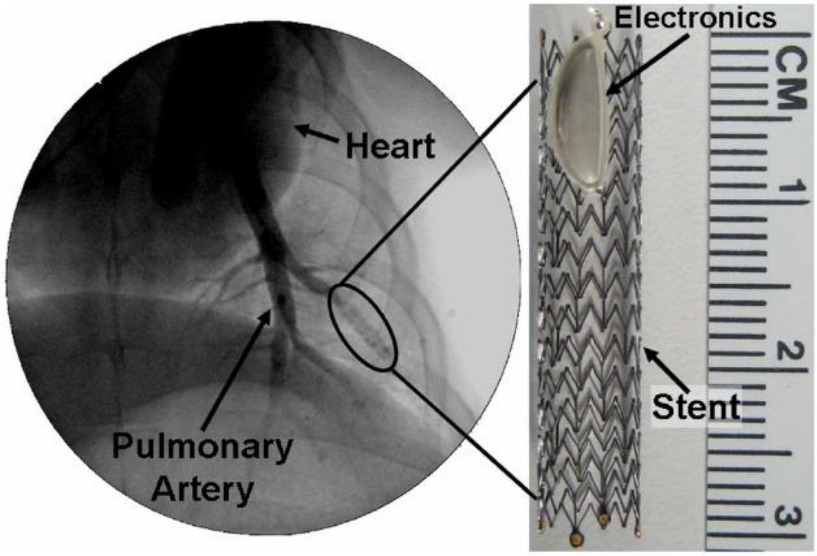

FIGURE 1.6: Smart Stent Sensing System (CMOS) [16] - © 2010 IEEE
A CMOS integrated circuit and capacitive pressure sensor packaged in liquid crystal polymer and integrated with a stent. An X-ray of the stent after deployment is shown on the left.

and move towards clinical relevance are described in detail. The *in vitro* experiments performed with these devices are explained, and the results are discussed. Problems preventing practical monitoring are clearly identified, pointing out limitations of the inductive stent based design approach.

- **Chapter 4** examines the sensing range and resolution of inductive stent based LC tanks, and miniaturized planar LC tanks. A different, ‘ring-down’, reader methodology is explored as a means of extending sensing range.
- **Chapter 5** describes the fabrication and characterization of a surface micromachined capacitive pressure sensor, designed for incorporation in an LC tank based in-stent pressure monitoring system with improved range and mechanical robustness. A miniaturized MEMS LC tank pressure sensor consisting of a surface micromachined capacitive pressure sensor integrated with an electroplated micro-inductor is proposed. The motivation for using these tanks for in-stent restenosis monitoring is explained.

- **Chapter 6** describes the design of a CMOS integrated circuit for use in an in-stent restenosis monitoring system. The design uses a standard commercial stent as a source of power and communication, without any additional features such as an external wire that could complicate deployment. Special attention is paid to electromagnetic modeling of the stent antenna and chip interface to maximize wireless power supply and communication range. Lessons learned from the design process are used to suggest desirable features of a CMOS based in-stent restenosis monitoring system.
- **Chapter 7** lists the original contributions to research contained in this thesis, and discusses the extent to which original project objectives have been met. Future directions of research are suggested.

Chapter 2: A Stainless Steel Based Capacitive Pressure Sensor

2.1 Background and Motivation

An LC tank monitoring system requires a capacitive pressure sensor for its operation. In most instances [22-23], the sensor used is a conventional silicon based MEMs capacitive pressure sensor. This is because well-established techniques for fabricating silicon based sensors already exist. However, there are several drawbacks to using these sensors in LC tank implants. Firstly, to maximize sensing distance, the quality factor Q of the resonator should be as large as possible [40], which suggests the series resistance of the LC tank should be minimized. This is not the case in a conventional silicon based capacitive pressure sensor, where the flexible membrane consists of doped silicon with a much higher series resistance than a metal. For instance, the series resistance of the commercially available E1.3N capacitive pressure sensor [41] offered by MicroFAB Bremen GmbH is measured to be 700 Ω at 10 MHz, and is the dominant resistive contribution to any inductive stent LC tank circuit in which it is used. Secondly, in the case of an inductive stent based tank, the bond between the stent and silicon sensor has relatively high contact resistance and unknown long-term mechanical performance inside the body. Lastly, silicon poses a greater bio-fouling risk as compared with stainless steel [42], and thus is not preferable for use in implants.

Because of these issues, a new capacitive sensor, based on stainless steel, has been developed for use in an inductive stent LC tank system [43-44]. The original intention in using stainless steel was to fabricate sensors directly on inductive stents for seamless integration. However, this approach presented the challenge of applying micro-fabrication techniques to stent substrates with awkward/curved geometries, so attention was shifted to fabricating a sensor on a separate flat stainless steel substrate for stent integration later.

2.2 Fabrication

Two similar methods of fabricating stainless steel based capacitive pressure sensors have been developed. The first method uses Parylene as a membrane-substrate bonding material. This process produces working sensors, but has low yield. Therefore, a second process using polyimide as a membrane-substrate bonding material has been developed and shows improved results.

2.2.1 Fabrication 1 – Parylene Bonding

Parylene bonded sensors are formed by bonding a Parylene-C / metal composite membrane to micromachined stainless steel chips with cavities in their center. After bonding, the metal membrane and steel substrate of each sensor act as plates of a capacitor with a Parylene-C dielectric layer. When pressure is applied to the sensor, the membrane deflects down into the cavity, increasing the capacitance between it and the stainless steel substrate. A schematic diagram of the bonding process and final sensor is shown in Fig. 2.1.

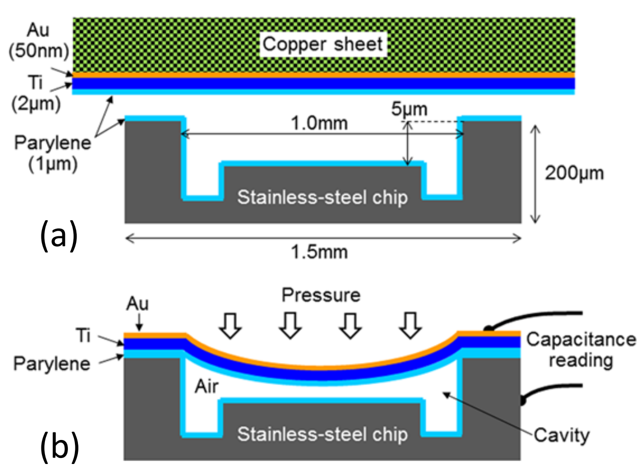

FIGURE 2.1: Stainless Steel Based Capacitive Pressure Sensor
Schematic diagrams of the (a) membrane-substrate bonding process and (b) final capacitive pressure sensor.

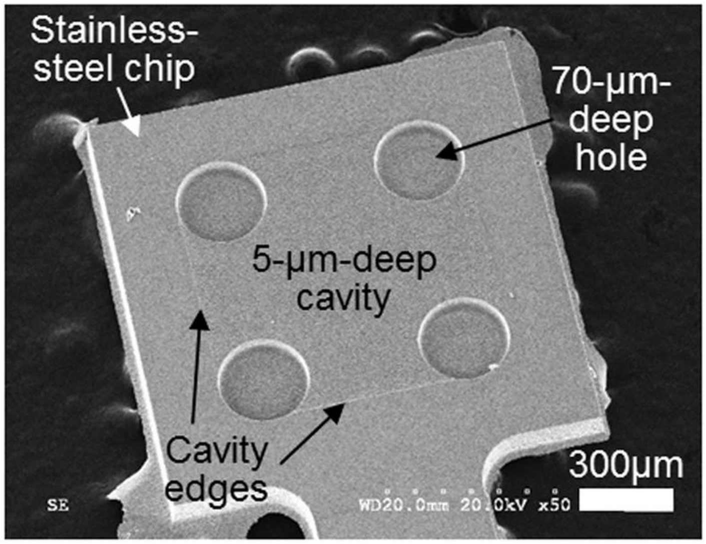

FIGURE 2.2: Stainless Steel Sensor Substrate
Electron microscope image of a µEDMed 316L stainless steel sensor substrate.

200 µm thick 316L stainless steel sheet by micro-electro-discharge machining (µEDM), and polished afterwards with a diamond lapping sheet (LFG1D, ThorLabs, USA) to remove any protruding edges and reduce surface roughness. Inside the cavity, four 300 µm diameter holes with 70 µm depth are µEDMed to increase the volume of the cavity space. This increase in volume enables larger deflections of the membrane with applied pressure, for increased sensor sensitivity. An image of a sensor substrate is shown in Fig. 2.2.

On a separate 100 µm thick Cu sheet (50nm surface roughness), a 5 nm Ti / 50 nm Au / 2 µm Ti multilayer metal film is e-beam deposited to form the sensor membrane, and coated with 1 µm of Parylene-C in preparation for bonding. The stainless steel substrate is also coated with 1 µm of Parylene-C during the same deposition process. Next, the Parylene-C coated surfaces of the membrane and substrate are thermally bonded together in air at 175 ºC for 35 minutes under ~50 MPa of applied pressure using a custom mechanical fixture [45]. After bonding, oxygen plasma and wet etching processes are used to remove the excess Parylene-C and metal multilayer film surrounding the bonded substrate. The sensor is then released by wet

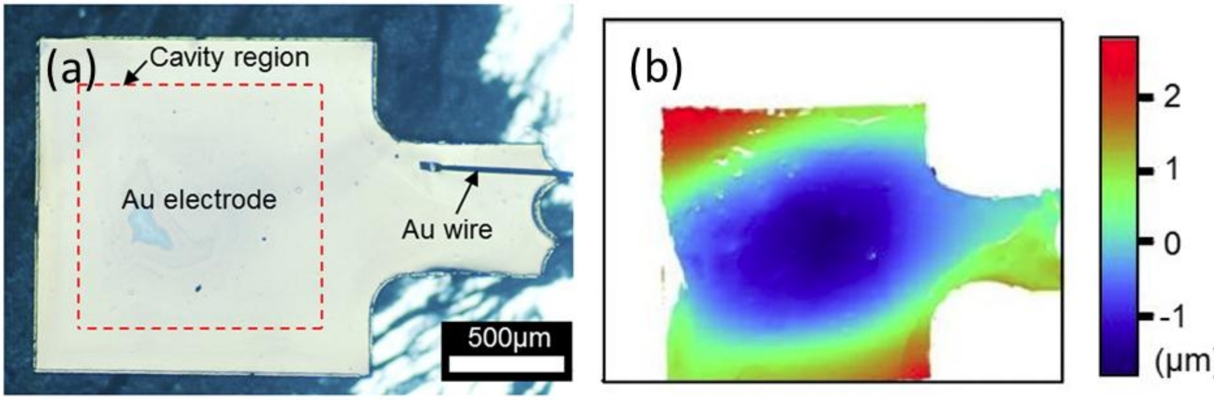

FIGURE 2.3: Parylene Bonded Sensor

(a) Fabricated sensor with wire bond for electrical characterization. The dashed red square indicates the position of the 5μm deep cavity. (b) Optical profile of the same sensor.

etching the entire Cu sheet, and the 5 nm Ti adhesion layer remaining on its surface is removed by a brief dip in dilute HF. An optical micrograph of a finished sensor that has been wire bonded for testing is shown in Fig. 2.3(a), and an optical profile of the same sensor is shown in Fig. 2.3(b). The dark blue region in the center of the optical profile indicates that it is depressed ~5 μm relative to the edges of the cavity. The measurement suggests that the membrane is not perfectly suspended, but contacting the bottom of the cavity.

2.2.2 Fabrication 2 – Polyimide Bonding

Fabrication using Parylene bonding produced working sensors, but had low yield (<5%) due to inconsistencies in bond quality. Many sensors would not show any change in capacitance with applied pressure due to incomplete bonding, and some sensor membranes and substrates would fail to bond at all if they were not well aligned during thermal bonding. To combat this issue, Parylene-C was replaced with HD-3007 adhesive polyimide as a bonding agent. This polyimide was designed as an adhesive for temporary or permanent packaging applications, and is similar to other polyimides that have been used for wafer bonding [46]. Yield using the polyimide based fabrication process is improved to approximately 50%.

The polyimide bonding process begins with micromachining a stainless steel substrate with the same lateral dimensions as before, but a slightly deeper cavity (10 - 20 µm) to help keep the sensor membrane suspended. Also, to ensure no electrical shorting between the membrane and substrate occurs during bonding due to surface irregularities, the substrate is coated with 1µm of electrically insulating silicon dioxide by plasma enhanced chemical vapour deposition. Next, the membrane is formed by e-beam depositing a 50 nm Cr / 150 nm Au / 50 nm Ti multilayer metal film on Cu foil. To bond, a single 2 µm thick polyimide layer is spin coated on the membrane and prebaked for 3 minutes on a hotplate as the temperature is ramped from 90 to 150 ºC. This prebake is used to evaporate most of the solvent out of the spin coated polyimide before bonding the membrane to the insulated steel substrate at 260 ºC for 35 minutes under 50 MPa of pressure. After thermal bonding, the excess polymer/metal membrane is etched away, and the final sensor is released by etching away the Cu foil as before. Finished pressure sensors are shown in Fig. 2.4.

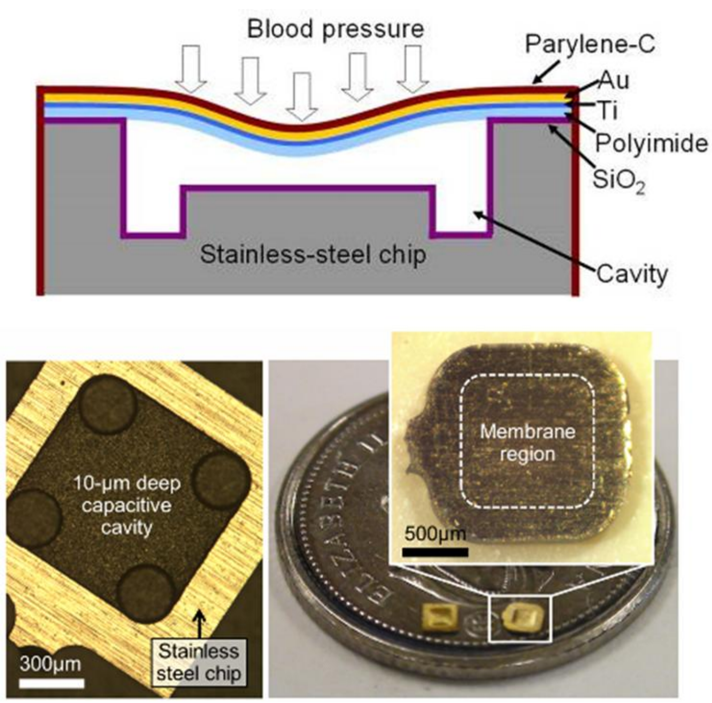

FIGURE 2.4: Polyimide Bonded Sensor
This figure shows a polyimide bonded sensor schematic diagram, steel substrate, and close-up image.

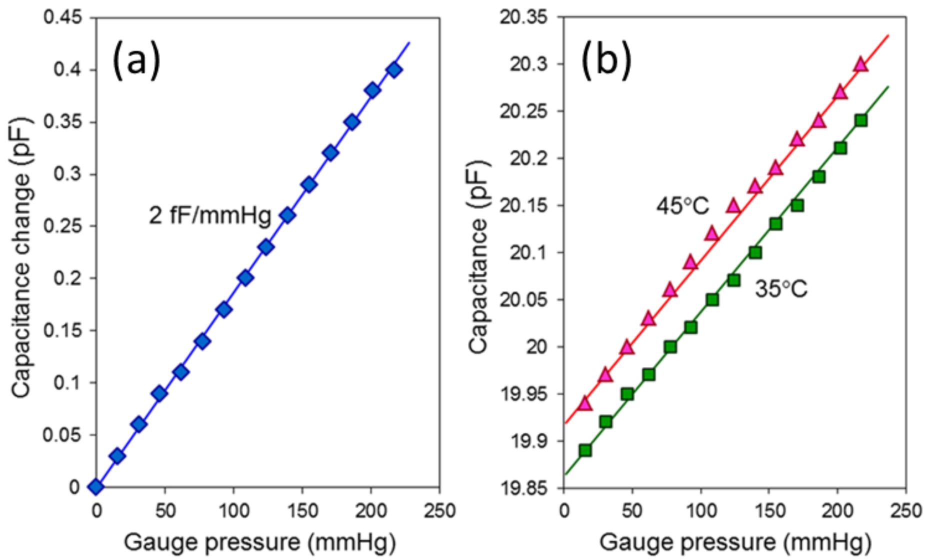

FIGURE 2.5: Parylene Bonded Sensor Pressure and Temperature Response
(a) Pressure and (b) temperature response of a Parylene bonded sensor.

2.3 Characterization

To test the sensors, electrical connections were made to their membranes and substrates by wire bonding and silver pasting leads. Each sensor was tested inside a custom chamber whose internal pressure could be adjusted using a syringe pump, and read from a reference pressure sensor (PX-26, Omega Engineering Inc., QC, Canada) coupled to the chamber. The sensor leads were fed into an LCR meter (HP 4275A) to measure the sensor capacitance as a function of pressure. Fig. 2.5(a) shows a plot of capacitance vs pressure recorded from a typical Parylene bonded sensor. The base capacitance of the sensor (19.75 pF) increased by 0.4 pF for a 200 mmHg increase in ambient pressure. The pressure response is highly linear and corresponds to a constant sensitivity of 2 fF / mmHg over a gauge pressure range of 0 - 250 mmHg. The linear response is attributed to the touching of the membrane to the cavity bottom (evident from optical profiling), since membrane-substrate contact is known to result in response linearity of capacitive pressure sensors [47].

Further tests were performed to determine the temperature sensitivity of a Parylene bonded sensor (Fig. 2.5(b)). Sensor capacitance was found to vary linearly with temperature over a biologically relevant range (35 - 45 ºC), with an average sensitivity of 250 ppm/ ºC. An important factor contributing to this sensitivity is the significant rise in the permittivity of Parylene-C with temperature (4400 ppm/ ºC [48]). Although a rise in temperature may pressurize the air inside the cavity and push the membrane away from the sensor substrate, reducing capacitance, the rise in dielectric constant could have counteracted this effect to create an overall increase in capacitance. This may explain why the sensor's temperature sensitivity is slightly higher than that of a commercial capacitive pressure sensor (139 ppm/º C [41]) with a vacuum sealed cavity and silicon nitride dielectric.

The capacitance versus pressure plots for three different polyimide bonded sensors are shown in Fig. 2.6. The varying results show how different cavity depths and bonding parameters lead to different base capacitances and pressure sensitivities. All sensors exhibit highly linear responses, of 2 - 3.1 fF/mmHg, and up to 7.85% change in total capacitance under 250 mmHg of

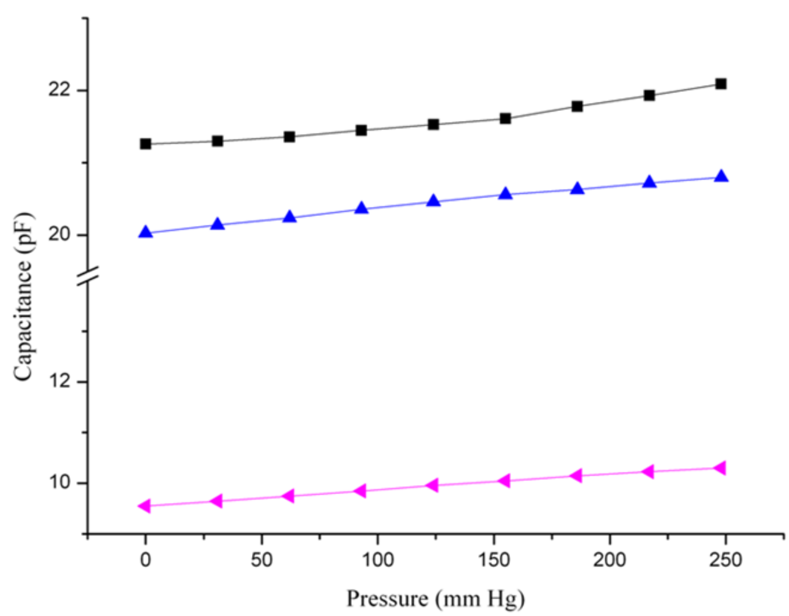

FIGURE 2.6: Polyimide Bonded Sensor Pressure Response

applied pressure. This range of sensitivity is similar to that obtained for Parylene bonded sensors, and response linearity is again attributed to membrane-substrate contact observed in optical profiles of the sensors.

2.4 Discussion

The stainless steel based capacitive pressure sensors described in this chapter offer several advantages over standard silicon based pressure sensors when applied in LC tank wireless pressure monitors. Principally, they reduce tank series resistance, thereby increasing sensing range, and potentially avoiding any bio-fouling hazard present from using silicon. Furthermore, for designs where stents are used as tank inductors, techniques such as laser welding exist for forming reliable long-term bonds between sensors and stents.

However, there are also drawbacks to using the stainless steel sensors in their current state of development. One issue is the variation in sensor performance evident in Fig. 2.6. This variability makes it more difficult to wirelessly determine the sensor pressure reading when it is integrated in an LC tank, and can only be improved by further refinement of the μEDM machining and thermal bonding processes employed during fabrication. The extent to which such refinements can be made and device tolerances lowered is not clear without further research, since these processes are not standard MEMS fabrication techniques and there is little pre-existing research in this area. This problem can be circumvented by individually calibrating stent-sensor integrated devices to account for sensor performance variations. Novel methods of fabricating sensors using ferrofluid sacrificial layers that avoid thermal bonding are also currently being explored [49-50].

In addition, the issue of how to scale up the μEDM and bonding processes for increased throughput rivaling that of a conventional MEMs fabrication process is not resolved, and could present a drawback to practical implementation of the technology. Currently, it takes about 4 hours to µEDM a single steel substrate, and only a few sensors are thermally bonded at a time. Although parallelization of µEDM processes has been reported [51], throughput is not comparable to the state of the art in MEMs sensors, where established fabrication techniques for processing thousands of devices in parallel exist. Therefore, if a process using standard micro-fabrication techniques could be developed to produce all-metal capacitive pressure sensors, it would have clear economic advantages in production speed over a µEDM-based process (as described in this chapter) at present.

Finally, the sensors in their current state of development are not particularly sensitive when compared with other capacitive pressure sensors in the literature. This reduces the wireless read range and resolution of systems in which they are used. To increase their sensitivity, further research and development is necessary.

In Chapter 5, an alternative surface micromachining fabrication process for making capacitive pressure sensors is presented. This approach uses standard micro-fabrication techniques, and is intended to address outstanding issues related to process variation, throughput, and sensor sensitivity.

Chapter 3: Integrated Sensor/Stent System for Blood Pressure Monitoring

This chapter describes the synthesis of a stent with wireless pressure monitoring capability. The design integrates an inductive stent and capacitive pressure sensor to form a pressure sensitive LC tank, following the same basic approach of previous work, but making several improvements [52]. *In vitro* tests of integrated devices are described, and the results are discussed at length.

3.1 Stent Design

For the targeted in-stent restenosis monitoring application, the stent works as a mechanical scaffold and electrical inductor/antenna, and must be designed to meet both these requirements with high performance. Commercially available stents have struts (bridges) that connect loops created in a cylindrical structure along the axial direction, forming electrical pathways that allow current passing through the stent to run in a straight line rather than a helix. This diminishes the mutual inductance achievable between the stent and an external antenna, and therefore decreases the wireless sensing range of the overall system. Since achieving maximum sensing distance is a critical concern for wireless monitoring of the coronary arteries (at least 3.5 cm required [16]), a helical stent structure with the struts between loops removed is utilized in this research [53].

The helical stents are laser micromachined out of 316L stainless steel tubing (EVASC Medical Systems) with an outer diameter of 2 mm and a wall thickness of 100 μm (Fig. 3.1). They are cut to a length of 20 mm, with 17 turns and zigzag patterns to relieve bending stress during expansion. Each end of the stent is created with a 0.5×1.75 mm^2 extension that can be

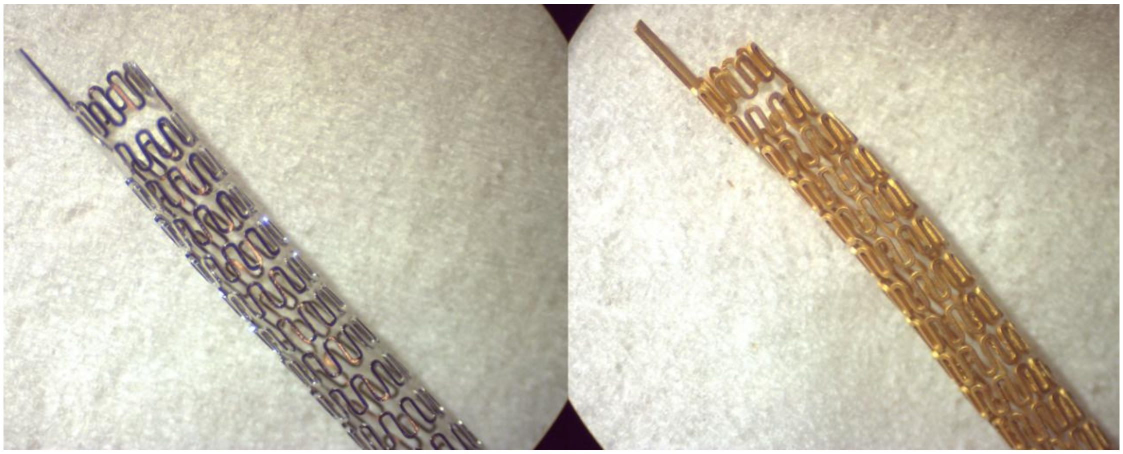

FIGURE 3.1: Helical Stent Before and After Gold Electroplating

used as a platform for sensor-stent integration. Unlike the planar approach to inductive stent formation used in previous research [20], this more standard laser machining approach facilitates compatibility with standard stenting tools.

After machining, the stents are surface finished by electro-polishing [54] as is common practice in industry. Then, to increase the quality factor of the LC tanks in which the stents are incorporated, gold is electroplated on the stents to reduce their electrical resistance. Gold is selected as the coating material for this purpose because it provides good biocompatibility, much higher conductivity than 316L stainless steel (4.1×10^7 S/m versus 1.3×10^6 S/m), and is easily electroplated. The electroplating process is performed in a cyanide-based solution (TriVal-24K Acid Gold Strike + 24K Bright Gold Solution, Gold Plating Services) with a custom rotational set-up that enables uniform deposition of the material over the entire surface of the stents. A plating thickness of 15 μm is used to avoid considerably changing the stent mechanical properties, while efficiently increasing conductivity in the relevant frequency range because of the small skin depth of gold (~10 μm at 50 MHz). After electroplating, stent series resistance is measured to be 1.5 Ω (DC), down from 30 Ω before plating.

3.2 Sensor/Stent Integration and Packaging

The helical stent is designed with two 0.5 mm x 1.75 mm extensions at each end for sensor and wire attachment, although only single sensor integrations have been attempted thus far to avoid the additional complexity of integrating two sensors. Both conventional adhesive bonding (Fig. 3.1(a)) and laser welding (Fig. 3.1(b)) have been experimented with as a means of integrating sensors and stents. Silver based Chemtronics conductive epoxy was used for adhesive bonding, and a FiberStar laser welding system from LaserStar Technologies was used for welding. For simplicity, μEDM'd steel substrates were bonded to the stent extensions for electrical characterization, and the electrical resistance (at 10 MHz) of bonds was tested. As shown in Table 3.1, laser welded bonds had lower resistance than conductive epoxy bonds. This is not surprising, since molten bonds remove contact resistance and form nearly non-destructive joints. Laser welds also only took a fraction of a second to form, while epoxy bonds had to set for tens of minutes. Thus, laser welding is more amenable to automation for scaling up throughput. Despite these advantages, epoxy bonding was used to integrate the devices tested in this work because of its relative simplicity and the small number of samples being processed.

Prior to sensor-stent bonding, 20 - 30 μm of Parylene-C is conformally coated on stents

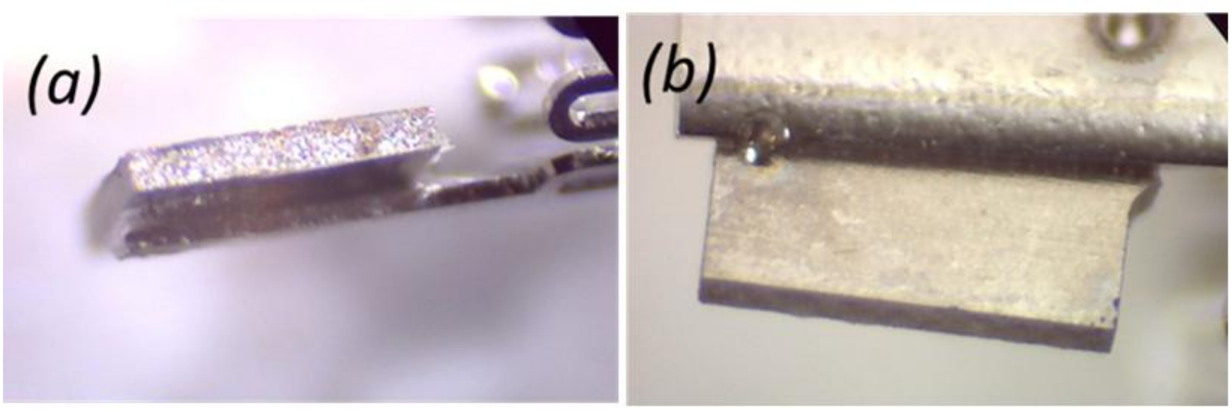

FIGURE 3.2: Sensor/Stent Bonding
Stainless steel substrate attached to a stent extension using (a) conductive epoxy and (b) laser welding.

TABLE 3.1: Electrical Resistance of Different Bonds

Bonding Method	Bond Electrical resistance (Ω)
Conductive Expoxy	5.3
Laser Welding	0.83

using a commercial coater (Labcoter 2, Specialty Coating Systems Inc., IN, USA). This electrical insulation prevents capacitive shorting between the stent's loops during operation in a conductive medium such as blood.

After sensor-stent bonding, LC circuits are established by electrically connecting sensor membranes and metal extensions on opposing ends of stents by adhesive bonding copper wire (enamel insulated, 80 μm in diameter). Then, another 2 - 3 μm thick layer Parylene-C is conformally coated over device surfaces to electrically insulate the sensors, wires, and joints, and ensure device biocompatibility [55]. Images of integrated devices prior to expansion are shown in Fig. 3.3(a). The Parylene-C coatings used were observed to exhibit high chemical and

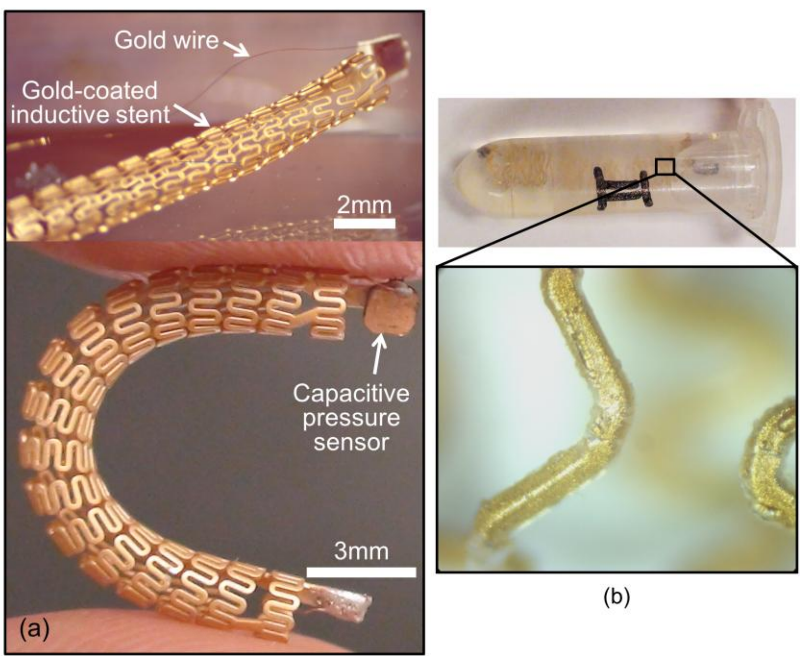

FIGURE 3.3: Integrated Device
(a) Fabricated LC-tank devices integrated with capacitive pressure sensors and (b) the coating quality of Parylene-C after device immersion in saline for approximately one year.

adhesion stability; a sample device passivated with 25 μm of Parylene-C was left in saline solution at room temperature for nearly one year and showed no signs of Parylene peeling or degradation (Fig. 3.3(b)).

3.3 Integrated Device Expansion

Deployment of integrated devices was performed in the same way as commercial stent deployment. Each device was crimped on a 4 cm long balloon catheter (e.g., Advance® 18LP Low Profile PTA Balloon Dilatation Catheter, Cook Medical Inc., IN, USA) in a contracted state. Once positioned for expansion, deionized water was injected into the balloon using an inflation device (Cook® Sphere, Cook Medical Inc., IN, USA) to expand the balloon and stent.

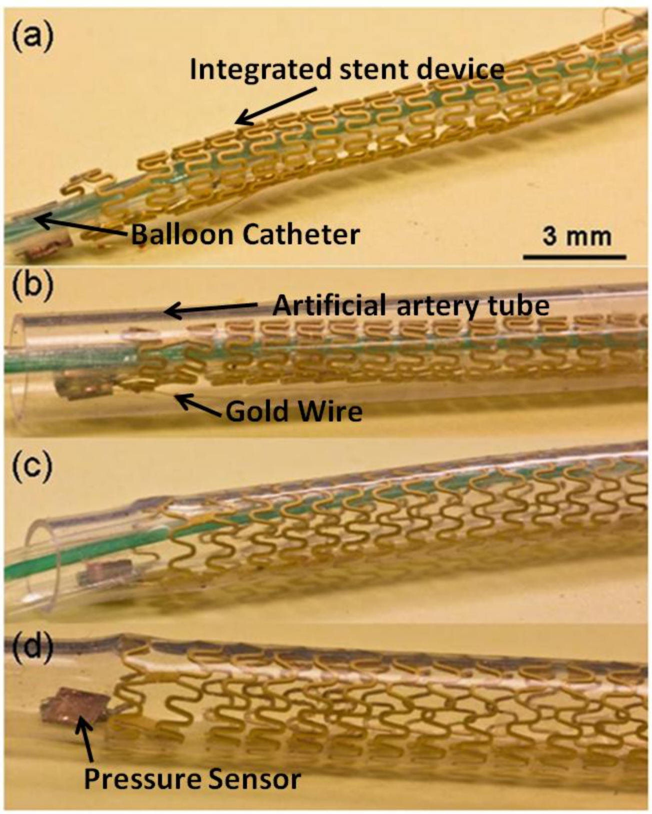

FIGURE 3.4: Integrated Device Deployment
Integrated device expansion sequence: (a) balloon catheter insertion into stent/sensor device and crimping; (b) stent/sensor device guided insertion into a mock vessel; (c) inflation of catheter balloon to permanently expand the stent inside the mock vessel; (d) deflation and removal of the balloon catheter, leaving stent in place.

Balloon catheters with different inflation diameters (3-6 mm) were selectively used for the expansion tests. Figs. 3.4(a) - (d) display the deployment of one integrated device performed inside a silicone mock artery tube with a 3 mm diameter (Dynatek Labs, MO, USA). As evident from the images, uniform expansion and deployment of the device was achieved, and it formed a scaffold for the tube walls. The stent in its unexpanded state was measured to have an inductance of 260 nH (at 50 MHz), and an inductance of 530 nH after expansion.

Similar expansion tests were performed with more than 15 samples. Typically, devices expanded to small (3 - 4 mm) diameters showed little or no visible non-uniformity after expansion. However, without struts to prevent irregular stretching and compression, all stents expanded to 5 mm or more in diameter showed clear non-uniformities in their expanded state (Fig. 3.5), and in the worst cases, buckling. Also, although nearly all devices expanded outside tubing showed no functional failure and preserved their wireless sensing ability, failures were observed for expansions inside mock arteries about 20% of the time. These failures were mostly

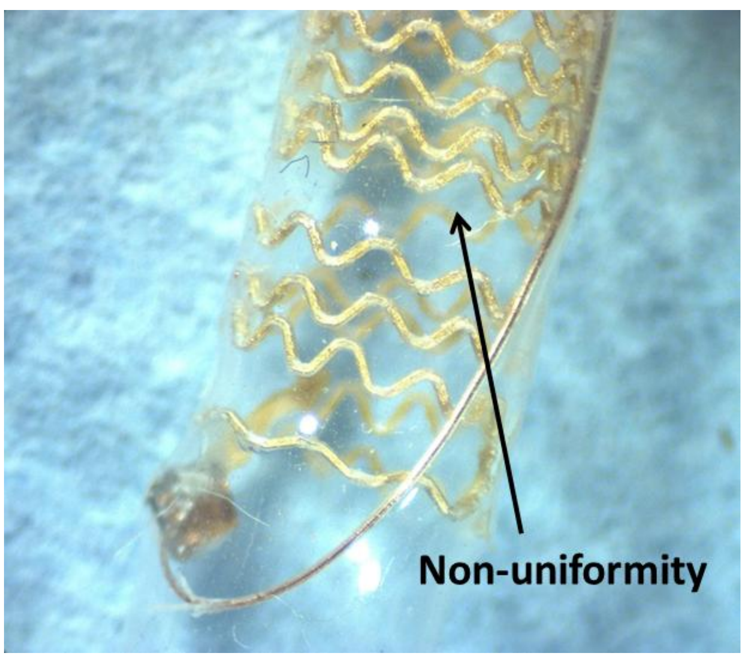

FIGURE 3.5: Non-Uniform Expansion to 5 mm Diameter
A typical helical stent expanded to a diameter of 5 mm showing non-uniformity in the spacing between its loops.

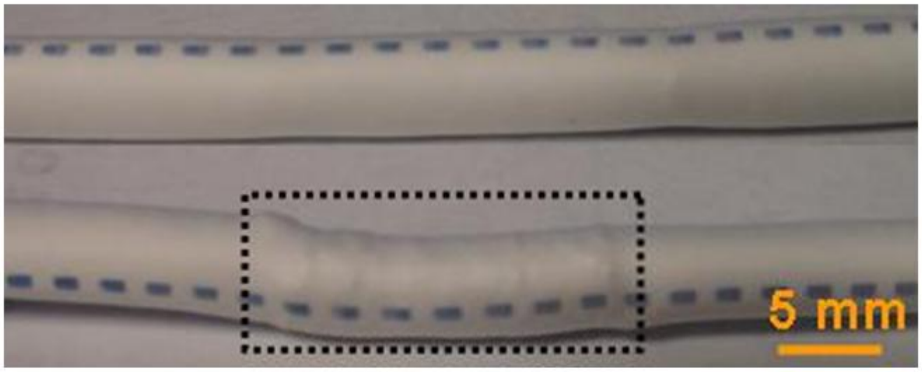

FIGURE 3.6: Deployment in a Vascular Graft
Two grafts, one with and one without devices expanded inside. The dashed frame indicates the position of the stent deployed in the bottom graft.

related to failures of the wire bonded region, apparently due to tangling between the bridging wire and balloon occurring during removal of the deflated balloon from the expanded device.

Further deployment testing was conducted in commercial vascular grafts (GORE- TEX® Stretch Vascular Graft, W. L. Gore & Associates, INC.) with 5 mm diameters. Grafts are fabric tubes, commonly supported by stents to form ‘stent grafts’ that are used to reinforce weak spots in arteries known as aneurysms. Stent grafts also suffer from restenosis [56], and a means of monitoring their internal pressure might be a useful diagnostic tool. An image of an integrated device deployed in a graft is shown in Fig. 3.6.

3.4 Device Testing

After deployment of integrated stent/sensor devices, they were tested in different environments to characterize their overall performances. In each case, impedance measurements of wire loops placed in proximity to integrated devices were used to track their resonant frequencies. *In vitro* responses of various devices to pressure, temperature, and flow rate were recorded.

3.4.1 Wireless Testing in Air

Prior to testing integrated devices in liquid, their response to pressure changes in air was characterized. Devices were placed in a plastic syringe whose internal pressure was manually adjusted and measured with a commercial pressure sensor (Omega Engineering PX-26) connected to its end. Devices inside the syringe were inductively coupled with external coils located within 3 mm of the syringe wall. Impedance measurements of external coils were made using an Agilent 4396B impedance analyzer to track shifts in device resonant frequency (f_R) with applied pressure.

Pressure responses of a typical device measured before and after expansion (2mm ⇒ 5mm diameter) are shown in Fig. 3.7. Before expansion, applying a gauge pressure of 250 mmHg shifted the device resonant frequency from 153.3 MHz to 148.1 MHz, for a sensitivity of 137 ppm/mmHg. After expansion, due to the increase in stent inductance, the device resonant frequency at atmospheric pressure dropped to 81.9 MHz. The same 250 mmHg pressure differential applied to the device in its expanded state reduced its resonant frequency from 81.9 MHz to 78.9 MHz, for a sensitivity of 146 ppm/mmHg. Also, due to the increased inductance of the expanded stent, the tank quality factor $\left(Q = \frac{1}{R}\sqrt{\frac{L}{C}}\right)$ increased from 23 to 30. This, together with increased magnetic coupling between the expanded stent and the external coil accounts for the significantly enhanced resonant peak depth shown in Fig. 3.7.

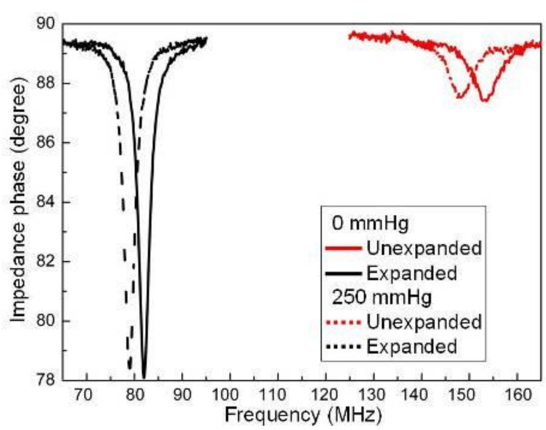

FIGURE 3.7: Device Resonant Peak Shift Before and After Expansion

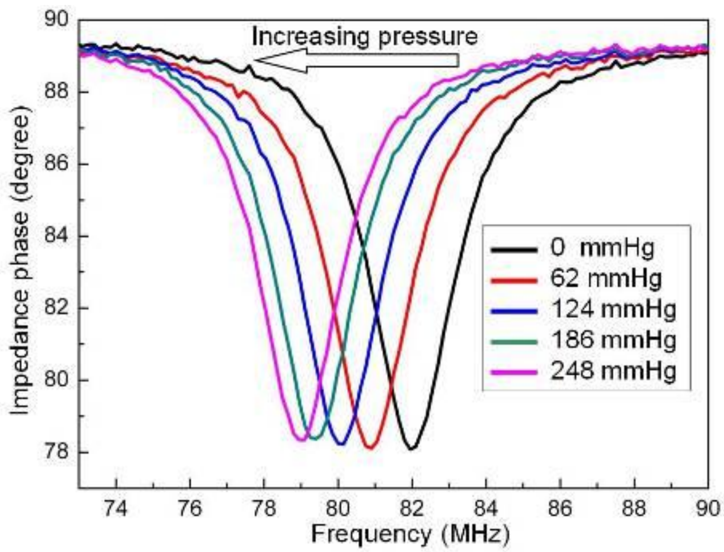

FIGURE 3.8: Expanded Device Resonant Peak Shift with Applied Pressure

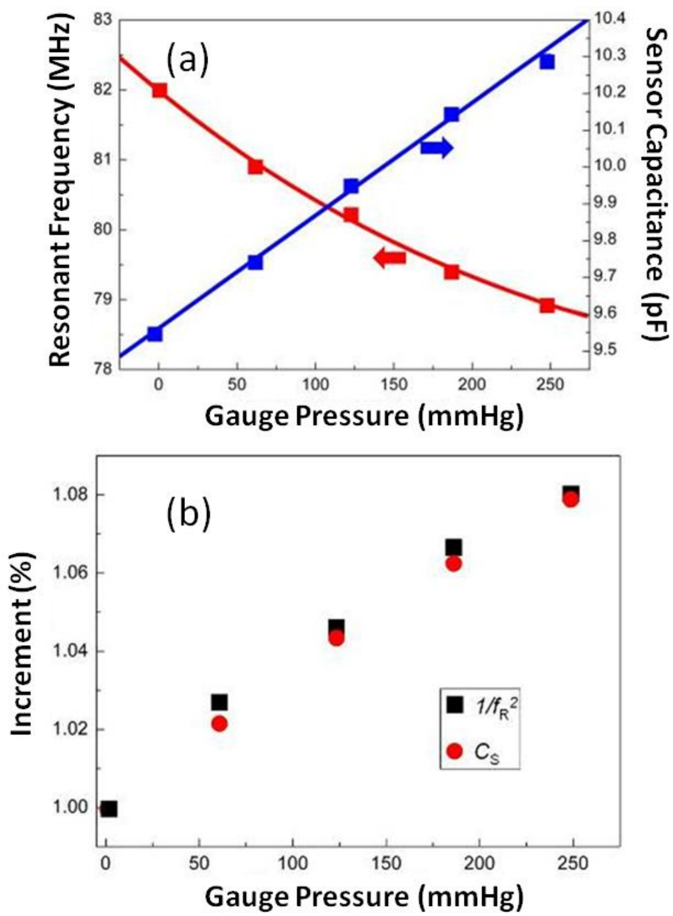

FIGURE 3.9: Consistency of Sensor and Integrated Device Pressure Response

(a) Response of sensor capacitance C_S and device resonant frequency f_R to applied pressure and (b) a renormalized comparison of $1/f_R^2$ and C_S.

Fig. 3.8 shows resonant peaks detected from the same expanded device while varying the applied pressure from 0 mmHg to 250 mmHg. A clear shift of the resonant frequency with applied pressure is visible (12 kHz/mmHg).

In theory, shifts in device resonant frequency are strictly due to changes in sensor capacitance (C_S). To see if this held true, the capacitive response of a standalone sensor before integration and the frequency response of a device in which it was incorporated were measured and compared. The results are plotted in Fig. 3.9(a). Theoretically, since $f_R = \frac{1}{2\pi\sqrt{LC}}$, $1/f_R^2$ and C_S should be in proportion. Fig. 3.9(b) shows the same results re-parameterized to better observe this relationship. The plot verifies that the experimentally observed relationship between f_R and C_S is in good agreement with theoretical expectation, and that the device is correctly converting changes in applied pressure to shifts in resonant frequency.

3.4.2 Wireless Testing in Conductive Media

When an integrated device without insulation is immersed in an electrically conductive medium, it loses its electrical function as shown in Fig. 3.10. This figure indicates that an almost complete loss of the resonant peak present in air occurs when the device is immersed in saline.

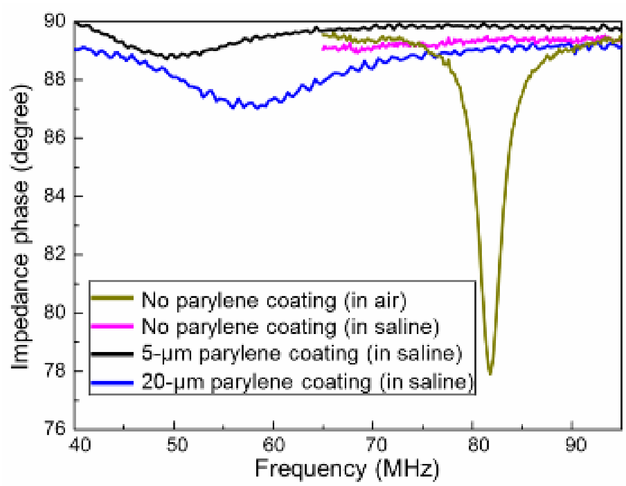

FIGURE 3.10: Electrical Performance in a Conductive Medium
Resonant behaviour of an integrated device immersed in air and saline for different Parylene coating thicknesses.

Since the device should function in the bloodstream, and blood is a conductive liquid, this is a significant problem. As a solution, Parylene, a biocompatible polymer, is conformally coated over the entire device to prevent degradation of its electrical performance; the thicker the coating, the less device resonance is affected by its environment. The drawback of doing this is that thicker coatings decrease the sensitivity of the device's capacitive sensor by increasing its membrane stiffness. Therefore, to determine a coating thickness of Parylene providing a reasonable trade-off between device electrical insulation and sensor sensitivity, the resonant response of an integrated device was tested in 0.15 M phosphate buffered saline (PBS) with different Parylene coating thicknesses. The first coating was 5 μm, and the second coating was 15 μm, for a total coating thickness of 20 μm. As apparent from Fig. 3.10, the thick 20 μm coating provided the best environmental insulation, resulting in the device showing the largest resonant peak. However, the pressure sensitivity of the integrated device was almost halved by the first 5 μm deposition of Parylene (Fig. 3.11), and further reduced by the second 15 μm coating. Given this severe reduction in sensitivity, Parylene coating was performed in two steps

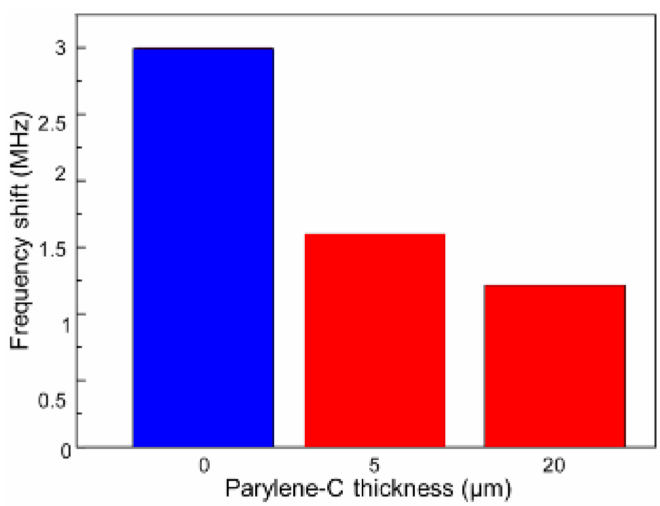

FIGURE 3.11: Effect of Parylene Coating on Device Sensitivity
Total device resonant frequency shift for 250mmHg of applied pressure when coated with 0, 5, and 20 μm of Parylene.

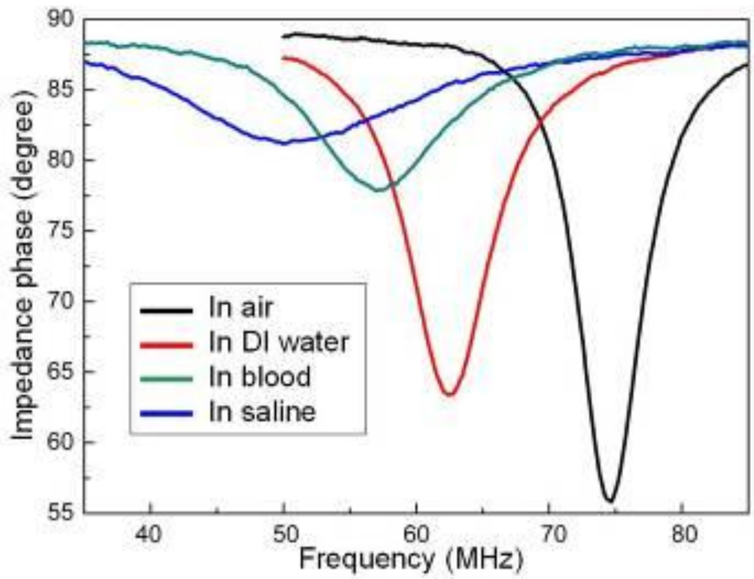

FIGURE 3.12: Device Resonance in Different Media

Resonant behaviour of an integrated device coated with a two-step Parylene coating immersed in different media.

as described in Section 3.3, i.e., a thick layer (20 - 30 μm) of Parylene was coated on the helical stent prior to sensor integration, followed by a thin coating (2 - 3 μm) of Parylene afterwards. This process was found to provide the best trade-off between electrical insulation and device sensitivity.

Fig. 3.12 shows the resonant behavior an integrated device coated with the two-step Parylene deposition immersed in different liquids: deionized (DI) water, saline (10% PBS), and animal (sheep's) blood. The resonant frequency of the device (at atmospheric pressure) shifted from 74.5 MHz down to 62.6 MHz, 57.2 MHz, and 50.2 MHz as the device was moved from air to DI water, blood, and saline, respectively. The drops in resonant frequency were accompanied by reductions in depth and quality of the resonant peak. Table 3.2 summarizes the resonant frequency and quality factor measurements of the device immersed in air and the three fluids. These trends are explained by the high relative permittivities and conductivities of the fluids, which tend to decrease immersed device resonant frequency and damp oscillation. Similar observations have been reported for LC tank devices studied in other work [57].

TABLE 3.2: **Comparison of Device Resonant Behaviour in Different Media**

Medium	Conductivity (mS/cm)	Resonant frequency (MHz)	Quality factor
Air	N/A	74.5	18.6
DI water	0.035	63.5	12.5
Sheep blood	6.2	57	6.7
Saline	16.4	49.8	3.2

3.4.3 Wireless Testing in a Circulating Fluid

Device performance was also characterized in a custom designed circulation system. The setup shown in Fig. 3.13 uses a commercial pump (Haake F423, Thermo Fisher Scientific Inc.) to heat and circulate fluid (16.4 mS/cm saline) through silicone tubing. Each device under test was deployed in a vascular graft with 5 mm diameter, and coupled to the circulation loop between two manual valves connected upstream (valve-1) and downstream (valve-2) of the device position relative to the pump. Opening and closing the valves to different extents allowed control of the flow of saline through the device. A commercial pressure sensor (24PC,

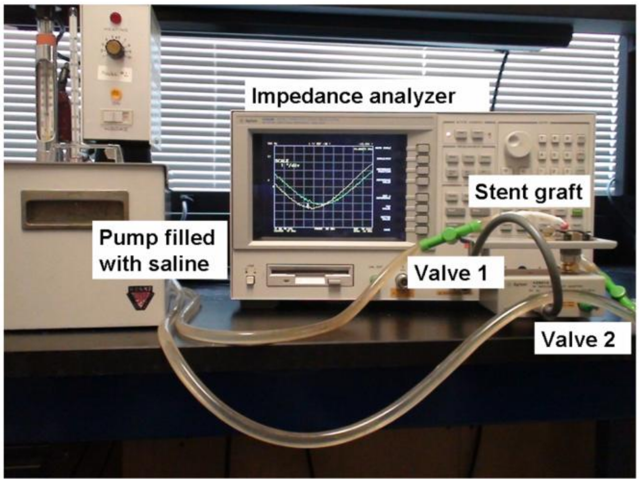

FIGURE 3.13: ***In Vitro*** **Flow Test Setup**
Photo of the test setup showing the pump, circulation loop, graft, and valves.

Honeywell Sensing and Control, USA) was connected to the loop between the two valves to monitor the pressure inside the tubing. As before, changes in device resonant frequency were read wirelessly using an external coil inductively coupled with the device.

Measurement results obtained with two different devices are plotted in Fig. 3.14(a). In these measurements, valve-2 downstream was left open, and valve-1 upstream was adjusted to regulate the flow. This mimics the situation in which in-stent restenosis occurs proximal to the stent, gradually obstructing blood flow. The flow rate achieved a maximum value of 900 mL/min with valve-1 fully opened (typical coronary artery flow is 100-200 mL/min). As valve-1 was closed, the flow rate decreased, and Fig. 3.14(a) plots the internal (gauge) pressure inside the device as a function of flow rate. The pressure attained a maximum value of 78 mmHg with valve-1 fully opened, and gradually dropped to zero as the flow rate was lowered by closing valve-1. A gradual decrease in device resonant frequency with increased flow rate was observed with an average frequency vs flow sensitivity of 10.6 ppm per mL/min.

Another flow test was conducted with a different graft device in the same flow setup. To start, valve-1 was fully closed and valve-2 fully opened, achieving a state of zero flow and atmospheric internal pressure inside the device, characteristic of complete proximal obstruction. Next, valve-1 was gradually opened until both valves were fully opened, permitting maximum flow (900 mL/min) through the system. Finally, valve-2 was gradually closed, reducing the flow until a state of complete distal obstruction was reached. In this state, the flow was zero, and the device internal pressure attained a new maximum value of 180 mmHg. The measurement results shown in Fig. 3.14(b) indicate a nearly linear response of device resonant frequency with applied pressure (78 ppm/mmHg). The graft device sensitivity is approximately half the sensitivity of the device discussed in Section 3.4.2 (for measurements in air), because of differences in

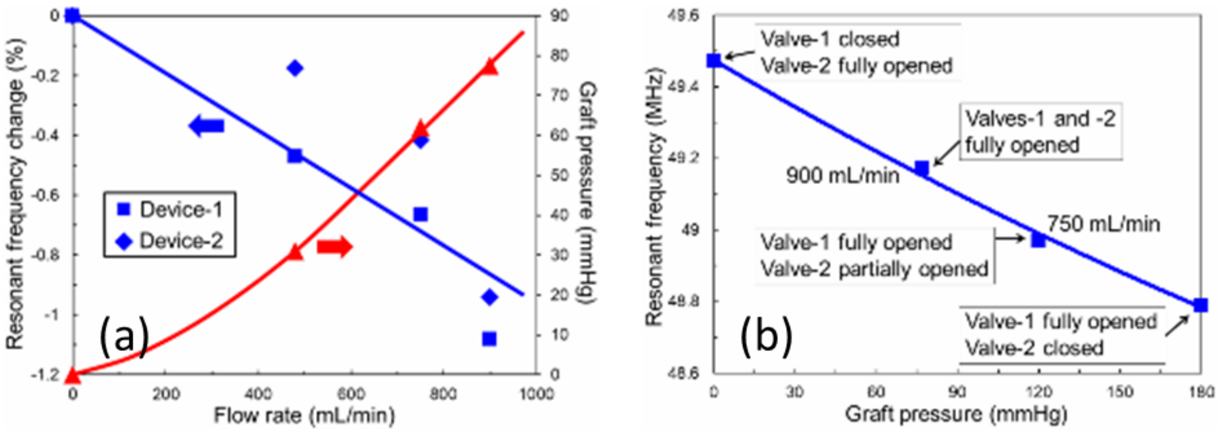

FIGURE 3.14: ***In Vitro*** **Flow Test Results**
(a) Changes in graft device resonant frequency and internal pressure with varied flow inside the circulation system.
(b) Changes in resonant frequency of a second graft device induced by a different valving sequence.

sensitivity of the integrated sensors.

3.5 Discussion

New approaches were adopted to improve upon previous LC tank telemetric stent devices [15,20] and produce a new device. *In vitro* tests showed the devices responded to pressure over a (gauge) pressure range of 0 - 200 mmHg, and identified the primary challenges to the inductive stent design approach that must be overcome to achieve clinically relevant restenosis monitoring:

1. **Crimping:** Deployment testing showed difficulties in crimping devices tightly to balloon catheters to pass through sheaths available for testing (Fig. 3.15). This is a problem, because the passage of stents through a sheath is part of the standard technique used to insert stents *in vivo* (Seldinger technique). Furthermore, the external bridging wire used to complete device tank circuits would not always crimp tightly to the stent body, and occasionally catch on vessel walls and/or tangle with the expanded balloon during device deployment.

   One obstacle to achieving tight crimping was the thick Parylene coating on devices used to improve electrical performance in conductive media; stents without Parylene coating have been observed to crimp more tightly. Thus, it is possible that the crimping problem may be

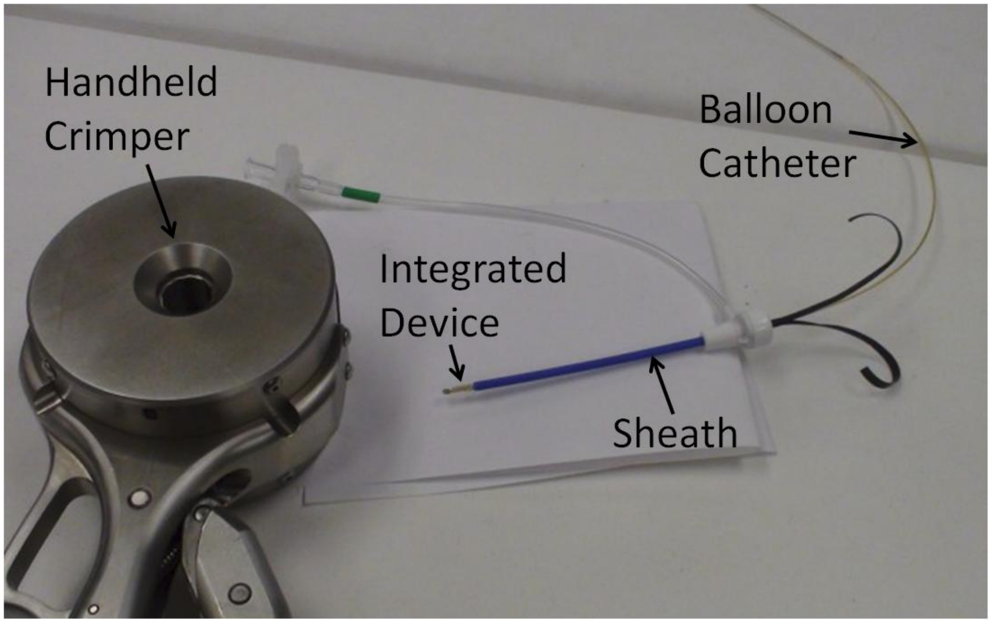

FIGURE 3.15: Integrated Device Crimping and Deployment
A handheld crimper was used to crimp integrated devices to balloon catheters before passing them through sheaths to test viability of standard deployment techniques. Devices were not crimped tightly enough to be passed through sheaths consistently.

alleviated by reducing the thickness of the Parylene coating and carefully choosing the stent wire thickness and balloon catheter size, although this remains to be tested. The effect of crimping on sensor performance and the propensity for the external wire to get damaged during insertion also require further in-depth analysis.

2. **Expansion:** To improve the mutual inductance of the stents with external antennae, their struts were removed. In stent expansion to small diameters (3 mm), this has not been observed to cause any visible non-uniformity. However, all stents expanded to diameters ≥ 5 mm have visible non-uniformity along their axis due to stretching and compression (Fig. 3.5). To help alleviate this problem, longer 4 cm balloons were used for deployment, since shorter balloons were observed to cause extreme non-uniformity of stent expansion, and even buckling. This current performance is not in accordance with ISO 25539 commercial stent standards, which require reliable and repeatable stent expansion. It is likely that by re-designing the stent zig-zag

pattern and/or replacing some of its removed struts, more uniform expansion to large diameters can be achieved reliably. However, additional struts decrease stent-reader mutual inductance, thereby decreasing read range, so whether or not an ISO 25539 compatible stent design can be found that is useful for the intended in-stent restenosis monitoring application is unclear at present. Clarification of this issue requires direct experimentation with improved inductive stent designs.

3. **Mechanical Reliability:** No ISO 25539 compliant mechanical testing (eg. radial stiffness testing, stress/strain analysis, fatigue testing) of strutless stents used in the experiments of this chapter has yet been conducted. One expects that the removal of struts from a stent reduces structural integrity by allowing new stretching/compression and spiral contraction modes of motion, degrading stenting performance. Therefore, stent re-design may be necessary to ensure compliance with industry standards. The issue of how to ensure long term stability of sensor-stent bonds for *in vivo* implantation also needs further examination. Techniques such as micro-welding and direct fabrication of the sensor on the stent are currently under investigation for solving this problem.

4. **Sensing Range and Resolution*:*** *In vitro* tests revealed that device resonant signals could not be read at antenna-device distances >1.5 cm, which is not adequate for monitoring stents implanted in coronary arteries. Also, although shifts in device resonant frequency under large ~62 mmHg static pressures were observed, no ability to resolve shifts in resonant frequency under smaller dynamic pressure changes occurring *in vivo* has yet been observed.

An ideal monitor would resolve a 1mmHg change in blood pressure at a device-reader distance of ~3.5 cm to monitor a coronary artery. If monitoring a carotid artery is adopted as an intermediate goal (restenosis also occurs in the carotid arteries [58]), a read distance of ~2.5 cm is required [59]. In either case, the current sensing range and resolution must be significantly increased to achieve clinical relevance. To this end, progress may be achieved by further improving reader design, external antennae, device quality factor, device-antenna alignment (with angled configuration or antenna wrapped around the body), and pressure sensor sensitivity. The extent to which such improvements can increase device sensing range and resolution requires a dedicated study of device telemetric properties.

5. **Diagnostic Utility:** Although the devices tested in this research utilize a single sensor at one end of the stent, two sensors at both ends of the stent are needed to perform fractional flow reserve (FFR) measurement across a (re)stenosis to diagnose its severity. To obtain two independent pressure readings instead of one, a device must have two LC tanks instead of one. This can be achieved by using two external wires that connect each sensor to the center of the stent to form two separate tanks [20]. This increases the complexity of the device, and a more robust means of making all the wire connections is essential. Whether a practical means of making these wire connections compatible with stent delivery requires further study.

   Additionally, the accuracy of each pressure measurement depends on the accuracy of each resonant frequency measurement, and since the resonant frequency depends on the electrical impedances of the expanded stent, external wire, and capacitive sensor, there is the question of how non-uniform final configurations of the stent and wire (eg. stretching/compression and variations in expanded stent diameter) and variations in sensor performance affect pressure measurement. In theory, if the inductance after expansion and capacitive sensor specifications are known precisely, the pressure experienced by the sensor can be calculated precisely from device resonant frequency. However, all experiments thus far have shown variations in stent expanded configuration and sensor performance that shift device resonant frequency in an unpredictable manner. Because of these variations, no ability to determine sensor capacitance (and thereby obtain a pressure reading) from deployed device resonant frequency has yet been demonstrated. This problem is exemplified by two graft devices that were prepared in an identical manner, but observed to have resonant frequencies of 29 MHz and 63 MHz respectively, primarily due to differences in sensor capacitance.

By sensor redesign or individual calibration of integrated devices prior to deployment, variations in sensor may be accounted for, and with stent redesign, variation in expanded stent inductance may be greatly reduced, allowing for approximate determination of absolute pressure from device resonant frequency. Tracking changes in this single resonant frequency may already provide useful information to physicians for assessing stent performance, although this remains to be tested. To obtain more comprehensive information, two sensors may be integrated with a stent, one at each of its ends [20], with additional external wiring to form two independent LC tanks. Readings of the two tank frequencies should be sufficient for approximating both sensor pressure readings, and enable computation of the FFR across the stent. The accuracy with which this calculation can be made and its diagnostic utility *in vivo* are important areas of future research.

Note that many of the problems listed result from the helical stent design in which all struts have been removed. In light of this, proposals for telemetric stents that do not require strut removal are made in Chapters 5 and 6. In Chapter 4, a closer examination of device telemetric properties is undertaken to better understand the fundamental/practical limitations to increasing sensing range.

Chapter 4: Wireless Range Testing

The conventional method of reading the resonant frequency of an LC tank device utilizes an impedance analyzer to measure the phase of an inductive coil placed in proximity to the device, since a plot of the coil's impedance phase versus frequency reveals the device's resonant peak. As the coil is moved away from the device, this dip gets smaller, and eventually is not observable against the noise floor of the analyzer. In tests of the sensing range achievable by this method, resonant peaks of integrated devices (in air) at antenna-device distances of more than 1.5 cm were not observable. A distance between the antenna and device of more than 1.5 cm, and ideally 5 cm, is necessary to implement wireless monitoring of stents in the vast majority of patients and locations. Furthermore, a general feature of any LC tank device is that its wireless read range depends strongly on its relative orientation with the external antenna, and since implanted stents run in directions parallel to the skin surface, a large sensing distance at less than optimal alignment must be obtained to ensure efficacy. This challenge motivates the experiments in this chapter, designed to determine the read range of LC tank devices. Two different methods, the impedance phase method and ring-down method, are explored as means of probing devices, and a maximum read distance of 2.75 cm is obtained for an inductive stent based device using the ring-down method. This is the first work to apply the ring-down method to read inductive stent based tank devices and identify the barriers to extending sensing range further.

4.1 Impedance Phase Method

4.1. Basic Theory

The impedance phase method for wirelessly determing the resonant frequency of an LC

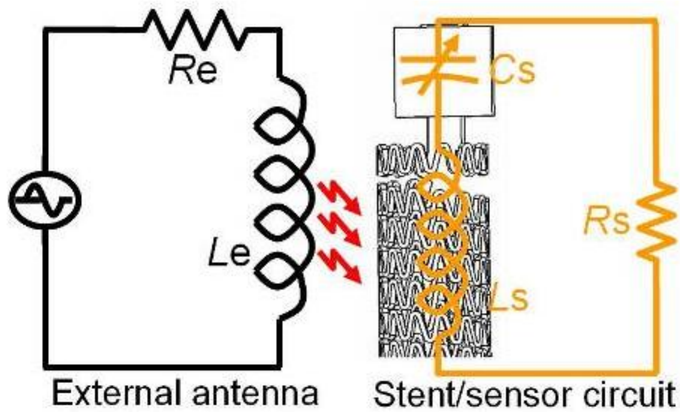

FIGURE 4.1: Impedance Phase Method for Detecting LC Tank Resonance

tank is shown in Fig. 4.1. The method works by measuring the impedance $Z_e = R_e + j\omega L_e$ of an external coil (antenna) placed in proximity to the tank at various (angular) frequencies ω, since there is a characteristic dip in the phase of the impedance at the resonant frequency.

To see why, let V_e be the voltage across the source in the external coil, and Z_s be the series impedance around the resonant circuit. Kirchoff's law applied to both the external and resonant circuits yields the equations:

$$V_e = Z_e I_e - M\frac{dI_s}{dt} \quad (1)$$

$$0 = Z_s I_s - M\frac{dI_e}{dt} \quad (2)$$

Now, assuming variables $V_e, I_e,$ and I_s are complex numbers encoding phase and amplitude information (only the real part is considered physically relevant):

$$V_e = \hat{V}_e e^{-i\omega t} \quad I_e = \hat{I}_e e^{-i\omega t} \quad I_s = \hat{I}_s e^{-i\omega t}$$

these equations become:

$$\hat{V}_e = Z_e \hat{I}_e + i\omega M \hat{I}_s \quad (3)$$

$$0 = Z_s \hat{I}_s + i\omega M \hat{I}_e \quad (4)$$

$$\Rightarrow |\hat{I}_s| = \frac{\omega M|\hat{I}_e|}{|Z_s|} \quad (5)$$

$$\Rightarrow \frac{\hat{V}_e}{\hat{I}_e} = Z_e + \frac{\omega^2 M^2}{Z_s} = R_e + j\omega L_e + \frac{\omega^2 M^2}{Z_s} \quad (6)$$

where:

$$Z_s = \left(j\omega L_s + R_s + {}^{1}\!/_{j\omega C_s}\right) \quad (7)$$

Recall that the resonant frequency ω_r of the tank is defined as the frequency where the maximum current amplitude is excited in the circuit when the amplitude of the external circuit current is specified. It follows from the relation:

$$\frac{|\hat{I}_s|}{|\hat{I}_e|} = \frac{\omega M}{|Z_s|} \quad (8)$$

that ω_r is the frequency maximizing ${}^{\omega}\!/_{|Z_s|}$, which turns out to be $\omega_r = \sqrt{\frac{1}{L_s C_s} - \frac{R_s^2}{L_s^2}}$.

The natural resonant frequency ω_0 of the loop is defined as the frequency where the imaginary part of the impedance around the loop $Im(Z_s(\omega_0)) = 0$, so $\omega_0 = {}^{1}\!/_{\sqrt{L_s C_s}}$. Assuming

$Q^2 = \frac{1}{R_s^2}\frac{L_s}{C_s} \gg 1$, the expressions for ω_r and ω_0 are roughly equal:

$$\omega_r \approx \omega_0 = {}^{1}\!/_{\sqrt{L_s C_s}} \quad (9)$$

This assumption is generally true for MEMs LC tank implants found in the literature and integrated devices studied in Chapter 3, since use of higher Q devices enables better sensing range and resolution. With a little algebra, the externally measured impedance may be written as:

$$\frac{\hat{V}_e}{\hat{I}_e} = R_e + j\omega L_e + \frac{\omega^2 M^2}{Z_s} = R_e + j\omega L_e \left(1 + \frac{j\omega C_s}{j\omega L_e} \frac{\omega^2 M^2}{1 - \omega^2 L_s C_s + j\omega R_s C_s}\right) \quad (10)$$

which, neglecting the external resistance and defining the geometric coupling constant as $k = {}^{M}\!/\!\sqrt{L_e L_s}$, gives:

$$\frac{\hat{V}_e}{\hat{I}_e} = j\omega L_e \left(1 + \frac{k^2\left(\frac{\omega}{\omega_r}\right)^2}{1 - \left(\frac{\omega}{\omega_r}\right)^2 + \frac{j}{Q}\left(\frac{\omega}{\omega_r}\right)}\right) \quad (11)$$

When the second term inside the brackets is real, the measured impedance is purely inductive with a phase of 90°. However, when the second term has a significant imaginary component, the second terms inside the brackets in the above equation generate a dip in the phase of the external impedance ${}^{\hat{V}_e}\!/\!{}_{\hat{I}_e}$. The magnitude of this dip is obtained by substituting $\omega = \omega_r$ in the above expression, yielding:

$$\frac{\hat{V}_e}{\hat{I}_e} = j\omega L_e (1 - jk^2 Q) \quad (12)$$

so that the phase dips by an amount $\tan^{-1}(k^2 Q)$ below $90^\circ = {}^{\pi}\!/_{2}$ at resonance. Fig. 4.2 shows an analyzer trace (140 MHz – 170 MHz) of the impedance phase of an antenna coupled to a dummy LC resonator. Away from resonance the phase is 90°, but it dips to 77.5° at resonance.

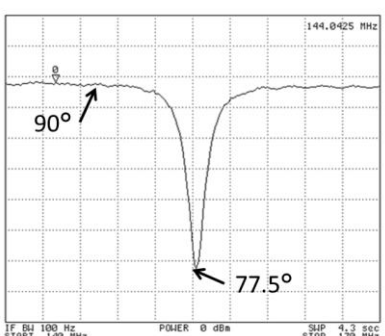

FIGURE 4.2: Impedance Phase of an Antenna Magnetically Coupled to a LC Tank
$(f_r = 155.3\ MHz, L = 220\ nH, C = 4.7\ pF, Q = 96)$

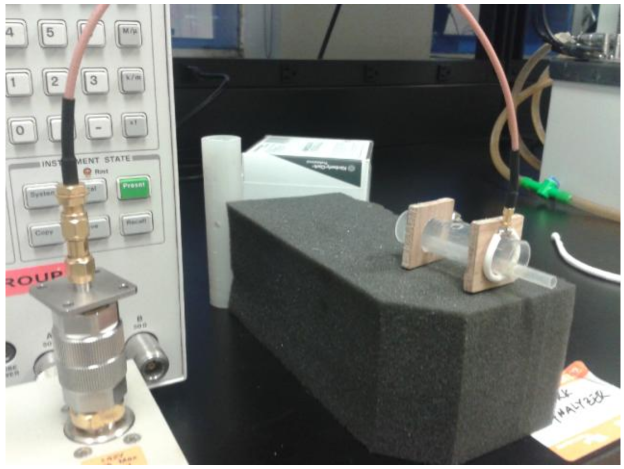

FIGURE 4.3: Antenna-Device Configuration for Determining Tank Resonant Frequency

4.1.2 Preliminary Experimental Results

Initial experiments were conducted to get a rough idea of integrated device wireless sensing range. Two devices were used in the test, one deployed in a mock artery, and the other in a graft. To measure the resonant frequency of each device, devices were threaded through a loop antenna (2 cm diameter) as the antenna's impedance phase was recorded on an Agilent 4396B impedance analyzer (with 43961A RF impedance analysis adapter). The experimental configuration with the mock artery device under test is shown in Fig. 4.3.

The analyzer traces of the impedance phase measurements (30 - 60 MHz, 15 dBm source

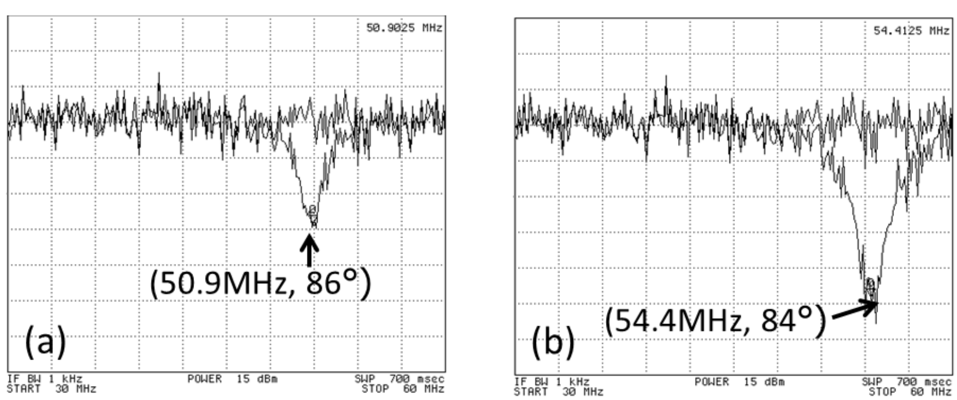

FIGURE 4.4: Device Resonant Peaks
(a) Mock artery and (b) graft device resonant peaks observed on the impedance analyzer.

power) for both the mock artery and graft devices are shown in Fig. 4.4, and identify the device resonant frequencies as 50.9 MHz and 54.4 MHz respectively. The respective phase dips are 3º and 5º below the 89 - 90º impedance phase baseline. The phase measurements obtained before device insertion are also shown in the plots, and account for the continuation of the baseline above the resonant peaks.

Phase measurements were also made as devices were pulled out of the loop antenna. In both cases, once the entire length of the device was withdrawn from the loop, the size of the phase dip was too small to be observed against the analyzer baseline noise (Fig. 4.5).

To test more realistic antenna-device configurations, devices were threaded through and centered inside a graduated syringe, in parallel with the loop antenna plane (Fig. 4.6). Using this setup, impedance phase measurements were obtained for different angles of device rotation and antenna-device distances. The mock artery device was observed to have minimal and maximal coupling with the antenna at angles of rotation separated by 90º. At maximal coupling, the resonant phase dip had a magnitude of 2.5º (Fig. 4.7(a)), while at minimal coupling it could not be observed at all (Fig. 4.5).

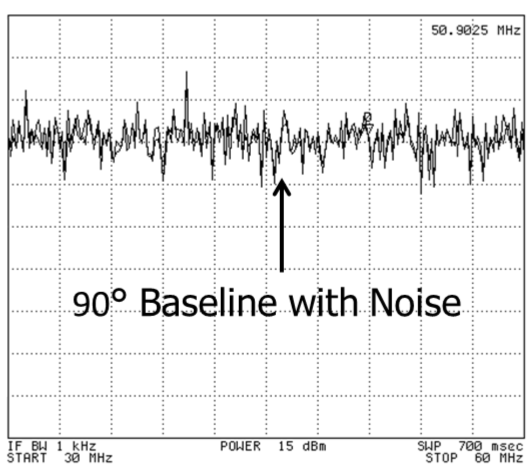

FIGURE 4.5: Analyzer Baseline with Noise
Once devices were withdrawn to the point their stents did not intersect the antenna plane, phase dips were not large enough to be observed against the analyzer baseline noise.

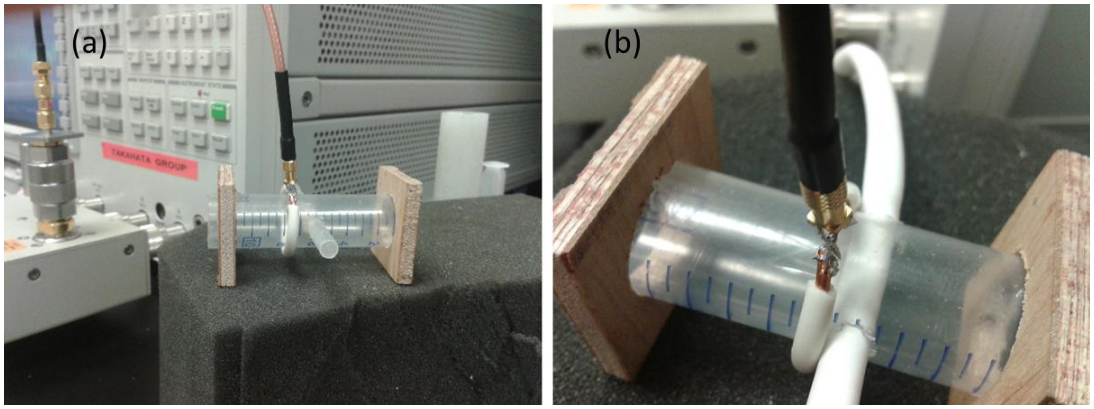

FIGURE 4.6: Range Test with Parallel Antenna-Device Alignment
Impedance phase measurements made with the antenna plane aligned in parallel to (a) mock artery and (b) graft devices.

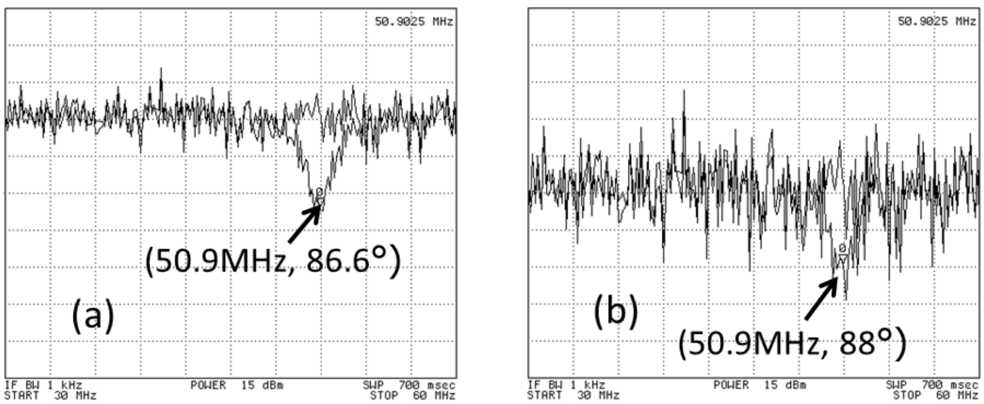

FIGURE 4.7: Range Test with Parallel Antenna-Device Alignment Results
Resonant peaks observable from the mock artery device for parallel alignment at distances of (a) 0 cm and (b) 0.25 cm.

Keeping the device at its optimal orientation, the antenna was then moved away from the device one syringe gradation (0.25 cm) at a time. The phase dip was still observable at an antenna-device distance of 0.25 cm (Fig. 4.7(b)), but not 0.5 cm. In the case of the graft device (Fig. 4.6(b)), even at 0 cm, no angle of rotation was found to generate a phase dip large enough to be observable on the analyzer screen. The greater read range of the mock artery device is due to it having a thicker electroplated coating and a longer bridging wire used to connect its ends, enhancing device quality factor and inductive coupling with the reader antenna. The graft device used a thinner electroplated coating and much shorter bridging wire to make it more practical for *in vivo* deployment.

4.1.3 Method Optimization

The preliminary experiments were not successful in obtaining any data from devices at distances ≥ 0.5 cm, and show vast improvements to sensing methodology are needed to obtain useful information from devices at distances relevant to in-stent monitoring. Several possible areas of improvement are considered in this section.

4.1.3.1 Loop Antenna: Size, Turns, and Orientation

To compute the geometric coupling between an external coil and our integrated device is difficult because of the complicated device geometry. Not only are there many turns with zigzag features, but there is also an external wire completing the circuit whose final position varies considerably from device to device. Thus, to some extent, the appropriate choice of external coil size and number of turns for achieving long distance sensing is best determined by direct experimentation. However, to obtain an intuition about how the size of the phase dip signal read from a device depends on antenna-device distance, we can study a toy LC tank model consisting of a wire loop of radius b with N_L turns.

Assume the tank loop shares its central axis with a simple loop antenna of radius a a distance r away. In this circumstance, the near magnetic field B_z generated by the external coil along its central axis is [60]:

$$B_z = \frac{\mu_0 I_{ex} N_{ex} a^2}{2(a^2+r^2)^{3/2}} \quad (13)$$

where μ_0 is the magnetic permeability of free space, and I_e and N_e are the current amplitude and number of turns of the antenna. By Faraday's law of induction, the voltage induced in the tank is:

$$V_L = -N_L \frac{d\Psi}{dt} \quad (14)$$

where $\Psi \approx \pi b^2 B_z$ is an approximation of the magnetic flux through the resonator, valid when $a \gg b$ and the magnetic field does not vary considerably over the area of the tank loop. Recalling that the equation defining the mutual inductance M of the antenna and loop is:

$$V_L = -M \frac{dI_e}{dt} \quad (15)$$

the following formula for the mutual inductance is obtained:

$$M \approx \frac{\mu_0 \pi N_L N_e a^2 b^2}{2(a^2+r^2)^{3/2}} \quad (16)$$

Now, since the size of the phase dip is given by:

$$\Delta\varphi = \tan^{-1}(k^2 Q) \approx k^2 Q \text{ for } k^2 Q \ll 1 \quad (17)$$

where k is the geometric coupling:

$$k = \frac{M}{\sqrt{L_{ex} L_{LC}}} \quad (18)$$

it follows that:

$$\Delta\varphi \approx k^2 Q \approx \frac{\mu_0^2 \pi^2 N_L^2 N_{ex}^2 a^4 b^4 Q}{4 L_{ex} L_{LC} (a^2+r^2)^3} \quad (19)$$

From this equation, to compute the dependence of the phase dip on tank/antenna size and separation, it only remains to compute the tank and antenna self inductances. One approximation [61], which assumes the loop and coil are solenoids of lengths l_e and l_L wrapped with infinitely thin wire, gives:

$$L_e = \mu_0 a N_e^2 \left(\ln \frac{8a}{l_e} - \frac{1}{2}\right) \quad (20)$$

$$L_L = \mu_0 b N_L^2 \left(\ln \frac{8b}{l_L} - \frac{1}{2}\right) \quad (21)$$

Substitution of these formulae into the expression for the phase dip yields:

$$\Delta\varphi \ \propto \ \left(\frac{ab}{a^2+r^2}\right)^3 \qquad (22)$$

For a given loop radius b and loop-coil distance r, this expression is maximized by taking $a = r$, so that:

$$\Delta\varphi \ \propto \ \frac{b^3}{r^3} \qquad (23)$$

Many assumptions have gone into the derivation of equation (23), but 2 general conclusions can be drawn from it. First, to observe the largest phase dip from a resonant device at a distance r away, the optimal choice for the loop antenna radius is approximately r, and not much larger or smaller. Second, the size of the phase dip drops off rapidly with the cube of the separation distance, so that minimization of the impedance analyzer noise floor is essential for seeing the phase dip at large distances.

Another interesting theoretical fact is that the derived expressions for geometric coupling and phase dip have no dependence on the number of tank/antenna turns. This is misleading, since the derivation assumed the antenna and tank were wrapped with ideal wires, while in reality the wires are insulated, have nonzero diameter, and may be wound in non-solenoidal patterns. Therefore, the approximate formulae derived do not take into account complexities of the winding geometry, and thus do not suggest an optimal number of turns to use in the antenna. This problem is most easily solved empirically, by constructing coils of the same radius with different wires and turn numbers, and measuring their performance. This process has been carried out, and is described in the next section containing experimental results.

Finally, one more way to increase the antenna-device geometric coupling is to find orientations of the external antenna and device that give unexpectedly large couplings. Although

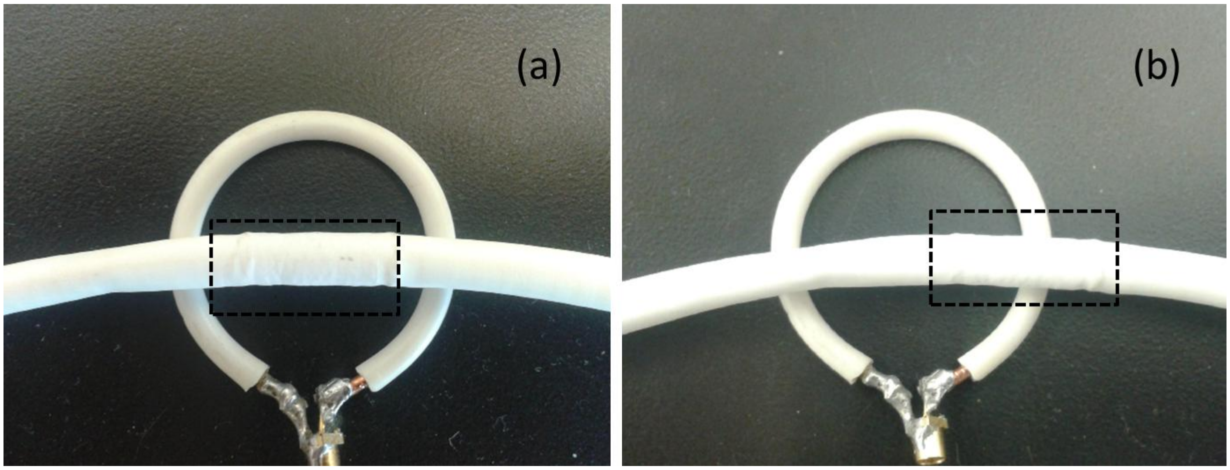

FIGURE 4.8: Antenna-Device Alignment for Enhanced Coupling
Antenna-device coupling is improved by shifting the device from the (a) center of the antenna to its (b) perimeter

the best case scenario of looping the device through the middle of the loop antenna is not an option for *in vivo* monitoring, an experimentation shows that for short sensing distances $r \ll a$ and parallel alignment of the loop antenna plane and device axis, the best coupling is achieved by centering the device over a section of the loop perimeter (Fig. 4.8). This is superior to centering the device over the middle of the loop antenna because the near magnetic field of the loop curves at its edges, increasing the magnetic flux through the loops of the nearby stent. This fact can be used to increase the detected phase dip at short distances, but does not change the long distance $\Delta\varphi \propto \frac{1}{r^3}$ relationship between phase dip and antenna-device distance.

4.1.3.2 Impedance Analysis

Although the size of the detected phase dip is determined by the geometric coupling of the antenna and device, and the device quality factor, the ability to see this dip on an impedance analyzer depends on the analyzer's noise. To get a better understanding of this noise and to what extent it can be reduced, it is necessary to understand how impedance analyzers operate.

One technique (RF I-V method) for measuring impedance employed by the Agilent 4396B is shown in Fig. 4.9. In this method, the analyzer's variable frequency oscillator (VFO)

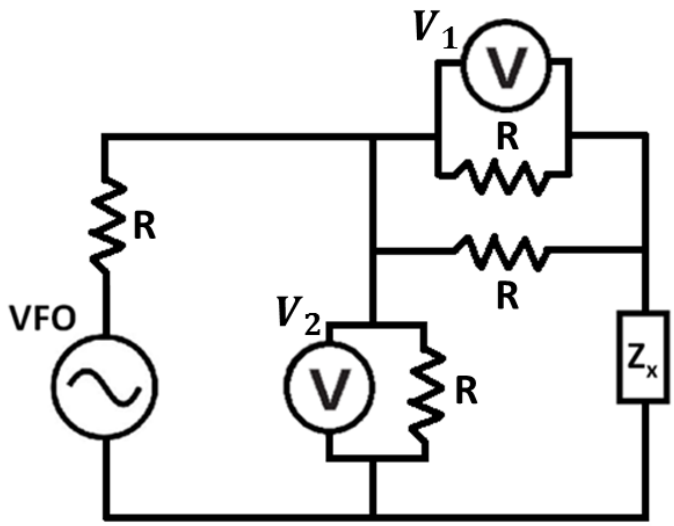

FIGURE 4.9: RF I-V Impedance Measurement

output is sent through a network of resistors to the device under test, and two separate voltage measurements, V_1 and V_2, are made by down-converting (mixing with a local oscillator and filtering at an intermediate frequency (IF)) and digital sampling to determine their magnitude and relative phase. This information is sufficient to compute the device impedance Z_x:

$$Z_x = \frac{R}{2}\left(\frac{V_1+V_2}{V_1}\right) \quad (24)$$

since the voltage across the impedance is $V_1 + V_2$, and the current it draws is ${V_1}/{\left(\frac{R}{2}\right)}$. Therefore, precision measurement of Z_x relies on precision measurement of V_1 and V_2, and is affected by several factors including environmental noise, VFO signal power, IF resolution bandwidth (RBW), and impedance analyzer noise figure.

In the case of interest, where the impedance being analyzed is a loop antenna, environmental noise consists of thermal noise and any additional electrical signals picked up by the antenna due to its surroundings. By choosing the largest possible VFO signal power (limited only by analyzer specifications and biological radiation exposure guidelines), its degrading effect on signal measurement minimized. For the Agilent 4396B, the maximum incident signal power is 20 dBm.

To further minimize measurement noise, the analyzer IF bandwidth can be set to the minimum possible value. On the Agilent 4396B, this minimum is 10 Hz. However, it is important to note that the smaller the filter bandwidth, the longer it takes to make an impedance measurement at a particular frequency, since the rise/stabilization time of the IF filter is inversely proportional to its bandwidth [62]:

$$Rise\ time = \frac{k}{RBW} \quad (25)$$

(k ≈ 2 for the Gaussian filters used in Agilent analyzers). This is relevant to the restenosis monitoring application of interest, because blood pressure is dynamic, and the sampling frequency must be high enough to ensure stability of the pressure and tank resonance over the sampling period. A rough estimate might be that a monitor should obtain 100 measurements each cardiac cycle to effectively track variations in blood pressure. Since a cardiac cycle takes ~1 s, this is equivalent to a 100 Hz sampling frequency (10 ms per measurement). Because the 4396B shortens filter rise times by using digital IF filtering techniques at small IF bandwidths (10 Hz - 3 kHz), it achieves a single frequency impedance measurement time of 10 ms for $RBW = 100$Hz, so an analyzer IF resolution bandwidth of 100Hz is selected as the smallest bandwidth useful for the intended application.

Further effects of impedance analyzer noise figure on measurement precision are considered in Section 4.1.4.

4.1.3.3 Signal Processing

When the impedance phase of a loop antenna dips at the resonant frequency f_R of a magnetically coupled LC tank, the minimum phase does not occur precisely at $f_{min} = f_R$, but at:

$$f_{min} = f_R\left(1 + \frac{k^2}{4} + \frac{1}{8Q^2}\right) \quad (26)$$

To see this, set $x = \frac{f}{f_R}$ and solve for the position of the minimum phase by minimizing the function:

$$f(x) = 1 + \frac{k^2x^2}{1-x^2+\frac{j}{Q}x} \quad (27)$$

Setting the derivative of the ratio of imaginary and real parts of $f(x)$ to zero yields:

$$x^4(1 - k^2) + \left(2 - k^2 - \frac{1}{Q^2}\right)x^2 - 3 = 0 \quad (28)$$

Because k^2 and $1/_{Q^2} \ll 1$, we can solve for corrections to the solution $x = 1$ by setting $x = (1 + \epsilon)$ and keeping only first order terms to obtain:

$$(1 + 4\epsilon)(1 - k^2) + \left(2 - k^2 - \frac{1}{Q^2}\right)(1 + 2\epsilon) - 3 = 0 \quad (29)$$

$$\Rightarrow \left(1 - k^2 + 4\epsilon\right) + \left(2 - k^2 - \frac{1}{Q^2} + 4\epsilon\right) - 3 = 0 \quad (30)$$

$$\Rightarrow \epsilon = \frac{k^2}{4} + \frac{1}{8Q^2} \quad (31)$$

$$\Rightarrow x = \left(1 + \frac{k^2}{4} + \frac{1}{8Q^2}\right) \quad (32)$$

This relationship between f_{min} and f_R is valid so long as k is less than some critical geometric coupling $k_c(Q)$, where the loop antenna and resonant loop take on qualitatively different resonant behavior due to strong coupling. Its existence demonstrates that to measure the resonant frequency, it is not adequate to measure the impedance phase of an antenna over a set of predetermined frequencies and take the frequency where the phase is minimized as the resonant frequency of the LC tank under test. Also, although it is true that $f_{min} \approx f_R$ for antenna-device distances where magnetic coupling is weak ($k \ll 1$), the presence of impedance analyzer noise makes the location of the antenna impedance phase absolute minimum difficult to identify since it obscures the shape and position of the resonant peak. Therefore, a more refined method of estimating the parameters k, Q, and f_R from a set of noisy impedance analyzer measurements is needed.

To illustrate such method, assume $k^2Q \ll 1$, so that $\tan^{-1}(k^2Q) \approx k^2Q$, and the antenna impedance phase is:

$$phase\left(\frac{\hat{V}_e}{\hat{I}_e}\right) = \frac{\pi}{2} + phase\left(1 + \frac{k^2\left(\frac{f}{f_R}\right)^2}{1-\left(\frac{f}{f_R}\right)^2 + \frac{j}{Q}\left(\frac{f}{f_R}\right)}\right) \quad (33)$$

By computing the phase and its second derivative at its minimum:

$$\frac{f}{f_R} = 1 + \frac{k^2}{4} + \frac{1}{8Q^2} \quad (34)$$

coefficients of a second degree polynomial (in f) approximating the phase are obtained:

$$phase\left(\frac{\hat{V}_e}{\hat{I}_e}\right) \approx \frac{\pi}{2} - 4k^2Q^3\left(\frac{f}{f_R} - 1 - \frac{k^2}{4} - \frac{1}{8Q^2}\right)^2 + k^2Q \quad (35)$$

This expression enables determination of $k, Q,$ and f_R from coefficients a, b, c of a polynomial $p(x) = ax^2 + bx + c$ found by least squares fitting to a dataset of impedance measurements [63]. This approach to parameter estimation is called curve fitting, and the fitting by quadratic forms used here is only one of many possible algorithms (eg. the conjugate gradient method [64]).

To see how this works, assume that the impedance analyzer phase noise (standard deviation) is $\Delta\varphi_{noise} = 0.1^{\circ} = 0.0017$ rad. Further assume that the LC tank quality factor is $Q = 30$, and the geometric coupling k of the antenna and tank is such that the maximum signal to noise ratio (SNR) at resonance is 10:

$$\frac{\Delta\varphi_{signal}}{\Delta\varphi_{noise}} = 10 \quad (36)$$

$$\Rightarrow \frac{k^2 Q}{0.0017} = 10 \quad (37)$$

$$\Rightarrow k = 0.024 \quad (38)$$

Taking normalized frequency units (f_R = 1), we can simulate the process of data taking and curve fitting by evaluating $phase\left(\frac{\hat{V}_e}{\hat{I}_e}\right)$ on a set of sample frequencies, adding phase noise to the data, and running the curve fitting / parameter computation algorithm to determine the effect of phase noise on the output. Fig. 4.10 shows the result for sample frequencies equally spaced in the interval (0.99, 1.01). As one might expect, the normalized frequency uncertainty satisfies:

$$\frac{\Delta f}{f_R} \propto \frac{1}{\sqrt{N}} \quad (39)$$

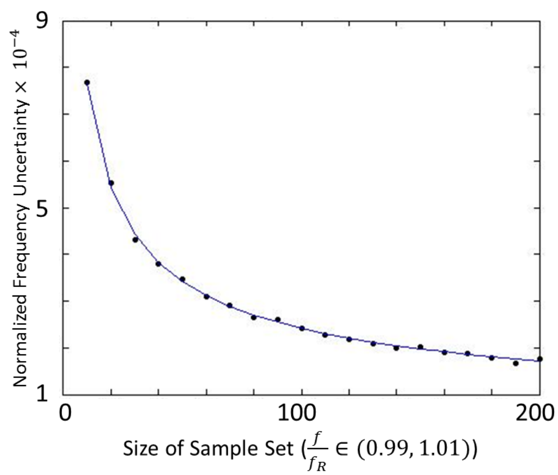

FIGURE 4.10: Curve Fitting Frequency Uncertainty $\frac{\Delta f}{f_R}$ vs Sample Size

where N is the number of samples in the interval.

Since there is also freedom in choosing the set of frequencies to sample at, it is useful to understand better the dependence of frequency uncertainty on the chosen sample set. The range of frequencies at which data may be sampled is limited by $\Delta\varphi_{noise}$, since for frequencies sufficiently far from resonance, the impedance phase dip is masked by the noise floor. For instance, the phase dip (k = 0.024, Q = 30):

$$phase\left(1+\frac{k^2\left(\frac{\omega}{\omega_r}\right)^2}{1-\left(\frac{\omega}{\omega_r}\right)^2+\frac{j}{Q}\left(\frac{\omega}{\omega_r}\right)}\right) \quad (40)$$

evaluated at $\frac{f}{f_R}=1$ is equal to k^2Q, while evaluated at $\frac{f}{f_R}=1.04$ is $\approx\frac{k^2Q}{10}$. Thus for SNR = 10, it is not useful to sample at frequencies larger than$1.04\ \times\ f_R$.

Sampling the impedance at 20 equally spaced points in a frequency range centered at $\frac{f}{f_R}=1$, the frequency uncertainty due to analyzer noise is plotted in Fig. 4.11 (k = 0.024, Q = 30, SNR = 10, N = 20). The high uncertainties associated with the first two data points are due to

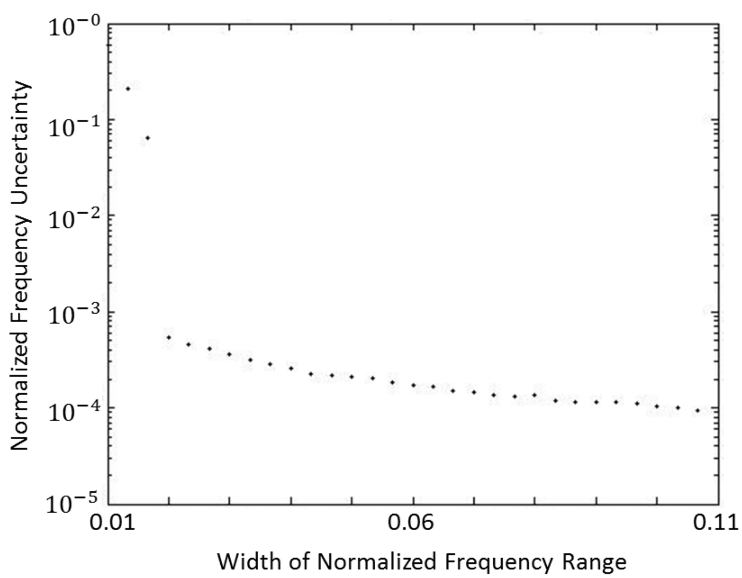

FIGURE 4.11: Curve Fitting Frequency Uncertainty $\frac{\Delta f}{f_R}$ vs Sample Range Width

inability of the quadratic fitting algorithm to construct a good quadratic approximation to the phase minimum from highly clustered data points. The rest of the uncertainties follow a regular trend suggesting optimal resonant frequency determination is made by choosing the widest possible range of sample frequencies, which is intuitive because this improves accuracy of curve fitting. Since measurement time is strictly a function of the number of measurement points (frequencies) and impedance analyzer RBW, there is no drawback to doing this.

4.1.4 Secondary Experimental Results

To improve upon preliminary experimental results, firstly, the coupling of different antennae with integrated devices was investigated. For this, antennae of two different wire thicknesses (AWG 20 = 0.82 mm and AWG 28 = 0.32 mm) and various turn numbers (1,3,5, and 7) were tested to see which gave the largest phase dip signals. The antennae, shown in Fig. 4.12(a), have 1 cm radii for optimal coupling at 1cm antenna-device distance.

The same mock artery and graft devices as used in the preliminary range test were tested

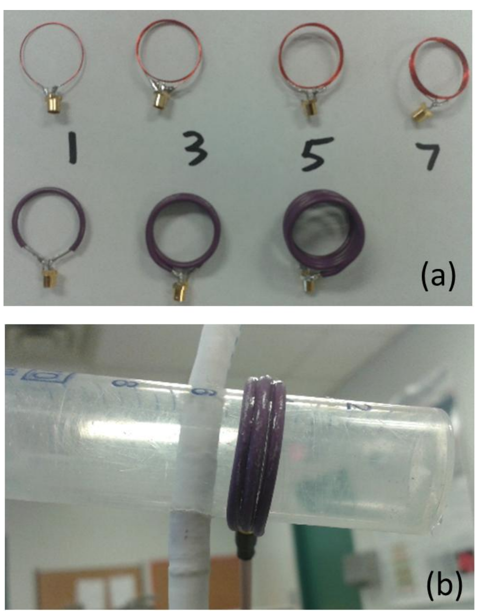

FIGURE 4.12: Testing Different Antennae for Maximal Coupling
(a) 2 cm diameter antennae with 2 different thicknesses (red: AWG 28, purple: AWG 20) and 1,3,5, or 7 turns. (b) A 3 turn purple antenna positioned 0.25 cm away from the graft device to record the phase dip.

with each antenna and the alignment shown in Fig. 4.12(b). In each test, devices were positioned to record the maximal phase dip at antenna-device distances of 0 and 0.25 cm. This is why the graft device shown in Fig. 4.12(b) is centered along the perimeter of the antenna for enhanced coupling. Table 4.1 shows the results of this test. The largest phase dips were observed using the red (AWG 28) antenna with 3 turns, so this antenna was used for subsequent testing.

TABLE 4.1: **Phase Dips Obtained with Different Antenna-Device Couplings**

	Mock Artery Coupling Distance 0 cm	**Graft Coupling Distance 0 cm**	**Mock Artery Coupling Distance 0.25 cm**	**Graft Coupling Distance 0.25 cm**
AWG 28 1 turn	6°	2.5°	2°	1°
AWG 28 3 turn	46°	35°	18°	10°
AWG 28 5 turn	22°	5.5°	11°	2.5°
AWG 28 7 turn	5.5°	1.5°	1.5°	0.5°
AWG 20 1 turn	5.5°	3°	2°	1°
AWG 20 turn	17.5°	9°	4.5°	3°
AWG 20 turn	31.5°	3°	9°	1°

Next, to better understand the analyzer's internal noise, several measurements were made with no cable or antenna connection to its input. In this state, the impedance under test was a very small 73 fF parasitic capacitance, with a -90° phase. The standard deviations of the impedance magnitude and phase were recorded at several frequencies and analyzer settings, and the results are shown in Tables 4.2 - 4.4. As expected, the analyzer noise in each of the measured quantities decreases as the source power is increased and the IF resolution bandwidth is decreased. Table 4.5 shows results of similar measurements when the 2 cm diameter, 3 turn loop antenna is connected via 15 cm of SMA cable to the analyzer. The changes in sign of the

TABLE 4.2: **73 fF Impedance Measurements – 0 dBm Source Power, 40 kHz RBW**

Frequency	**Impedance Magnitude (**kΩ) $(\lvert Z\rvert, \Delta\lvert Z\rvert)$	**Impedance Phase** $(\theta_Z, \Delta\theta_Z)$
25 MHz	(120, 93.1)	(-89.5°, 42.6°)
50 MHz	(47.3, 11.1)	(-90.0°, 12.5°)
100 MHz	(21.4, 2.3)	(-90.0°, 6.0°)
200 MHz	(11.1, 0.8)	(-89.3°, 3.7°)
400 MHz	(5.5, 0.2)	(-89.6°, 1.8°)

TABLE 4.3: **73 fF Impedance Measurements – 20 dBm Source Power, 40 kHz RBW**

Frequency	**Impedance Magnitude (**kΩ) $(\lvert Z\rvert, \Delta\lvert Z\rvert)$	**Impedance Phase** $(\theta_Z, \Delta\theta_Z)$
25 MHz	(87.7, 3.4)	(-89.5°, 2.2°)
50 MHz	(43.3, 0.9)	(-90.3°, 1.2°)
100 MHz	(21.8, 0.2)	(-89.9°, 0.75°)
200 MHz	(10.9, 0.1)	(-89.7°, 0.6°)
400 MHz	(5.4, 0.02)	(-90.1°, 0.49°)

TABLE 4.4: **73 fF Impedance Measurements – 20 dBm Source Power, 100 Hz RBW**

Frequency	**Impedance Magnitude** (kΩ) $(\lvert Z\rvert, \Delta\lvert Z\rvert)$	**Impedance Phase** $(\theta_Z, \Delta\theta_Z)$
25 MHz	(87.4, 0.2)	(-89.8°, 0.37°)
50 MHz	(43.6, 0.1)	(-89.9°, 0.34°)
100 MHz	(21.8, 0.03)	(-90.0°, 0.33°)
200 MHz	(11.1, 0.06)	(-90.7°, 0.32°)
400 MHz	(5.4, 0.04)	(-90.2°, 0.28°)

TABLE 4.5: **Antenna Impedance Measurements – 20 dBm Source Power, 100 Hz RBW**

Frequency	**Impedance Magnitude** (Ω) $(\lvert Z\rvert, \Delta\lvert Z\rvert)$	**Impedance Phase** $(\theta_Z, \Delta\theta_Z)$
25 MHz	(65, 0.013)	(89.5°, 0.024°)
50 MHz	(293.3, 0.027)	(89.0°, 0.023°)
100 MHz	(125.1, 0.014)	(-89.7°, 0.026°)
200 MHz	(22.0, 0.012)	(-88.4°, 0.022°)
400 MHz	(65.3, 0.014)	(87.6°, 0.023°)

antenna's impedance phase are indicative of the antenna's self-resonance at 62.5 MHz and 260 MHz.

Using the 3 turn antenna with 20 dBm source power and 100 Hz RBW, measurements of device resonance at different antenna-device distances were made. 3 devices were tested in this second experiment: the same mock artery (Fig. 4.13(a)) and graft devices as before

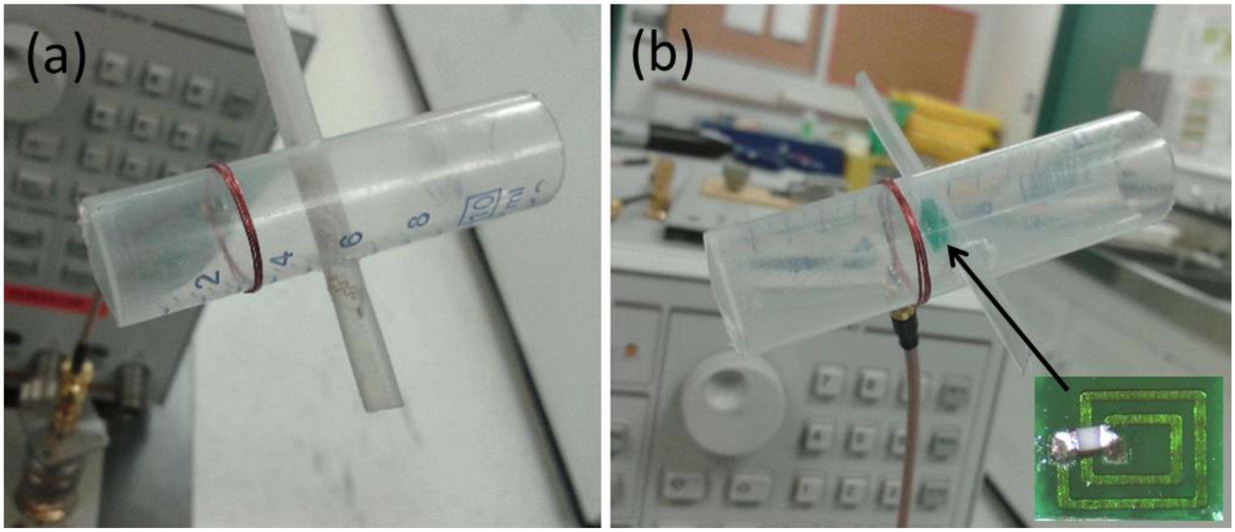

FIGURE 4.13: Modified Range Test Setup
(a) A mock artery device being probed from 1cm away. (b) An LC tank dummy device being probed from 0.5 cm away.

(Fig. 4.12(b)), and a dummy planar LC tank (Fig. 4.13(b)). The planar tank was comprised of a two turn printed circuit board (PCB) spiral inductor (outer dimension 2.5 mm, 0.25 mm trace width) soldered together with a 68 pF surface mount capacitor.

For each device and antenna-device distance, the best quadratic approximation to the antenna's resonant phase dip was made in a 5 MHz window around the resonant frequency (20 measurement points, 0.4s sweep time), and the coefficients of this quadratic were used to compute k, Q, and f_R as described in Section 4.1.3. Impedance phase measurements made in the absence of any LC tank device were also fed into computations as calibration data to reduce background noise. The results are shown in Tables 4.6 - 4.8. Beyond the distances listed in each table, antenna-device coupling was too weak for the signal processing algorithm to return reliable results. As in the preliminary experiment, the mock artery device showed the greatest read range (1.5 cm). Interestingly, the graft and planar LC tank devices showed the same read range (0.75 cm).

TABLE 4.6: **k, Q, and f_R Computed for Different Antenna-Mock Artery Device Distances**

Distance (cm)	**k**	**Q**	**f_R (MHz)**
0	1.66×10^{-1}	25.6	50.37
0.25	9.66×10^{-2}	24.2	50.57
0.5	5.58×10^{-2}	24.7	50.68
0.75	4.03×10^{-2}	23.0	50.70
1	2.91×10^{-2}	17.6	50.75
1.25	2.04×10^{-2}	15.8	50.67
1.5	1.64×10^{-2}	15.3	50.75

TABLE 4.7: **k, Q, and f_R Computed for Different Antenna-Graft Device Distances**

Distance (cm)	**k**	**Q**	**f_R (MHz)**
0	1.58×10^{-1}	16.9	54.38
0.25	8.80×10^{-2}	16.6	54.75
0.5	5.95×10^{-2}	15.7	54.90
0.75	4.50×10^{-2}	12.9	54.91

TABLE 4.8: **k, Q, and f_R Computed for Different Antenna-Dummy Tank Distances**

Distance (cm)	**k**	**Q**	**f_R (MHz)**
0	2.17×10^{-2}	28.9	192.54
0.25	2.02×10^{-2}	31	192.50
0.5	1.92×10^{-2}	28.8	192.92
0.75	1.44×10^{-2}	28.7	192.1

The sensing ranges achieved improve upon the preliminary results, and highlight how changes to the antenna and impedance analyzer settings affect read range. The results also demonstrate the need for an appropriate signal processing algorithm to accurately calculate device resonant frequency from antenna impedance phase information, since the output of the quadratic fit algorithm used in the tests varied considerably with antenna-device distance. This difficulty of finding an algorithm that can calculate device resonant frequency with high resolution regardless of device environment is a drawback of the LC tank design approach to restenosis monitoring.

4.2 Ring-Down Method

In the range tests discussed in Section 4.1, even with optimization of the antenna, device, antenna-device orientation, and analyzer settings, and additional signal processing, the impedance phase method was not capable of reading device resonant frequencies at distances >1.5 cm. With the implantation of the device in a conductive medium, read range is further reduced, and initial *in vitro* experiments revealed a maximum read range of 0.5 cm for devices immersed in phosphate buffered saline with conductivity similar to blood. Although further analysis of the impedance phase method is required to fully understand its limitations, an alternative, 'ring-down', sensing method for further improving read range has been explored, and the results are presented in this section.

4.2.1 Basic Theory

The 'ring-down' method ([65-67]) operates by using one or more loop antennas to transmit a sequence of single frequency pulses that excite the LC tank device. After each pulse, a short duration is left to receive the signal from the excited resonator as its signal decays or 'rings-down'. Fig. 4.14 ([68]) shows sample transmit and receive signals to and from resonators with 3 different quality factors (Q). At resonance, the ring-down signal is largest, and 180° out of phase with the signal from the transmitter, so that either amplitude or phase analysis of the received signal can be used to determine the resonant frequency of the device under test. The phase analysis technique has been implemented in previous work [68-69] using two phase locked loops to adjust the phase and frequency of the transmit pulse until it is 180°out of phase with the ring-down signal. Another variation of this technique is shown in Fig. 4.15 ([65]), where rather than toggling the transmit signal on and off, a lock in amplifier is used to determine any small

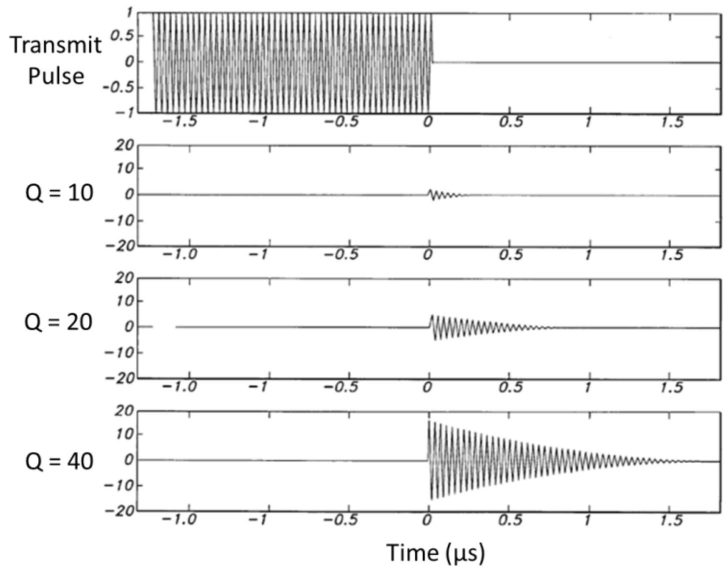

FIGURE 4.14: Ring-Down Method [68]
Transmit (excitation) and ring-down signals to and from LC tank devices with different quality factors.

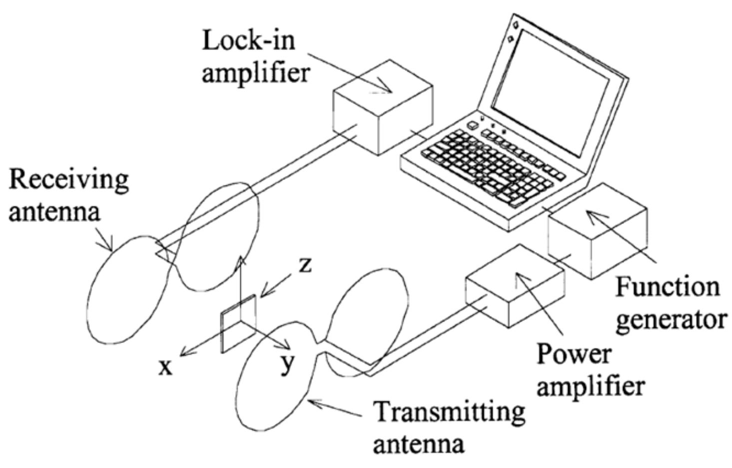

FIGURE 4.15: Phase Analysis Technique [65]
Schematic diagram of the ‘ring-down’ method using two antennas to probe the resonant frequency of an LC tank by detecting changes in the phase of the receive signal.

change in the received signal phase due to interference from the resonator.

In theory, whether using the impedance phase method or ring-down method, there is little difference between the sizes of device resonant peaks observable with a loop antenna. In fact, the induced voltage signals in the receive antennas from the resonator are:

$$impedance\ measurement: \frac{\omega^2 M^2 |\hat{I}_e|}{|Z_s|} \qquad (41)$$

$$ring\ down\ measurement: \frac{\omega^2 M_1 M_2 |\hat{I}_e|}{|Z_s|} \qquad (42)$$

where M is the mutual inductance between the transmit/receive coil and resonant device used in the impedance phase method, and M_1, M_2 are the two mutual inductances between the transmit/receive coils and the resonant device in the ring-down method. Thus it would seem that there is no significant advantage to using one method over the other.

However, in practice, using an impedance analyzer has drawbacks in that its source power is limited to 20 dBm, and its noise floor is quite high. For instance, in the Agilent 4396B impedance analyzer, the A and R channels (V_1 and V_2 in Fig. 4.9) have noise floors of -113 dBm/Hz and -93 dBm/Hz when the IF resolution bandwidth is 100 Hz. The R channel noise floor is higher because of additional attenuation in the channel used to limit incoming signals. The A channel -113 dBm/Hz noise floor suggests an analyzer noise figure of [62]:

$$NF = -113 - 10 \cdot \log\left(\frac{100}{1}\right) + 174 = 41\ dB \qquad (43)$$

which is quite high, and is made worse when the effect of the RF I-V resistive network (Fig. 4.9) is taken into account. To see this, recall that:

$$Z_x = \frac{R}{2}\left(\frac{V_1+V_2}{V_1}\right) \qquad (44)$$

from which it follows:

$$\frac{\Delta|Z_x|}{|Z_x|} \leq 2 \cdot \max \left(\frac{\Delta|V_1+V_2|}{|V_1+V_2|}, \frac{\Delta|V_1|}{|V_1|}\right) \quad (45)$$

Assuming the absence of the resistive network, and full-scale 20 dBm signal inputs to A and R channels, this suggests:

$$\frac{\Delta|Z_x|}{|Z_x|} \leq 2 \cdot \frac{rms(-93\ dBm)}{rms(20\ dBm)} = 2.24 \times 10^{-6} \quad (46)$$

which is two orders of magnitude smaller than any $\frac{\Delta|Z|}{|Z|}$ ratio computed from Tables 4.2 - 4.5. This implies that the resistive network significantly increases the noise of the impedance measurement. Because Fig. 4.9 represents a simplified schematic of a proprietary circuit, it is difficult to pinpoint the exact origins of this noise in the circuit. However, measurements of the A channel amplitude for a 20 dBm input show a signal attenuated by 25 - 35 dB for frequencies probed in Tables 4.2 - 4.5, so attenuation of the input signal by the resistive network is confirmed as one factor contributing to increased measurement noise.

In contrast, the ring-down method imposes no device limit on the transmit signal power, and no degrading attenuating elements need be included in the receive chain. Instead, a low noise amplifier and band pass filtering can be used to amplify the ring-down signal and improve measurement SNR. Previous results [65-66] suggest an order of magnitude improvement in read range is achievable by using this method.

4.2.2 Two Loop Tests

An initial experimental setup for testing the ring-down method is shown in Figs. 4.16(a), (b), and (c). A signal from a function generator is transmitted via SMA cable to a 1" diameter loop antenna. This loop antenna is coiled around a plastic syringe tube with the mock artery

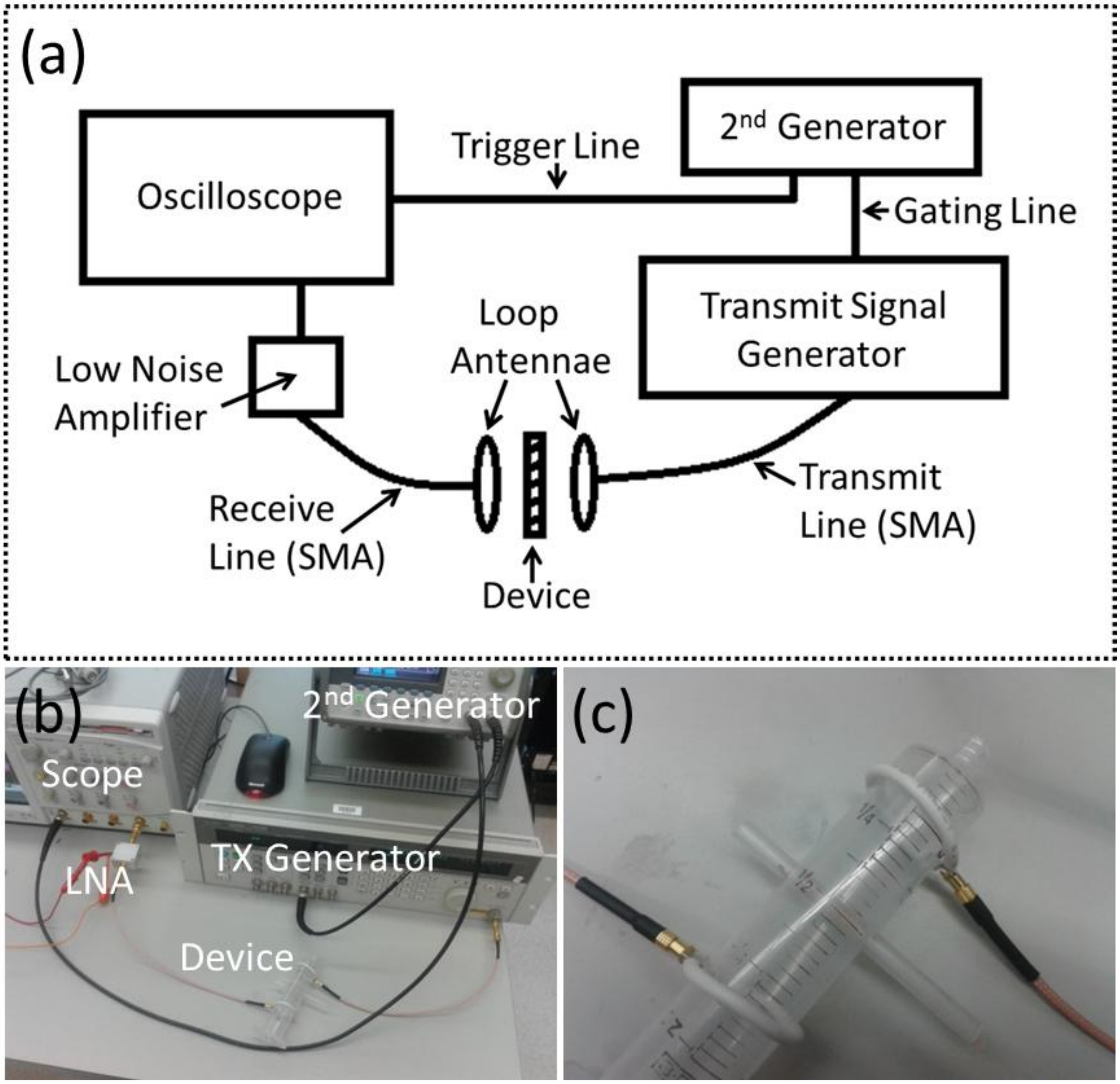

FIGURE 4.16: Ring-Down Experimental Setup
(a) Ring-down experiment block diagram. (b) Range test setup showing oscilloscope / LNA / syringe tube + device / loop antennas / and 2 function generators. (c) Close-up of mock artery device inside the syringe.

device threaded through the middle. A second identical loop antenna is coiled around the same syringe on the other side of the device, and connected via cable to an oscilloscope through a low noise amplifier (ZFL-1000LN). The transmitted signal is gated by a second function generator every second (1Hz), switched on for 1ms and then off again. A sync cable from the second generator to the oscilloscope is used to capture the gating event to observe the ring-down signal.

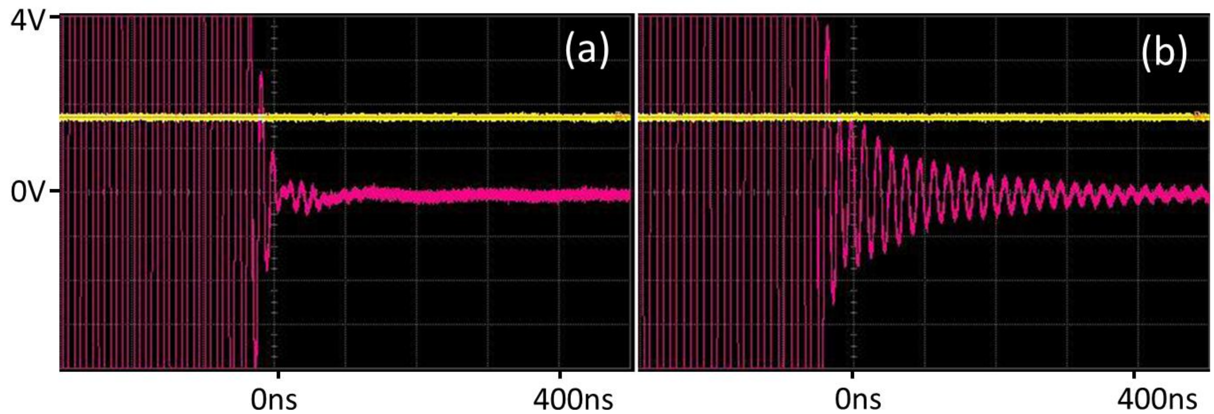

FIGURE 4.17: Ring-Down Signals from Mock Artery Device
Decay signals from device after excitation at (a) 60 MHz (far off resonance) and (b) 50.7 MHz (on resonance).

Fig. 4.17(a) and (b) show decay signals captured from the mock artery device for 20 dBm transmit pulses off (60 MHz) and on (50.7 MHz) resonance, when both antennas are adjacent to the device. The ring-down signal is clearly observable in Fig. 4.17(b).

With the LNA removed from the receive chain, the oscilloscope's average root mean square (RMS) voltage in a 100 ns - 600 ns window after turning off the transmit signal was recorded at various frequencies. Fig. 4.18 shows the results for 20 equally spaced excitation frequencies in a 2 MHz band (separated by 0.1 MHz) around resonance. The maximum windowed V_{rms} occurs at 50.5 MHz, close to the resonant frequency identified by the impedance

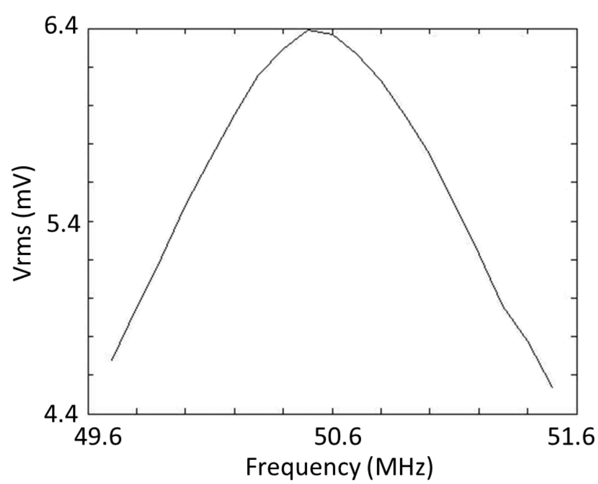

FIGURE 4.18: Ring-Down Signal V_{rms} vs Excitation Frequency
Average V_{rms} voltage measured 100 - 600 ns after transmission is gated off.

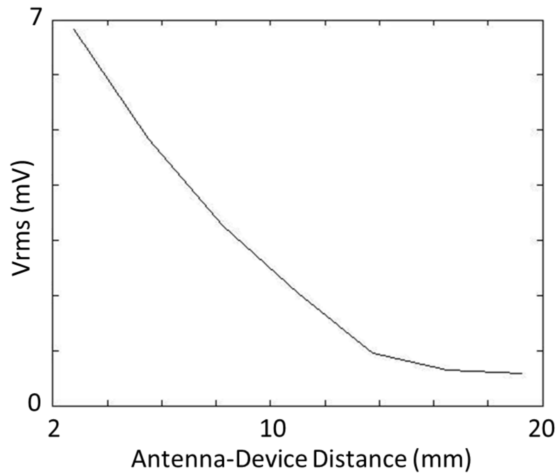

FIGURE 4.19: Resonant Ring-Down Signal V_{rms} vs Antenna-Device Distance

phase method.

Next, with the mock artery device oriented for optimal antenna coupling, the transmit and receive antennas on either side of the device were displaced along the syringe, and the windowed V_{rms} at resonance was recorded. Antenna-device distances were measured using gradations on the syringe. The results are plotted in Fig. 4.19. At 1.8 cm, the windowed V_{rms} was still larger than the scope noise floor (55 mV), and decay oscillations could be observed on the oscilloscope screen. With the 20 dB LNA in the receive chain, resonant ring-down oscillations could be observed at an antenna-device distance of 2.75 cm, as shown in Fig. 4.20. These results show that the ring-down method can be used to extend the wireless sensing range achieved in Section

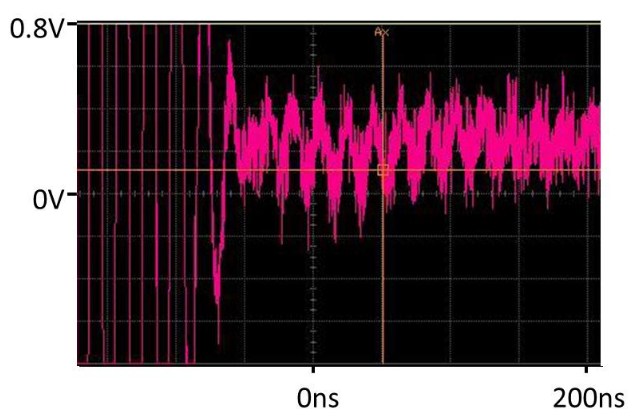

FIGURE 4.20: Ring-Down Signal Observed at 2.75 cm Antenna-Device Distance with LNA

4.1.4 using the impedance phase method.

More in depth tests were conducted with planar tank and graft devices. Antenna-device configurations are shown in Fig. 4.21. In each setup, two single turn, 2 cm diameter, AWG 28, antennae were used to couple signals in and out of devices. A 20 dBm source power was used, and the amplitudes of ring-down signals from the respective devices were recorded for different antenna-device distances. Since the ring-down signals decay with time, each amplitude was recorded at a fixed time after the excitation signal was turned off. This time was selected as 40 ns for the planar LC tank ($f_R = 192$ MHz), and 160 ns for the graft device ($f_R = 54.7$ MHz), to avoid any interference from transients remaining in the TX/RX antennae after the initial excitation. The results are shown in Fig. 4.22, and support the findings of Section 4.1.4 in which planar tank and graft devices showed similar sensing ranges. The largest antenna-device distances at which ring-down signals larger than the oscilloscope noise floor (V_{rms} = 0.4 mV) could be observed from devices was 1.25 cm. The figure also includes the amplitude of ring-down signals obtained from another planar LC tank device immersed in 7 mS/cm saline. For these measurements, the same setup as in Fig. 4.21 was used, but with the syringe filled with

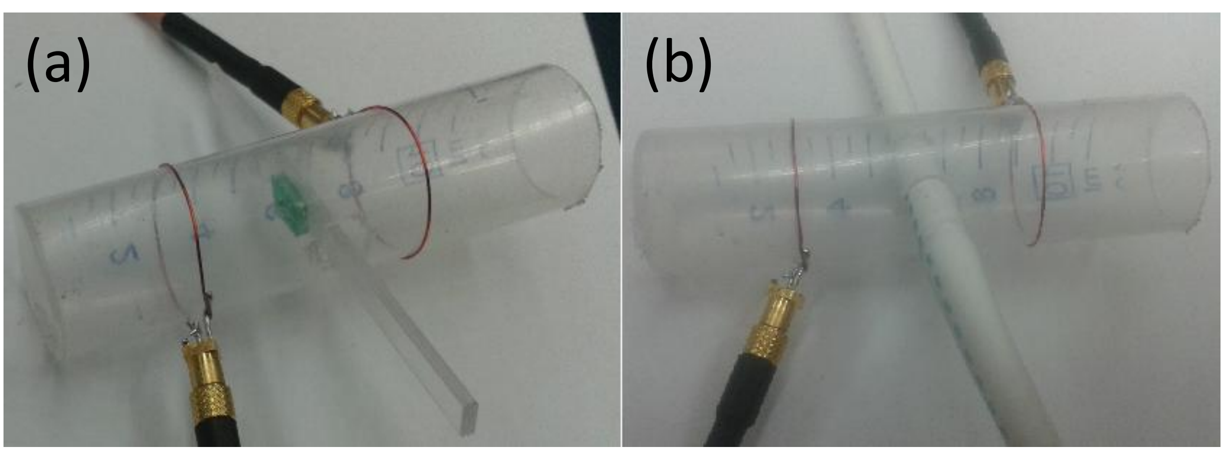

FIGURE 4.21: Planar and Graft Device Two Loop Test Setup
Antennae-device configurations for (a) planar and (b) graft device two loop ring-down testing.

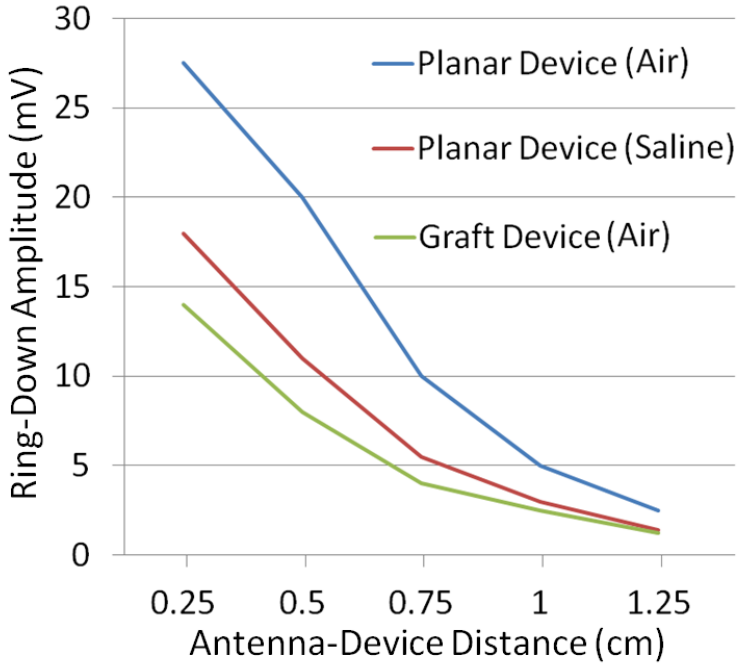

FIGURE 4.22: Two Loop Ring-Down Signal Amplitude vs Antennae-Device Distance

liquid, and the planar device coated with 3 μm of Parylene for electrical insulation. When immersed, the tank resonant frequency and quality factor were measured to be f_R = 189 MHz and Q = 16.6, decreased from their values in air (f_R = 191 MHz and Q = 26.5). These proportional changes in resonant frequency and quality factor are significantly less than those measured for integrated devices (Table 3.2), and account for the relatively large ring-down signal observed in saline.

To lower the noise floor, band pass filtering was implemented on the oscilloscope. Setting a 150 MHz - 250 MHz pass band lowered the noise floor to V_{rms} = 0.035 mV. Without the antenna, the noise floor was only slightly lower: V_{rms} = 0.03 mV. This reduction in noise floor is what one expects from the reduction in thermal noise due to reduced bandwidth, according to Johnson's formula for the root mean square thermal noise voltage across a resistor R:

$$V_N = \sqrt{4k_B TRB}$$

(k_B is Boltzmann's constant, T is temperature, and B is the noise bandwidth). This formula suggests that a reduction in scope (50 Ω input impedance) bandwidth from 13 GHz to 100 MHz should reduce the noise floor by a corresponding factor:

$$0.4\ mV \cdot \frac{1}{\sqrt{130}} = 0.035\ mV,$$

in agreement with observation.

With the noise floor lowered, sensing range was extended. Fig. 4.23 shows experimental results obtained for the planar resonator at 1.75 cm antenna-device distance. At this distance, the ring-down signal is small (amplitude 0.3 mV – Fig. 4.23(a)), and is difficult to discern against the background receive antenna transient (Fig. 4.23(b)) remaining after excitation. Subtracting these two signals (Fig. 4.23(c)) gives a clearer picture of the ring-down signal,

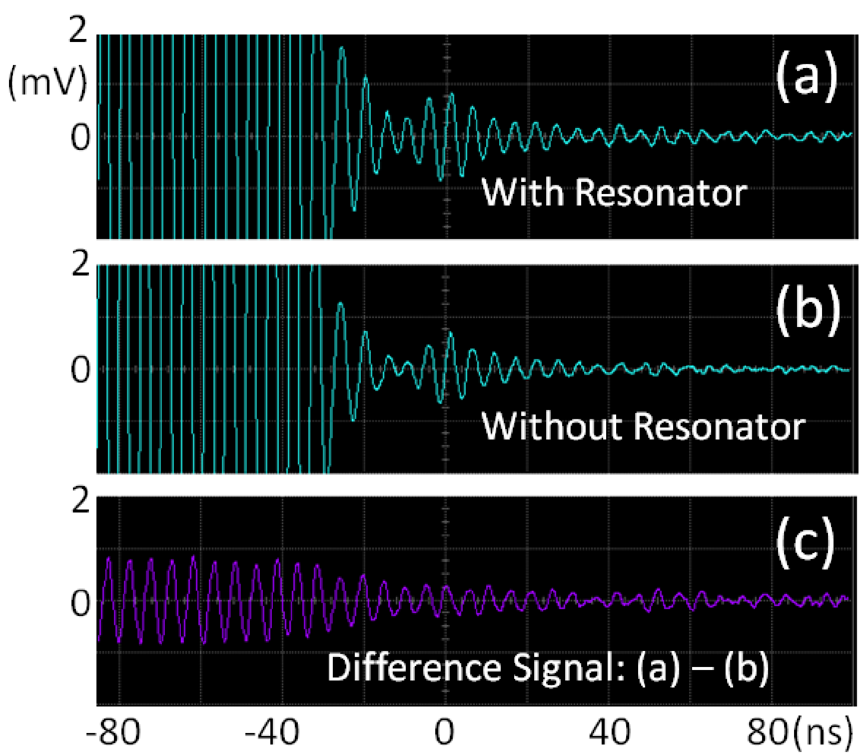

FIGURE 4.23: Observation of Ring-Down Signal Against Receive Antenna Transient
Receive antenna signal (a) with and (b) without ring-down signal, and the (c) difference of these two signals.

although jitter of the trigger signal sent to the oscilloscope results in a slight time shift of the two signals that must be accounted for in computing their difference. Using this subtraction scheme, the maximum antenna-device distance (in air) at which the planar device ring-down signal could be observed was 2 cm (amplitude 0.25 mV). This ring-down amplitude is significantly larger than the oscilloscope noise floor, because the transient signal in the receive antenna after excitation is the factor limiting sensing range, not oscilloscope noise. In fact, assuming the amplitude of the ring-down signal decreases with the cube of the antenna-device distance (Section 4.1.3), one expects the antenna-device distance could be increased to ~4 cm before scope noise would limit observation of the ring-down signal. Therefore, to increase sensing range beyond 2 cm, receive antenna transients must be reduced, either by improved off-switching of the excitation signal or antenna re-design. Note that adding an LNA to the receive chain is not a solution, since it will amplify antenna transients together with ring-down signals.

4.2.3 Singe Loop Tests

Although two loop ring-down experiments achieved better sensing range than impedance phase method experiments, the two loop antenna experimental setup suffered from a few drawbacks: the presence of transient signals in the receive antenna, no means of automating data taking, and the requirement that two antennae be coupled to the device under test, so that the effects of antenna mutual inductance should be accounted for in analyzing ring-down behavior. In contrast, by using a single antenna, data taking and result interpretation are simplified, and the size of the reader is reduced. Antenna transient behavior is not necessarily improved, but may be studied in this simplified setting.

In a single antenna reader, an RF burst at the resonant frequency of a tank is transmitted by the antenna before quickly shutting off transmission and switching to receive mode to record

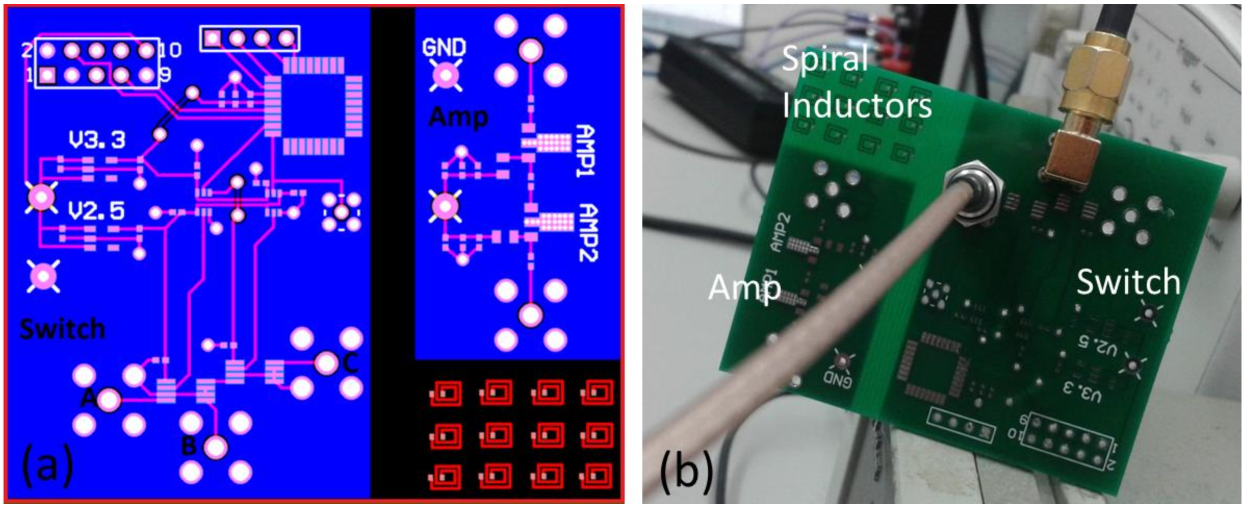

FIGURE 4.24: PCB for Single Antenna Testing
(a) PCB schematic and (b) channel isolation test.

the ring-down signal. Fig. 4.24(a) shows a PCB designed (Appendix 2) to perform this function. The 'Switch' section of the PCB is used to shut off transmission and turn on reception of the antenna. A, B, and C label SMA connectors used for connecting the: A – loop antenna, B – oscilloscope (receive channel), and C – function generator (transmit channel). Between the SMA connectors are two RF switch ICs used for switching the antenna between transmit and receive states. A Silicon Labs C8051F361 MCU in the top right corner of the 'Switch' PCB is used for sending control signals to the RF switches. Each switch changes state within 10 ns of a change to its control signal. The remaining right hand side of the PCB consists of a 40 dB RF amplifier ('Amp' section) and 12 spiral inductors for making planar LC tanks.

Because unwanted signals in the antenna during reception affect sensing range, it is important when using a single antenna design to achieve good transmit/receive channel isolation when the switches are turned off. Even without any ICs soldered to the board, this isolation is not perfect. Fig. 4.24(b) shows the setup used for testing the TX/RX isolation of the PCB board. Using the spectrum analyzer, the channel isolation levels were measured, and the results are

TABLE 4.9: **Unpopulated PCB Transmit/Receive Channel Isolation**

Frequency (GHz)	RX / TX Channel Isolation (dB)
1	> 90
2	80
3	60

shown in Table 4.9. Next, the PCB board was cut into 'Switch', 'Amp', and spiral inductor sections, and components were soldered in place. Fig. 4.25 shows a populated 'Switch' PCB with all test connections in place. The ribbon connector at the bottom of the image is used for programming/debugging the C8051F361 Silicon Labs MCU that issues control signals. The MCU was programmed to run at a clock speed of 100 MHz, so that switch states could be controlled independently within 20 ns of each other (2 MCU clock cycles). After populating the PCB and programming the MCU, isolation between transmit and receive channels was tested again in 2 states: (1) both switches on (TX on, RX off) and (2) both switches off (TX off, RX on). The results are shown in Table 4.10.

The ring-down behavior of a dummy LC tank coupled to a 1 cm diameter loop antenna is

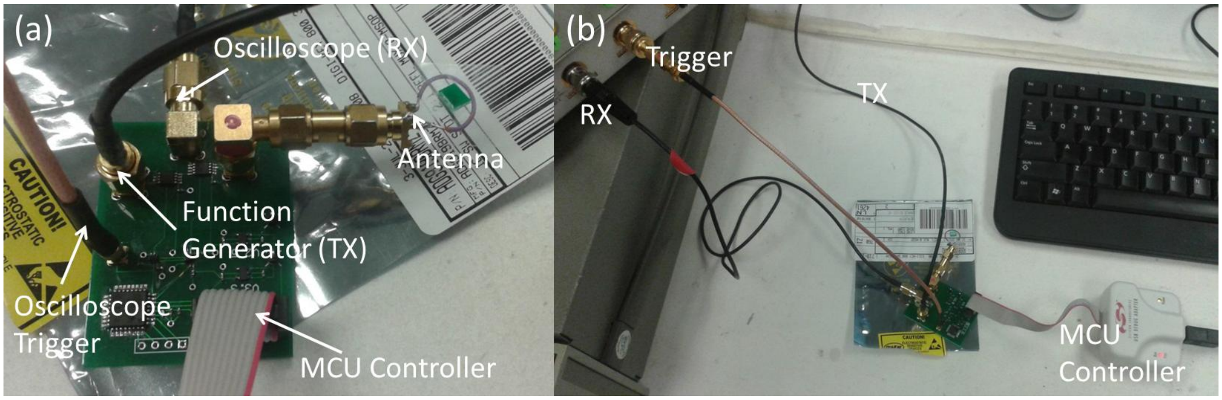

FIGURE 4.25: Single Antenna Test Experimental Setup
(a) Populated PCB and (b) test connections.

TABLE 4.10: **Populated PCB Transmit/Receive Channel Isolation**

Frequency (MHz)	RX / TX Channel Isolation (dB) – Switches On	RX / TX Channel Isolation (dB) – Switches Off
20	65	83
100	41	66.5
200	29	59.5
400	17	46
800	6	16

shown in Fig. 4.26(a). This tank had the same 68 pF surface mount capacitor as the tank shown in Fig. 4.13(b), but a slightly different resonant frequency of 189.8 MHz. The transmit power used in this experiment was 4 dBm, reduced from 20 dBm used in previous experiments because of power handling limitations of PCB components. This source power accounts for the 4 - 29 = -25 dBm (35 mV p2p) signal leaking into the RX channel (scope) prior to switching, in agreement with measured channel isolation characteristics. When a graft device was placed on top of the same antenna in an optimal orientation (antenna-device distance = 0 cm), a ring-down signal of

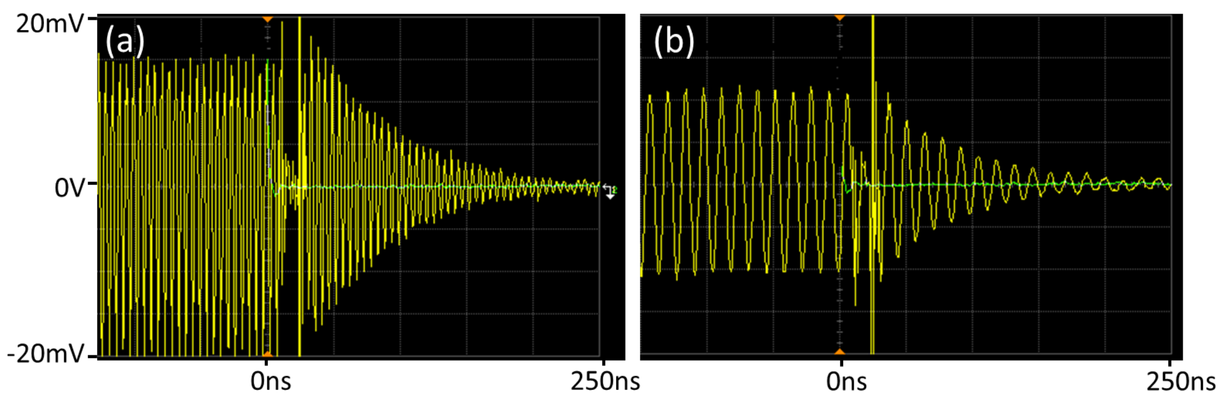

FIGURE 4.26: Single Antenna Test Ring-Down Signals
Resonant decay signals from a (a) planar LC tank and (b) graft device placed at 0 cm from a 1 cm diameter loop antenna.

smaller amplitude was observed than for the dummy tank (Fig. 4.26(b)). Once again, this shows that despite the size of the graft device, its ring-down signal amplitude is comparable to that derived from a device a few square millimeters in area for the experimental setup used, in agreement with the range test results of Sections 4.1.4 and 4.2.2. Sensing range with this setup is limited to <1 cm because of the low excitation power and poor channel isolation achieved with the selected RF switches.

Without redesigning the Switch PCB design, it is possible to enhance transmit/receive channel isolation and achieve a more precise means of quantifying the ring-down signal amplitude for different excitation frequencies by using down-conversion. By IQ demodulating and digitally sampling the ring-down signal, its amplitude may be inferred from measurement of I and Q output amplitudes, and signals leaked to the receive antenna due to poor channel isolation may be removed with a DC block.

To test the effect of down-conversion on the ring-down signal, a modified single antenna test setup (Fig. 4.24(a)) was used, with the Switch PCB receive channel fed into the RF port of a ZAD-1+ Mini-Circuits mixer, and the mixer LO port fed by the same signal as the PCB transmit channel using a power splitter. The IF output of the mixer was fed to the oscilloscope to capture the down-converted ring-down signal, and the results with and without coupling to a resonating planar LC tank are shown in Fig. 4.27(b) and (c). As evident from the images, the oscillating ring-down signal is replaced by an exponential decay after down-conversion, and the strength of the resonance can be determined by sampling the size of this decaying signal at a fixed time after transmission is cut off. At approximately 60 ns after cutting transmission, the resonant decay signal from a planar device located adjacent to the antenna was observed to have an amplitude of 4 mV. By low pass filtering the received signal (30 MHz cutoff), the planar device

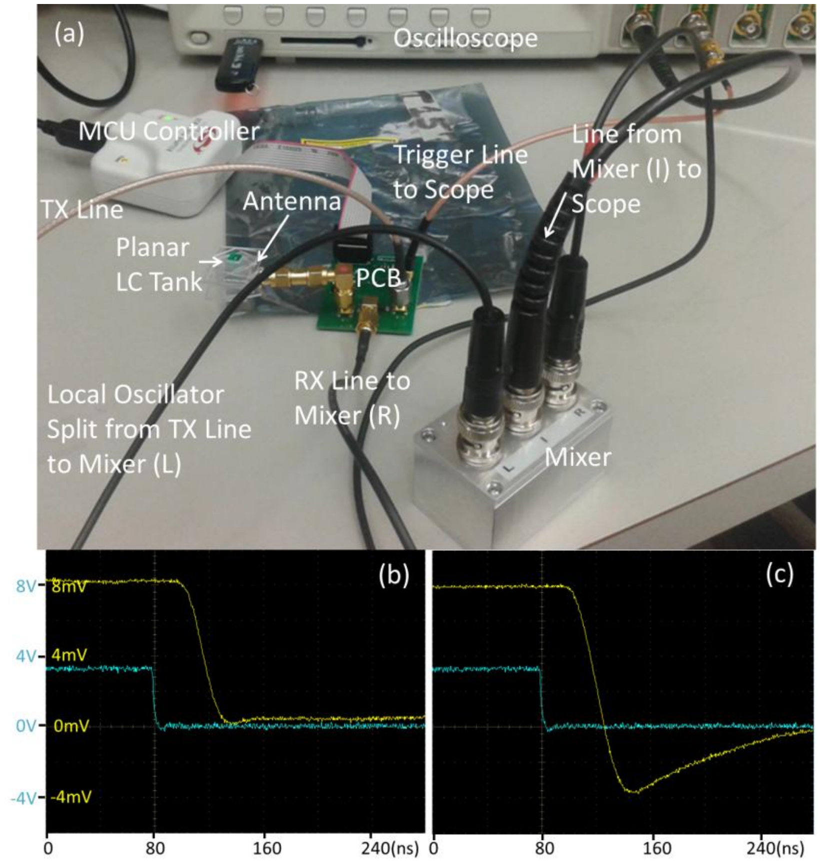

FIGURE 4.27: Single Antenna Test with Demodulation
(a) Test setup showing PCB and mixer. Demodulated ring-down signals are shown in (b) with no tank present and (c) with a planar LC tank coupled to the antenna.

resonance could be observed at 1cm antenna-device distance. Beyond this distance, the maximum decay signal could not be clearly observed above the low frequency variations of the scope noise floor (100 µV swings in DC offset), although the AC noise floor was lower (V_{rms} = 0.05 mV). By averaging over 100 samples, variations in the noise floor were reduced, and a resonant signal could be detected on the scope at 1.75 cm antenna-device distance. Making 100 ring-down measurements at 20 different excitation frequencies took ~10 ms, enabling the same 100 Hz device resonant frequency sampling rate achieved by the impedance phase method used in Section 4.1.4. At this sampling rate, the ring-down method sensing range was better than twice that of the impedance phase method.

To extend range further, work is needed to re-design the PCB switch to handle 20 dBm excitation powers, improve transmit/receive isolation, and understand the effect of antenna transients on the demodulated signal noise floor. Low noise amplification of the decay signal may also extend range if antenna transients can be reduced. Other improvements to the experimental setup could be made by incorporating an analog to digital converter into the receive chain to sample the demodulated ring-down signal and feed the results back to the MCU. This would help automate the data taking process, and the PCB design could then be extended to create a fully portable electronic reader with addition of an MCU controlled direct digital synthesizer.

4.2.4 Discussion

Initial two loop tests of the ring-down method showed a mock artery device resonant ring-down signal could be observed at an antenna-device distance of 2.75 cm (in air). A source power of 20 dBm was used in this test. This read range is an improvement over the 1.5 cm mock artery device read range (in air) achieved by the impedance phase method (Section 4.1.4). Further tests of the planar LC tank and graft devices showed functional sensing at 1.25 cm antenna-device distance, which was increased to 2 cm for the planar device by filtering its ring-down signal and subtracting the background antenna transient to make the oscillations observable. Immersion of a Parylene coated planar device in 7 mS/cm saline only slightly decreased its resonant frequency and ring-down signal amplitude, and the device resonance could still be detected at 1.25 cm antenna-device distance without application of any transient subtraction technique (made difficult by the experimental setup). Further enhancement of sensing range requires redesign of transmit excitation switching electronics and/or antennae to reduce transients. Improvement may also be achieved by redesigning resonators to alter their resonant frequencies once the optimal resonant frequency for maximizing sensing range of a device probed in blood is determined. If significant advances can be made in these areas, it is possible that sensing range may be extended to >5 cm with incorporation of an LNA in the receive chain, since noise is not currently the limiting factor.

To investigate switching electronics and remove the awkwardness of using two loops for real time monitoring, attention has been focused on development of a single loop, ring-down reader. A custom designed PCB was built to conduct single loop tests of the ring-down method. In these tests, only the planar LC tank resonator and graft device were considered, since the mock artery device did not appear practical for *in vivo* usage due to its very long bridging wire that could easily tangle on vessel walls during deployment. Testing revealed ring-down signals of similar amplitude are derived from both devices (in air), despite the much smaller size of the planar LC tank resonator. In fact, the ring-down signal from the planar device was found to be slightly larger, and could be observed at an antenna-device distance of 1.75 cm with demodulation, filtering (30 MHz low pass), and averaging (100 samples).

The single loop sensing distance is less than the two loop sensing (2 cm in air) distance because of the lower source power (4 dBm) that had to be used in the single loop test to avoid damaging PCB components. However, the results are promising in that if the PCB switch can be redesigned to allow 20 dBm source power, the current 1.75 cm sensing range may well be extended to ~2.5 cm to enable carotid artery monitoring. Furthermore, if a MEMS LC tank sensing approach is taken, this range need not be severely affected by immersion of the resonant device in a conductive medium such as blood (Section 4.2.2). Efforts to increase single loop ring-down read range must also be directed towards achieving better PCB TX/RX channel isolation and antenna redesign to reduce unwanted transient signals.

Chapter 5: Surface Micromachined Pressure Sensor

The stainless steel based pressure sensors described in Chapter 2 were designed specifically for integration with a stent to form a wireless pressure monitor. The primary advantage of these sensors is their low series resistance, which increases the quality factor of the integrated stent-sensor resonator, thereby increasing the wireless sensing range of the device. However, these sensors have drawbacks, such as significant variation in sensor performance and low fabrication throughput due to non-standard techniques employed in their fabrication. Also, since the sensors were designed and fabricated with a proof-of-principle approach, no careful consideration was given to demands on their performance required for their use in a restenosis monitor. Thus, the purpose in designing a surface micromachined pressure sensor was to use standard microfabrication techniques to improve reliability and create a sensor with specifications suitable for the targeted application. Since there are only a few examples of surface micromachined MEMS capacitive pressure sensors with metallic membranes found in the literature [25,70-72], and none are designed for in-stent pressure sensing, the design and development of such a sensor constitutes a new area of research.

5.1 Specifications

Results of Chapter 4's range tests suggest that within read range, LC tank resonant frequencies can be determined with a resolution of 0.5 MHz (Tables 4.6 - 4.8). Since LC tank resonant frequencies satisfy $f_R = \frac{1}{2\pi\sqrt{LC}}$, it follows that:

$$\frac{\Delta f_R}{f_R} = \frac{\Delta C}{2C} \quad (3)$$

Assuming $f_R = 50\ MHz$, this means that for each 1mmHg change in pressure, the fractional change in sensor capacitance must be 2% (20000 ppm) to ensure resonant frequencies are clearly resolved. This sensitivity is revealed to be quite high by survey of capacitive pressure sensors found in the literature. For example, the characteristics of 5 such capacitive sensors are shown in Table 5.1.

The largest sensitivity in Table 5.1 is that of an anodic bonded silicon pressure sensor ($0.8\% =$

TABLE 5.1: **Survey of Capacitive Pressure Sensor Sensitivity**

Ref.	$\frac{\Delta C}{C \cdot mmHg}$	Gauge Pressure Range (mmHg)	Sensor Lateral Dimensions (mm)	Fabrication Method (Substrate)
Ch. 2	300 ppm	0 – 200*	1.5×1.5	Polyimide bonding (Steel)
[23]	3500 ppm	0 – 50*	0.68×0.68	Anodic Bonding (Silicon)
[41]	500 ppm	0 – 200*	0.37×0.69	Surface Micro-machining (Glass)
[73]	8000 ppm	-110 – 0*	$circle\ radius = 0.5$	Anodic Bonding (Silicon)
[57]	500 ppm	0 – 100*	$circle\ radius = 0.5$	Surface Micro-machining (Silicon)

*Tested range. Operational range may be larger.

8000ppm), and this sensitivity is still less than the targeted figure of 2%. Therefore, to reduce demands on sensor performance, it is helpful to operate at a frequency higher than 50 MHz and improve reader signal processing. Assuming reader improvements can be made to achieve a frequency resolution of 0.1 MHz and operation at 200 MHz, the fractional change in capacitance required to resolve 1 mmHg pressure changes is reduced to 0.1% (1000 ppm). This sensitivity is achieved by the anodically bonded sensors in Table 5.1, but not by the surface micromachined sensors. However, since surface micromachining offers a more straight forward route to all-metal capacitive pressure sensor fabrication, a surface micromachining process was selected as the means of fabricating sensors for incorporation in high Q LC tanks. The modeling results of the next section suggest that the sensor sensitivity obtainable by using the process outlined in Section 5.3 is 400 ppm/mmHg. This is higher than the sensitivity of the sensors developed in Chapter 2, and good enough to achieve 2.5 mmHg pressure sensing resolution of LC tank systems in which the sensor is integrated.

5.2 Modeling

Prior to fabrication, modeling in COMSOL multiphysics was conducted to determine an appropriate sensor design to achieve the desired performance specifications. Fig. 5.1 shows an example of a sensor model, where a 1.0 μm thick, 260 μm diameter Cu membrane is deflected into contact with a dielectric coated metallic substrate by an applied pressure. The distance between the membrane and substrate (sensor cavity height) before deflection is 600 nm. These sensor dimensions do not optimize sensor sensitivity, but are representative of sensor dimensions used in the first fabrication process

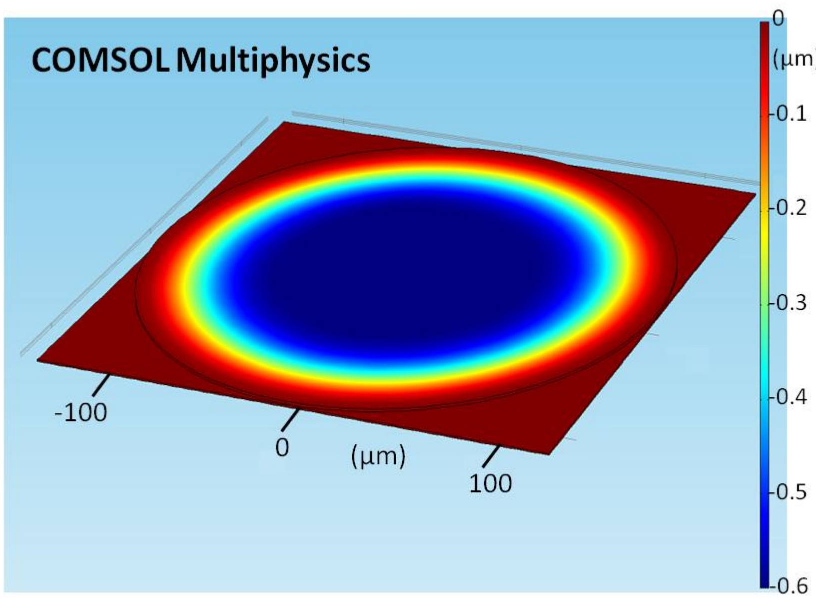

FIGURE 5.1: COMSOL Sensor Model
Deflection of aCu membrane (1.0 μm thick, 260 μm diameter) under 900 mmHg applied pressure (absolute). The internal pressure of the cavity is taken to be 0 mmHg absolute since the cavity is sealed in vacuum.

(Section 5.3.1) yielding functional pressure sensors. This fabrication process differs from the originally conceived fabrication process for which sensor photomasks were designed because of unanticipated problems encountered using this process (Section 5.3.2).

The absolute pressure applied to the top membrane surface is in the range of 760 - 900 mmHg (1 atm = 760 mmHg), and the absolute pressure applied to the bottom membrane surface is assumed to be 0, since the sensor cavity is sealed in vacuum. The modeling results indicate a linear response of sensor capacitance with pressure when the membrane is in contact with the substrate. For a 200 nm thick silicon dioxide dielectric (SiO_2 $\epsilon_r = 3.9$), the sensor base capacitance and sensitivity (touch mode) are ~6 pF and 400 ppm/mmHg, while for a 100 nm hafnium oxide dielectric (HfO_2 $\epsilon_r = 25$), the sensor base capacitance and sensitivity are ~16 pF and 440 ppm/mmHg. Further effort in modeling and fabrication is needed to determine sensor dimensions that optimize sensitivity.

Note that the sensitivities computed above only take into consideration the sensor membrane, and will be reduced by any additional fixed capacitance contributed by electrical connections. This electrode capacitance of fabricated sensors significantly decreased their sensitivity (Section 5.4), but no similar effect is expected to degrade the sensitivity of the MEMS LC tank proposed in Section 5.5. The simulated sensitivities achievable by sensors operating in touch mode (substrate contact) are expected to be adequate for the targeted restenosis monitoring application, although higher sensitivity available with non-touch mode operation may be achieved by fabricating arrays of membranes with smaller diameters to replace larger single membrane sensors with the same base capacitance. By designing membranes with a smaller diameter appropriately, atmospheric pressure will force them into near contact with the substrate, the regime in which their sensitivity is maximized.

5.3 Fabrication

5.3.1 Process

A process developed for surface micro-micromachining capacitive pressure sensors is illustrated in Fig. 5.2. The process begins with dry oxidation of a 300 µm thick p++ silicon wafer (1) in a tube furnace at 1050ºC for 9 hours. This produces a high quality 200 nm thick oxide layer on the silicon surface. Next, S1805 (produced from S1813 by diluting with thinner type P in 5:3 volume ratio) is spin coated at 3000 rpm on the wafer surface to form a 500 nm thick layer which is lithographically patterned to act as a sacrificial layer (2). Then, 1 µm of copper is e-beam deposited on the oxidized wafer and photoresist (3), before spin coating and patterning another S1805 layer on top of the copper (4). This S1805 layer acts as a mask to define different sensor shapes while the exposed copper is wet etched (5) for two minutes in ammonium persulfate (APS). Wet etching exposes the original sacrificial photoresist layer, which is released by immersing the wafer in acetone for ~1 hour (6). Once released, silicon substrates containing sensors are soaked in isopropyl alcohol (IPA) and transferred to an autosamdri-815 supercritical CO2 dryer for drying. After drying, sensor cavities are sealed with an Optomec Aerosol Jet printer (7), by printing HD-3007 over their openings while the substrate is heated to 70 ºC. Finally, sensors are wire bonded to make electrical connections for testing, and coated with a final 1 µm thick layer of Parylene C to ensure hermetic sealing of the cavities (8).

An optical micrograph of a finished sensor and photo of a silicon substrate containing an array of sensors is shown in Fig. 5.3. The discoloration of the sensor surface is due to oxidation of the copper

Step	Description	Schematic
1	Begin with a p++ silicon substrate with 200 nm thermal oxide	

Step	Description	Schematic
2	Spincoat and pattern 500 nm thick layer of S1805 photoresist	
3	E-beam deposit 1 µm of copper	
4	Spincoat mask layer of S1805 photoresist and lithographically pattern	
5	Pattern photoresist and wet etch underlying copper layer	
6	Release photoresist with acetone and dry with supercritical CO2 dryer	
7	Seal cavity opening by depositing polyimide with Optomec Aerosol Jet printer	
8	Wire bond in preparation for testing, and coat with 1um of Parylene to ensure hermetic sealing	

FIGURE 5.2: Surface Micromachined Pressure Sensor Fabrication Process

surface and poor adhesion of Parylene-C. The polyimide deposited with the aerosol jet printer clearly covers the right edge of the sensor where the cavity opening is. In the sensor array, the membranes of

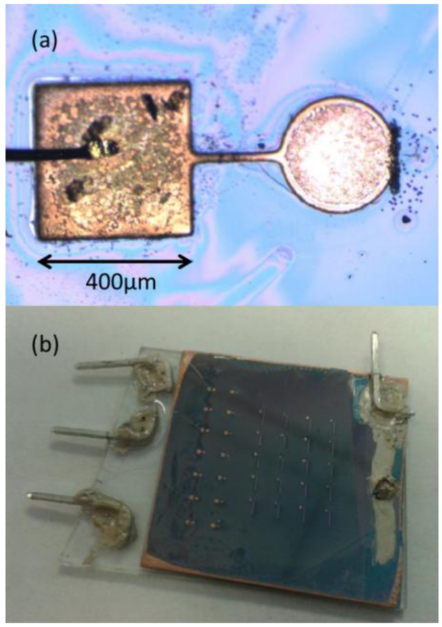

FIGURE 5.3: Surface Micromachined Capacitive Pressure Sensor
(a) Optical micrograph of a fabricated sensor and (b) a photo of a sensor array ready for testing

three sensors have been wire bonded to test leads silver pasted to a separate glass substrate, while a fourth lead is silver pasted directly to the p-doped silicon substrate which acts as the bottom electrode of each sensor. The sensor array shown is the most recently fabricated, and the first shown to contain functional sensors. Only three sensors were tested due to space limitations of making test connections, although the substrate itself contains 44 sensors. Hundreds of sensors could be contained on a silicon substrate of the same size by redesigning the photomasks used for fabrication.

5.3.2 Discussion

The developed fabrication process was arrived at after trying several others. It is instructive to discuss what went wrong with these other attempts, to illustrate common problems encountered in MEMS fabrication.

Fig. 5.4 shows the result of a fabrication process in which plasma enhanced chemical vapor deposition (PECVD: 100 kHz Trion) deposited SiO_2 was used as the primary membrane material. In the images, the SiO_2 membrane either (a) buckled or (b) broke after sacrificial layer

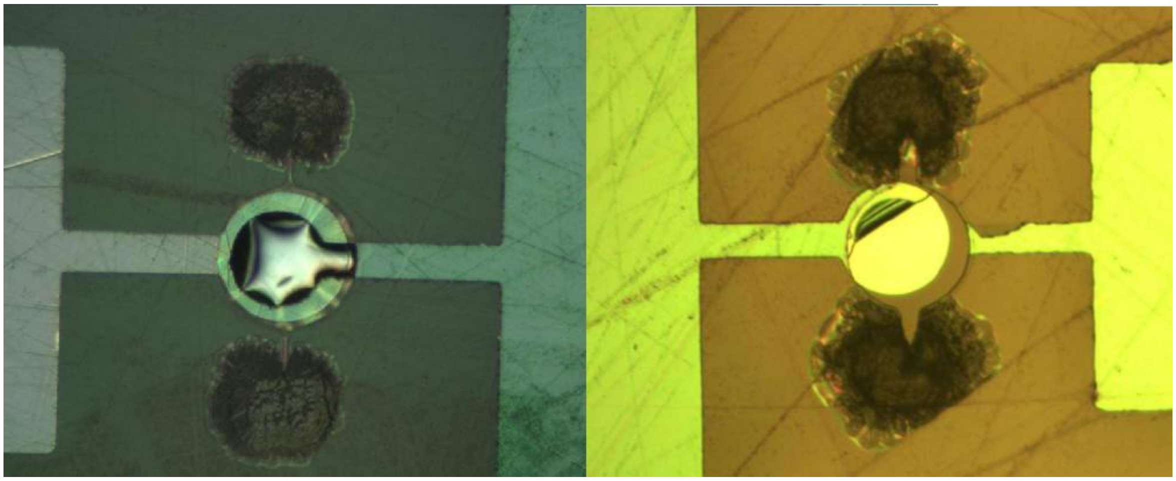

FIGURE 5.4: Effect of Large Compressive Stress on Membranes
SiO_2 membranes under compressive stress (a) buckled and (b) broke after releasing.

release because of residual compressive stress from the deposition process. This compressive stress is characteristic of thin films deposited with 100 kHz PECVD systems [74], and although it can be avoided by using a dual source or ECR type system, access to such a system was not readily available. It was also found that buckled SiO_2 membranes tended to break the metal connection from the top capacitive plate to the test electrode, rendering sensors completely un-testable. To circumvent these problems, a relatively thick e-beam deposited layer of copper was used to form sensor membranes, since it did not fracture and held the membranes under tensile stress to keep them flat.

Another fabrication issue encountered was how to hermetically seal the sensors. The first attempts at sealing cavity openings were made with the Optomec by printing silver ink. However, it was found that this ink seeped into sensor cavities before drying, and while drying would draw the membrane and substrate into contact (Fig. 5.5(a)). Fig. 5.5(b) shows an optical micrograph of two sensors fabricated on a glass substrate in which the seeping of silver ink into their cavities is clear. To solve this problem, a different sealing material and set of aerosol jet parameters had to be used. HD-3007 polyimide was chosen as a new sealing material because of

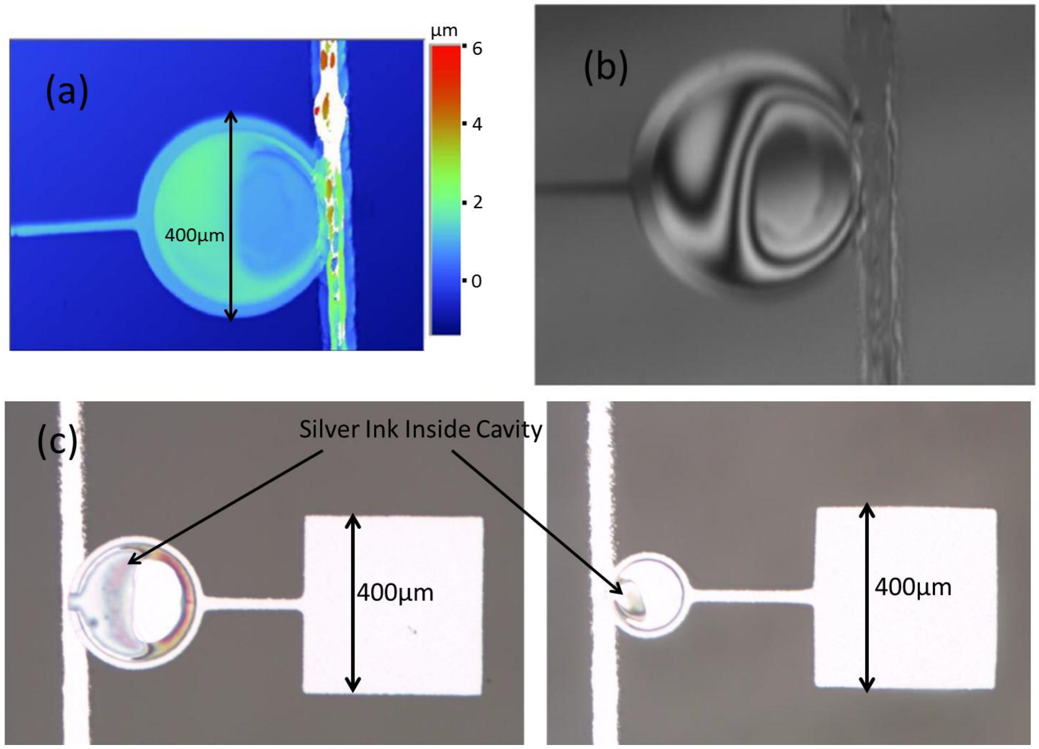

FIGURE 5.5: Membrane Deformation caused by Silver Ink Printing
(a) Optical profiles of sensors sealed with silver ink showed large regions of membrane-substrate contact.
(b) Silver ink was directly observed to seep in to the cavities of sensors fabricated on glass slides.

its high viscosity and adhesion. With a slight dilution from 25% to 23% solid content in N-methyl-2-pyrrolidine, its viscosity could be reduced just below 1000 cpa for compatibility with use Optomec printing. Appropriate aerosol jet parameters were determined for printing the polyimide, and no more seepage into cavities was observed.

Despite the success in printing polyimide to seal the cavities, the sealing was not found to be hermetic, as sensor capacitance readings did not change with applied pressure. This is why a final layer of Parylene was coated over sensors to improve sealing. More robust hermetic sealing layers such as atomic layer deposition (ALD) deposited aluminum oxide may be used instead of Parylene to guarantee better long term performance. Also, it is possible that aerosol jet printing of polyimide may be replaced with PECVD deposition of SiO_2 for faster processing.

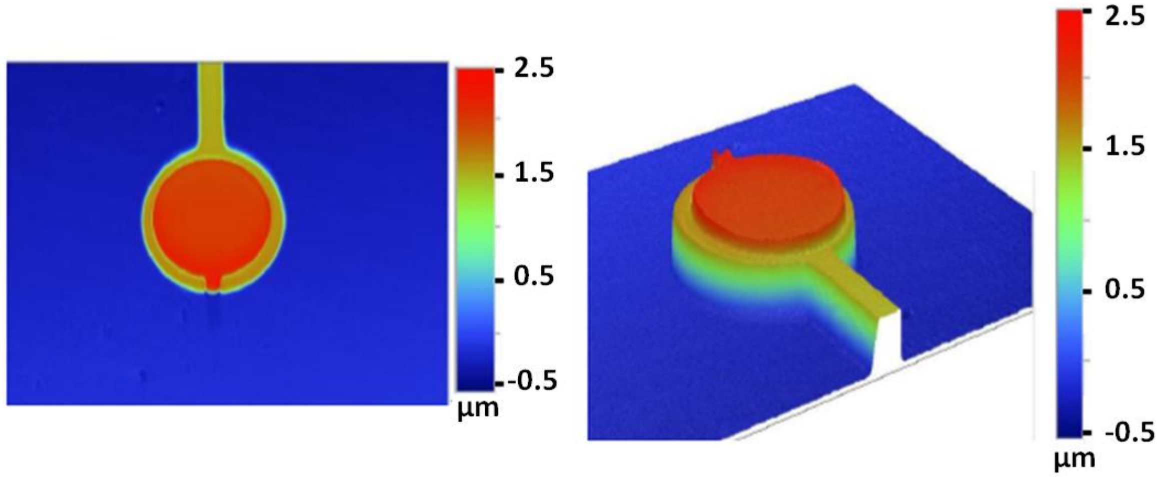

FIGURE 5.6: Optical Profile of a Pressure Sensor Before Sealing

5.4 Characterization

Before sealing, suspension of sensor membranes has been verified by optical profiling (Fig 5.6). At this stage of the fabrication process, diaphragms showed good flatness, and cavity depths of 500 - 600 nm.

Optical and contact profiles of a sensor after final Parylene coating are shown in Fig. 5.7(a) and (b). The contact profile clearly shows a depression of the cavity membrane at its center due to the pressure differential between the cavity interior and exterior after Parylene coating. The depression appears to be ~1 µm lower than the cavity edge, which is larger than

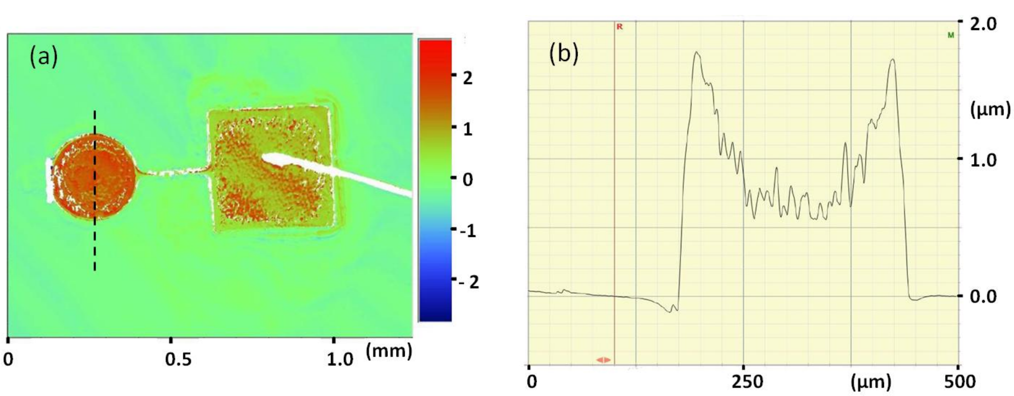

FIGURE 5.7: Optical and Contacts Profile of a Fabricated Sensor
(a) Optical and (b) contact profiles of a fabricated sensor.

the initial cavity depth. This is due to protrusion of the edges of the membrane that occur during copper and Parylene thin film depositions.

The response to applied pressure of three sensors (A,B, and C) were tested in a custom pressure chamber. Sensor capacitances were measured while pressure was applied manually and monitored with a reference pressure sensor. The change in capacitance of each sensor for an applied pressure of 240 mmHg is shown in Table 5.2. Prior to sealing, the capacitance of

TABLE 5.2: Surface Micromachined Pressure Sensor Response

Sensor	Capacitance (1 atm + 0 mmHg)	Capacitance (1 atm + 240 mmHg)
A	29.96 pF	30.03 pF
B	29.27 pF	29.36 pF
C	30.42 pF	30.45 pF

each sensor was measured to be ≈23 pF, suggesting the depression of the membrane during sealing added an additional ≈7 pF of capacitance to each sensor. Since each sensor consists of a 400 µm x 400 µm bonding square, 200 µm x 20 µm stem, and a 300 µm diameter diaphragm with a 20 µm wide boundary contacting the substrate, the ratio of area in contact with the substrate to the suspended diaphragm is:

$$\left(400^2 + 200 \times 20 + \pi(150^2 - 130^2)\right) : \pi\,(130^2) = 3.4 \quad (4)$$

Therefore, knowing the final capacitance each sensor is ≈30 pF, the contribution to capacitance from a completely depressed diaphragm must have been $\frac{30}{3.4+1} = 6.8$ pF, which is in approximate agreement with the experimental findings.

The sensitivities (in units $\frac{\Delta C}{C \cdot mmHg}$) of sensors A, B, and C are 10 ppm, 13 ppm, and 4 ppm respectively, when evaluated with respect to the entire sensor capacitance. When evaluated with respect to the ~7 pF membrane capacitance alone (as done in modeling Section 5.2), the sensitivities are 40 ppm, 50 ppm, and 20 ppm respectively. These sensitivities are an order of magnitude smaller than expected from computer modeling (Section 5.2). This may be due to the use of Parylene as a hermetic seal, which because of its permeability allows sensor cavity pressures to rise, dramatically reducing sensitivity. It may also be due to tension residual in the sensor membranes from e-beam deposition. Use of atomic layer deposited alumina as a hermetic sealing agent [75] and electroplating as a means of creating sensor membranes are potential means of solving these problems.

5.5 A MEMS LC Tank Device

One of the advantages of the surface micromachining fabrication approach is that it enables simple integration of capacitive pressure sensors with micro-inductors to construct MEMS LC tanks. Such devices (Fig. 1.2), used for wireless pressure sensing, are familiar from the literature and predate systems using stents as tank inductors. Since the use of helical stents posed practical difficulties during *in vitro* testing of stent based LC tanks (Chapter 3), and range testing showed no great advantage to using them over planar LC tanks, it is possible that integrating two independent MEMS LC tanks on either end of a typical commercial stent could be a better solution to wireless in-stent pressure monitoring. By taking this approach, troublesome mechanical and device variability issues associated with using helical stents are avoided. The MEMS LC tank fabrication process proposed in this section has not been followed through to completion, but is briefly described to give some idea of the efforts exerted in this direction.

5.5.1 Microinductor Fabrication

MEMS LC tanks require micro-inductors, so a process for fabricating such inductors is illustrated in Fig. 5.8 below. It begins by e-beam depositing a Ti 10 nm / Cu 100 nm seed layer for electroplating on a 200 µm thick glass slide. Next, the glass slide is rinsed in acetone and DI water for 5 minutes, before being blown dry with nitrogen and left on a hotplate at 175 ºC for 15 minutes to ensure complete moisture removal. A thick epoxy based photoresist suitable for forming electroplating molds (KMPR 1050, MicroChem, USA) is spun on the glass slide at 2000 rpm for 1 minute to form a 60 µm thick film, and then soft baked at 100 ºC for 20 minutes. Once baking is finished, the slide is left to cool for 5 minutes before 4 - 5 minutes of masked exposure. As required by KMPR processes, the exposed sample is baked for a further 4 minutes after exposure, before 5 minutes of cooling, and a 3 - 4 minute development in standard Microchem SU-8 developer. Rinsing developed samples with isopropyl alcohol (IPA) and drying with an air gun leaves a mold that can be used for electroplating copper inductors.

The electroplating bath consists of a sulfuric acid solution (70 g/L Copper Sulfate, 200 g/L Sulfuric Acid, 50 mg/L Chloride, 10 mL/L Cuprostar Make-Up, 5 mL/L Cuprostar Brightener). During electroplating, a piece of copper foil is used as an anode. Applying a voltage of 1 V between the anode and sample (cathode) for 20 - 30 minutes produces good quality, 20 µm thick, inductors within the mold. By immersing the sample in MicroChem Remover PG at 80 ºC for an hour, most of the KMPR is released, and any remaining material can be removed by a brief dip in dilute Pirahna etchant which without noticeable effect on the copper. A brief ammonium persulfate (APS) wet etch is then used to remove the exposed copper seed layer.

To embed the micro-inductors in a flat substrate, a 5 µm thick layer of HD-3007 is spin-coated on top of them and baked at 150 ºC for two hours to strengthen their structure, before spin-coating on another 50 µm KMPR layer which is soft-baked for twenty minutes at 100 ºC.

After soft-baking, a second glass slide is placed on top of the KMPR and bonded under a 1 kg weight for three hours at 200 ºC to complete bonding. Finally, the sample is removed from the

Step	Description	Schematic
1	E-beam deposit a 100 nm Cu seed layer for electroplating.	
2	Spincoat and pattern KMPR photoresist to form electroplating mold.	
3	Electroplate 20 - 50 µm of copper.	
4	Immerse in Remover PG for one hour and etch in dilute Pirahna solution to remove KMPR. Remove seed layer with APS wet etch.	
5	Spincoat KMPR over inductors and thermally bond another glass slide on top. For extra surface stability, a coating of HD-3007 polyimide can be applied before KMPR	
6	Protecting the bonded glass side with tape, wet etch away the other glass side with HF, leaving a flat surface with the inductors exposed.	

FIGURE 5.8: Microinductor Fabrication Process

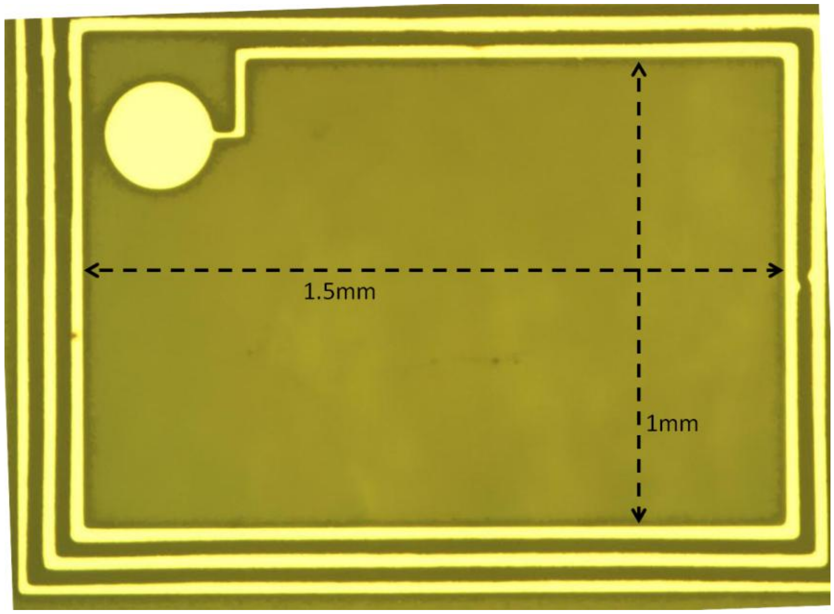

FIGURE 5.9: Fabricated Microinductor
Optical micrograph of a micro-inductor after fabrication step 5.

the other is protected with tape, to leave a rigid flat substrate with embedded micro-inductors. An image of a micro-inductor prior to HF release (after step 5) is shown in Fig. 5.9. Further work is needed to improve the last release step, which can damage the glass-KMPR adhesion without careful protection.

5.5.2 Proposed Tank Device

By coating a thin dielectric film on the micro-inductor substrates and surface micro-machining pressure sensors on top of this substrate, it is proposed that pressure sensitive LC tanks can be fabricated. The suggested alignment of the top sensor and bottom inductor is shown in Fig. 5.10. Notice that no direct electrical connection between the top sensor and bottom inductor is made, but an LC tank is still formed. This is because two capacitive connections between the top and bottom exist: one occurring at the sensor body, the other at the sensor membrane. The sensor body capacitance is designed to be much larger than the sensor membrane capacitance, so that it acts like a direct electrical connection at the tank resonant frequency. Explicitly, the sensor body

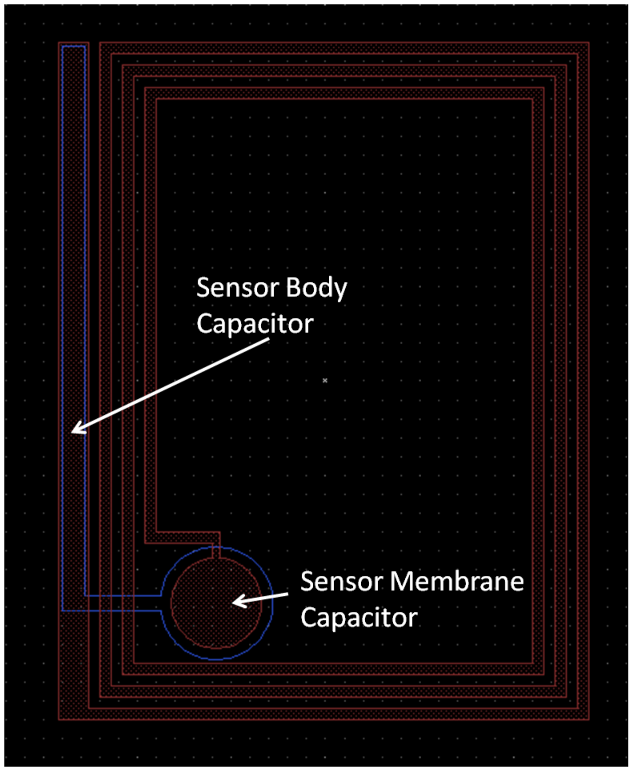

FIGURE 5.10: Sensor and Microinductor Alignment for LC Tank Formation
No direct electrical connections are made, but the tank circuit is completed by two capacitors.

has dimensions 60 µm X 1500 µm (area 90,000 µm^2), while the sensor membrane capacitance derives from a circle of diameter 240 µm (area 45239 µm^2), and is not in contact with the substrate over a significant portion of this area (Fig. 5.1). Denoting the sensor body and membrane capacitances by C_{SB} and C_{SM}, it follows that $C_{SB} > 2 \cdot C_{SM}$, so that the total series capacitance C_S of the two capacitors satisfies:

$$C_S = \frac{C_{SM}}{1+\frac{C_{SM}}{C_{SB}}} > \frac{2}{3} C_{SM} \quad (4)$$

This equation shows that the resonant frequency of the tank is only slightly increased by the absence of a direct electrical connection between the sensor body and inductor, and that the pressure sensitivity of the tank resonant frequency is not significantly altered.

The lateral dimensions of the tank are 1.5 mm X 1.8 mm, so that it can be mounted on platform extensions of a stent in a manner similar to the capacitive sensors in Chapter 3. For the intended pressure monitoring application, it has advantages over similar tank devices described in the literature in that it is purely metallic, and its micro-inductor can be made very thick (100 μm) to maximize quality factor. Theoretical calculations suggest the tank inductance is ≈25 nH [76], and by choosing a high-k dielectric for coating the embedded micro-inductor substrates (such as HfO_2), the tank membrane capacitance can be made as large as 16 pF (Section 5.2) to reduce the tank resonant frequency to around 250 MHz. Assuming a 100 μm thick inductor, the resistance of the LC tank is estimated to be 1 Ω (resistance of sensor connections on top of substrate), so that the quality factor $Q = \frac{1}{R}\sqrt{\frac{L}{C}} \approx 40$ obtained is higher than the quality factor of the planar LC tanks range tested in Chapter 4. Furthermore, the central area of the micro-fabricated spiral inductor is larger than that of the PCB spiral inductors utilized Chapter 4, and the number of turns is increased, suggesting that the proposed MEMS LC tank device should have similar, if not better, wireless performance than the planar LC tanks.

Chapter 6: A CMOS Based System for Blood Pressure Monitoring

6.1 Advantages of CMOS Based System Design

The primary challenge to using pressure sensitive LC tanks for in-stent restenosis monitoring is achieving a clinically relevant sensing range of at least 2.5 cm (for carotid artery monitoring) Despite efforts to optimize device performance and external reading schemes, no tank system has yet been produced with the desired range and resolution. The original design approach taken in this thesis used specially designed strutless stents to address this problem, but testing revealed that devices incorporating these stents suffer from several new mechanical/deployment issues (Chapter 3), and do not enable significantly longer wireless read ranges than planar LC tank devices a few square mm in size.

CMOS based in-stent monitoring systems offer a solution by operating at higher frequencies, which has been shown to be beneficial for powering implants efficiently [77]. Furthermore, their operation does not necessitate redesign of the stent or inclusion of an additional wire. Instead, a typical commercial stent is used as an antenna to wirelessly power a CMOS integrated circuit attached to it for reading and transmission of pressure data. The transmission and reception properties of such systems have been studied [78], and the results indicate that an RF transmitter (operating within FCC radiation exposure guidelines) placed within several centimeters of a stent antenna can provide a enough wireless power to drive a CMOS IC. Also, the power received by the IC is not as dependent on the stent's alignment with the transmitting antenna as it is in the case of LC tank systems, where there exist antenna-device orientations for which the geometric coupling is zero.

Another advantage of a CMOS based design approach is that it allows processing of pressure data into digital signals, so that measurement resolution of the reader is not sacrificed at device-reader distances where signal to noise ratio is low. For instance, frequency shift keying [16] and amplitude shift keying [79-80] techniques can be used to directly transmit digitized pressure readings from the implant. This is different from situations in which LC tanks are used as pressure monitors, where ability to resolve tank resonant frequency is significantly degraded by low signal to noise ratio, and worsens pressure reading resolution of the overall system beyond the limits imposed by the resolution of the pressure sensor itself.

Finally, CMOS based systems offer the advantage that data can be transmitted over a narrow frequency band chosen by the designer (e.g. ISM band [81]), whereas LC tanks necessarily operate over larger bandwidths sensitive to variation in sensor fabrication and stent expansion. Thus, it is easier to fix performance specifications for CMOS based devices and readers, and achieve immunity to environmental variation.

6.2 An ASIC for Wireless Pressure Monitoring

In designing a CMOS ASIC for in-stent pressure monitoring, there are many design choices to make, including what CMOS technology to use, how to integrate the chip with a pressure sensor, what type of pressure sensor to use, what bandwidth to use, and what wireless communication protocol to use. At present, there is no obvious answer for what design specifications are optimal, but with an eye towards devising a system with practical utility, the most important considerations appear to be ease of integration of the chip/sensor/stent, and ensuring adequate power harvesting of the device to turn on the CMOS chip when an RF transmitter is located >2.5 cm away.

By reviewing the literature on CMOS based in-stent pressure monitoring, difficulties inherent in ensuring both ease of integration and adequate power supply are apparent. One attempt [28] achieves ultralow power consumption by integrating a MEMS capacitive pressure sensor with an on-chip low power variable frequency oscillator (VFO). Thus, as in LC tank systems, the output signal of the VFO encodes the in-stent pressure reading in its frequency, and is transmitted outside the body by the stent antenna. This design approach has the advantage of simplicity, but also a couple drawbacks. Firstly, a differential RF input signal is required to power the CMOS IC, and to obtain such a signal, electrical connections must be made from both ends of the stent to the chip. This requires additional wiring, which may or may not be practical. Secondly, ultralow power consumption of the IC is only achieved through integration with a MEMs capacitive pressure sensor with very low series resistance, and widely available silicon based sensors do not have this characteristic.

Another approach [16] avoided additional wiring by integrating a CMOS chip and a commercial capacitive pressure sensor (microFab Bremen E1.3 N) in a liquid crystal polymer (LCP) based PCB package, which acted as a ground plane for the stent antenna. This device, because of its unusual antenna design, needed an RF transmitter operating right near the Federal Communications Commissiom (FCC) limits of radiation exposure to achieve power up. Also, the LCP packaging was quite bulky, causing potential difficulties in crimping and deployment, and the device sensor was not located at the end of the stent where it needs to be for FFR measurement.

To help investigate the aforementioned integration and sensing range issues, a CMOS IC design is presented in the following Sections 6.2.1 - 6.2.3. The design allows the stent and IC ground plane to act together as a monopole antenna, avoiding the use of any additional wires and streamlining its integration with a stent. This is advantageous from a mechanical point of view, although determination of whether or not such a configuration can harvest enough power to drive an IC at stent-transmitter distances > 2.5 cm is not clear at present, and requires experimentation with different stent antennae and matching networks [82] for better understanding. This is why a primary goal of the work in this chapter is to help determine if additional wiring is required for CMOS based in-stent restenosis monitoring.

To keep circuit design simple, an on-chip VCO is designed to interface directly with a MEMS capacitive pressure sensor, so that its output frequency is a measure of in-stent pressure. The power consumption problem caused by high sensor series resistance may be avoided by using an all-metal surface micromachined pressure similar to the sensor described in Chapter 5, but fabricated on a metallic substrate rather than doped silicon. In Section 6.3, electromagnetic modeling of a stent is used to illustrate the importance of impedance matching at the stent-IC interface for extending sensing range, and a method of integrating the sensor, IC, and stent using through glass vias (TGVs [83]) is proposed. The results of IC design and sensor-stent interface modeling clarify desirable features of a practical CMOS based in-stent pressure monitoring system, and challenges associated with taking a CMOS based design approach. Discussion of these issues is given at the end of this chapter (Section 6.4).

6.2.1 Design Overview

The schematic in Fig. 6.1 shows the cells in the ASIC design. A Rectifier takes an RF input from one end of the stent and converts it to a DC voltage for powering the bias generator and Colpitts oscillator. The oscillator's frequency is determined by the values of an on-chip spiral inductor and a MEMs capacitive pressure sensor, and one of its outputs is fed back to the stent for transmission. Both the capacitance of a capacitive pressure sensor and an on chip spiral inductor determine the oscillator output frequency.

6.2.2 Component Design and Simulation

In this section, the operation of each primary cell is explained with reference to its

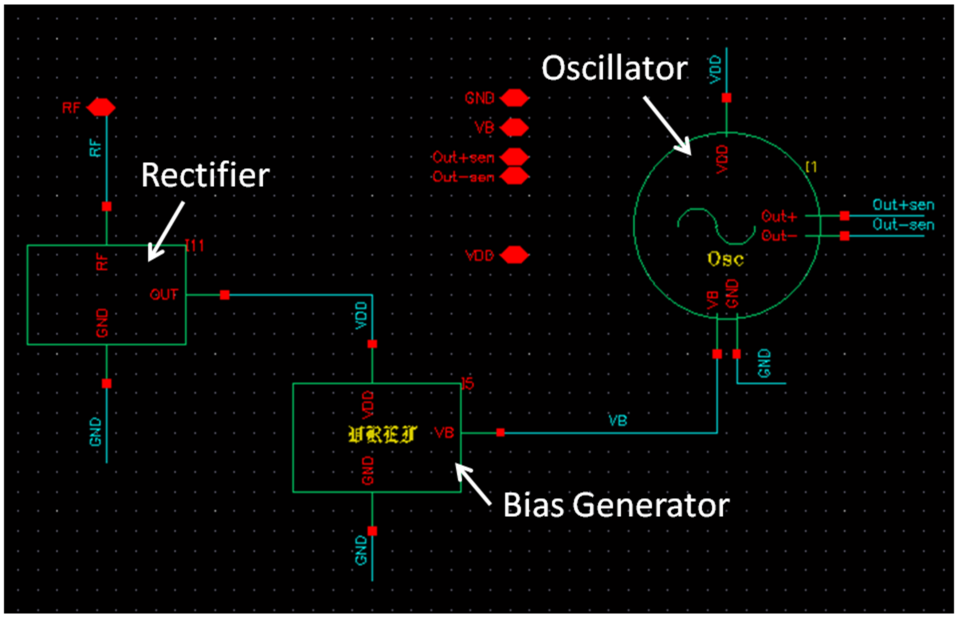

FIGURE 6.1: Top Level ASIC Design Schematic

schematic diagram. The results of simulating both the schematic and layout circuits of each cell are given. By understanding the working of each cell the overall system is understood.

6.2.2.1 Rectifier

The rectifier schematic shown in Fig. 6.2(a) consists of 3 identical stages. The purpose of having 3 stages is to increase the DC output of a single stage by a factor of 3. The schematic of an individual stage Fig. 6.2(b) shows two diode-connected metal-oxide-semiconductor field-effect transistors (MOSFETs) with input and output coupling capacitors in a Greinacher voltage doubler configuration [84]. In this configuration, the function of the diode at the input is to charge the input capacitor of the stage on negative voltage swings of the input signal. The effect of this is to raise the DC offset of the RF signal fed to the output diode and capacitor, which function as a standard half wave rectifier to produce the output DC voltage. The circuit is called a doubler because when the stage is not loaded the output DC voltage is approximately twice the amplitude of the RF input signal.

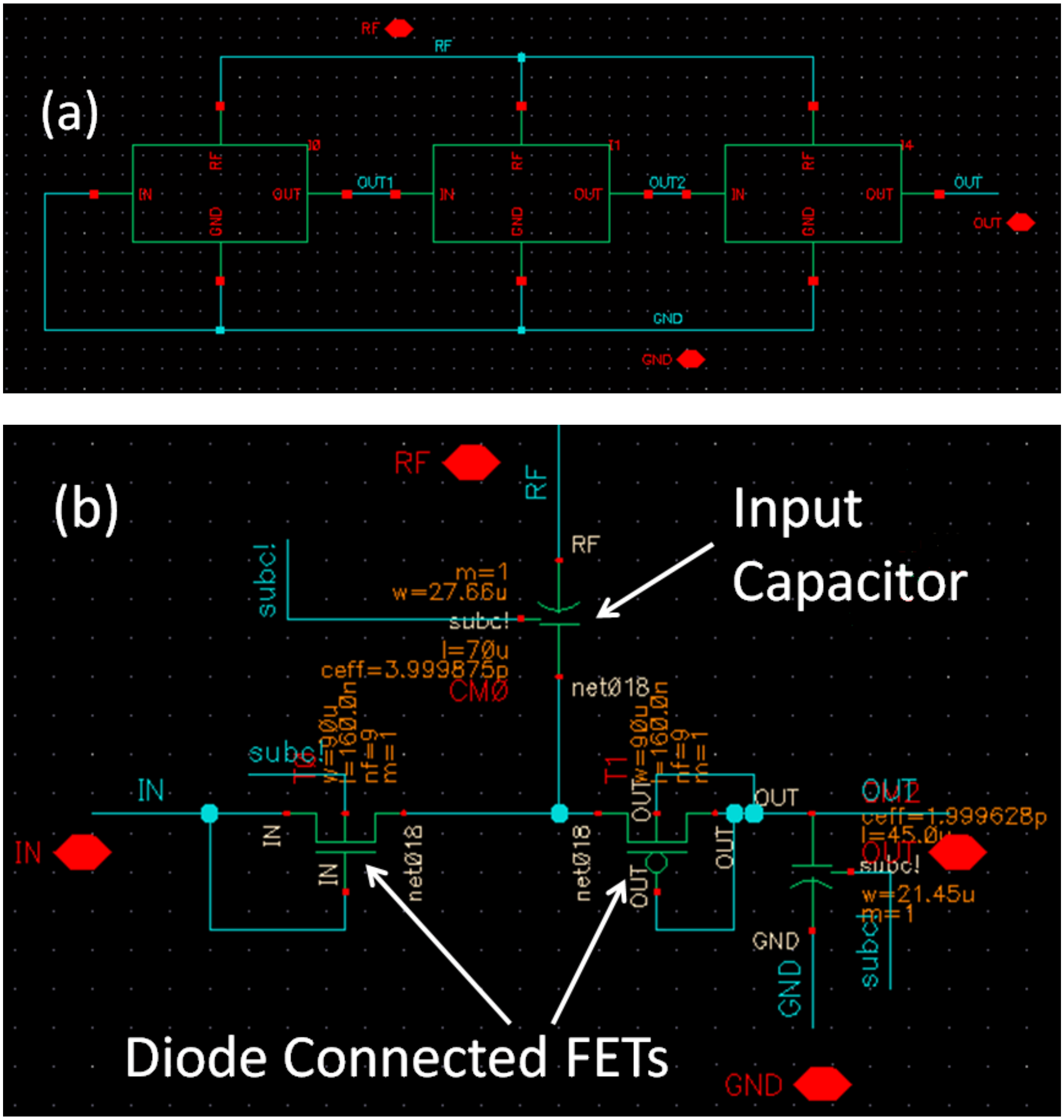

FIGURE 6.2: Rectifier Schematic
(a) Top level schematic of rectifier showing the connections of its 3 identical stages.
(b) Schematic of an individual rectifier stage, showing diode connected FETS in a Greinacher voltage doubler configuration.

The input signal amplitude to the rectifier must be greater than the turn on voltage of each diode in this configuration if the rectifier is to produce a useful output. Since each diode is a FET with gate and drain tied together, this is equivalent to the condition that the input signal amplitude must be at least as large as the threshold voltage of each diode connected transistor. That this is so is apparent from the standard MOSFET saturation current equation [85]:

$$I_{D,max} = \frac{1}{2}\mu_n C_{ox}\frac{W}{L}(V_{GS} - V_{TH})^2$$

which shows the maximum current load $I_{D,max}$ of a rectifier stage determines gate-source voltages V_{GS} slightly larger than the transistor threshold voltages V_{TH} that must be surpassed by input signals for proper rectifier function. Clearly, these gate-source voltages are minimized by maximizing the transistor dimension ratio $\frac{W}{L}$. This is why the transistors in the rectifier are chosen to be wide and short with dimensions W = 90 µm, L = 160 nm. These dimensions provide a reasonable trade-off between good circuit performance and small layout area, and support a current load of about 100 µA.

Simulation results of a single rectifier stage with a low current load (< 1 µA) are shown in Fig. 6.3. A 500 mV, 100 MHz RF signal applied to the stage input (purple) gives rise to a DC output of about 500 mV with a small ripple (white) after 250 ns. The yellow waveform is the DC shifted RF signal occurring between the input capacitor and diode-connected MOSFETs. Since the circuit is intended to operate at 1 GHz input, the stage`s output capacitance is set to 2 pF to reduce most of the rectifier output ripple at this frequency without overloading the stage and reducing the DC output level. The stage`s input capacitance is set to 4 pF, much larger than the parasitic capacitances of each transistor source/drain to ground, so that the input signal is not significantly divided during rectification and the largest possible DC output is obtained.

In the multistage rectifier, 3 stages are linked together to form a long voltage multiplier cascade (Villard cascade) which increases the DC output. The transient simulation results of the schematic and extracted rectifier circuits are compared in Fig. 6.4, for a 500 mV, 1 GHz RF

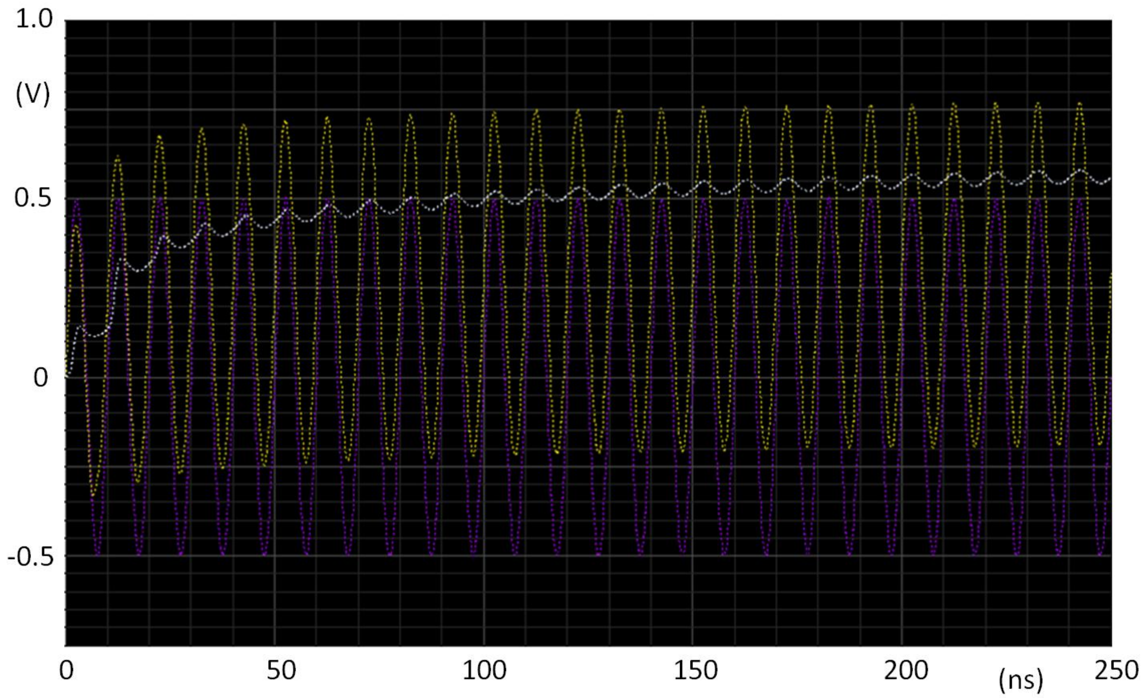

FIGURE 6.3: Single Stage Simulation
Simulation of a single rectifier stage for a 500 mV, 100 MHz RF input (purple). The DC shifted input signal and rectifier output waveforms are shown in yellow and white respectively.

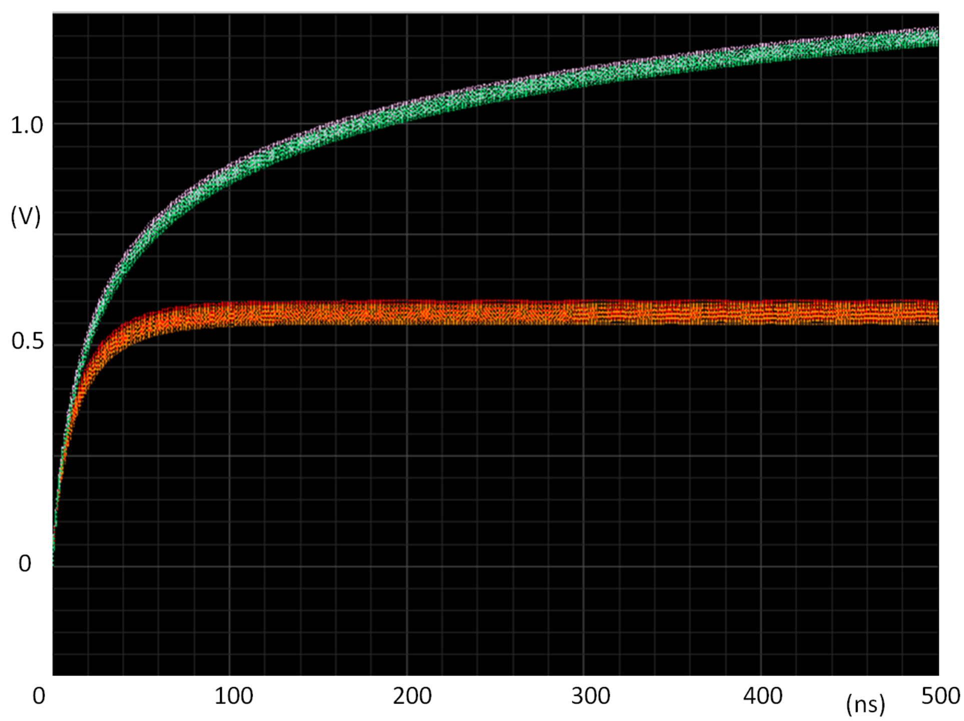

FIGURE 6.4: Multistage Simulation
Simulated output waveforms of schematic and extracted rectifier circuits for a 500 mV, 1 GHz RF input. The DC output voltage for a 10 kΩ load is about 0.6 V while the DC output for the 10 MΩ load is about 1.25 V.

input. The 4 waveforms represent the DC outputs of the schematic and extracted circuits for 10 kΩ and 10 MΩ output loads. As expected, the schematic and extracted simulation results agree very closely, and the 10 kΩ load draws more current from the rectifier, lowering the DC output voltage from 1.25 V (for a 10 MΩ load) to 0.6 V. In this state, the current drawn by the load is 60 µA, which is almost enough current to drive the Colpitts oscillator. Simulation of the overall ASIC allows precise determination of the RF input signal level required to start the Colpitts oscillator and enable data transmission.

6.2.2.2 Bias Generator

The purpose of the bias generator circuit is to generate a stable 0.6 V DC bias used by the Colpitt's oscillator. The circuit schematic is shown in Fig. 6.5. The current mirror comprised of

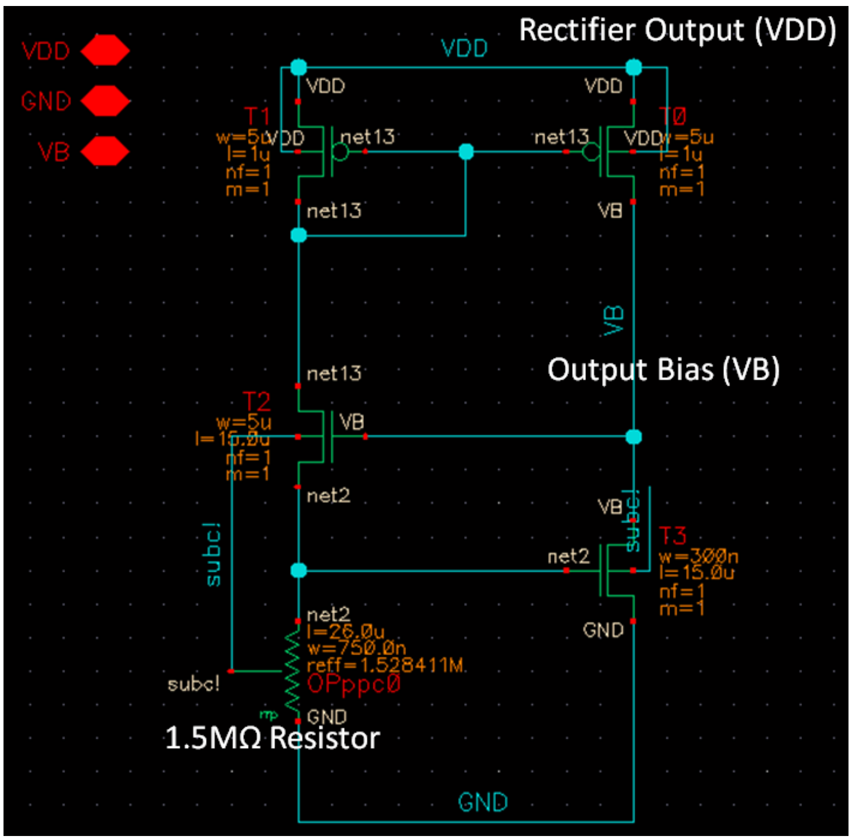

FIGURE 6.5: Bias Generator Schematic

transistors T0 and T1 ensures that the current flowing through T1 and T2 is the same as the current flowing through T0 and T3. For a typical supply voltage (VDD) of 1 V supplied by the rectifier, this current is set at 0.5 μA by the 1.5 MΩ resistor. The gate-source voltages of T2 and T3 calculated from this small current are close to threshold, implying the output bias voltage VB is approximately the sum of these voltages, and will not vary much with supply voltage. This stability against changes in supply voltage is the essential property of the circuit. A simulation of the output bias voltage for different supply (0 - 2.0 V) voltages is shown in Fig. 6.6(a), and stabilizes around 0.6 V for large enough supplies. Transistors T2 and T3 are made long

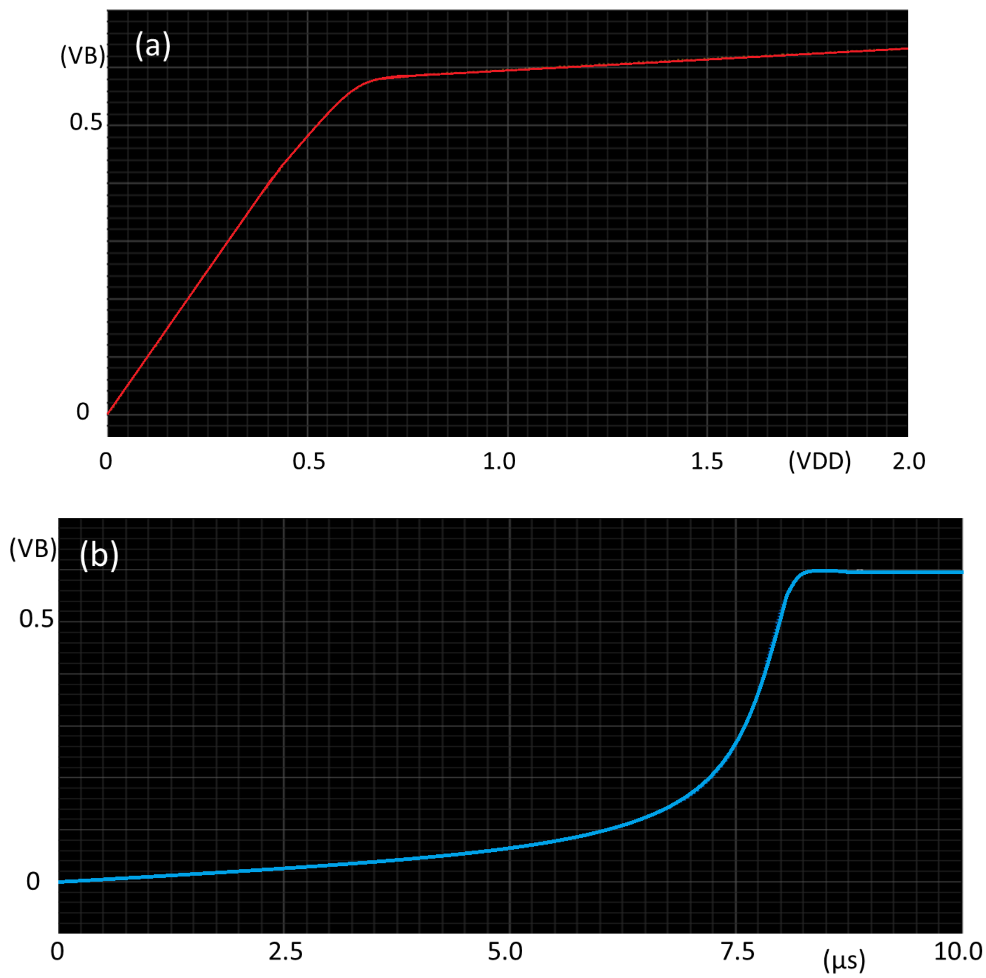

FIGURE 6.6: Bias Generator Simulation
(a) Simulated bias generator output voltage versus supply voltage. (b) 10 μs transient simulation of the bias generator output voltage when a 1 V supply voltage is applied.

(L = 15 μm) to mitigate the effects of channel length modulation on the output voltage and enhance stability.

The transient simulation shown in Fig. 6.6(b) shows the start-up behavior of the bias generator for a 1 V supply voltage. Because the bias generator circuit does not have any special start-up mechanism [86], it relies on sub-threshold conduction of the transistors to exit the unstable 0 bias state and reach the stable 0.6 V bias state. As evident from the simulation, this takes about 8 μs, and is found to be typical for supply voltages in the range of interest (3 V > VDD > 0.6 V). For a deeper understanding of the circuit`s operation, a detailed small signal analysis of its stability may be undertaken.

6.2.2.3 Colpitts Oscillator

A schematic diagram of the oscillator is shown in Fig. 6.7. This oscillator topology is often used in CMOS designs because of its ease of implementation and low phase noise [87]. When appropriate bias and supply voltages are applied, oscillation occurs near the resonant frequency $\omega = \frac{1}{\sqrt{LC}}$ of the parallel LC network connecting Out- and Out+. With each cycle of oscillation, the current flowing from VDD to GND alternately passes through transistor paths T3-T0-T2 and T4-T1-T2. In so doing, the current also passes through the LC network, whose impedance at resonance determines the current load of the oscillator. In general, the higher the quality factor Q of the tank ($Q = \frac{1}{R}\sqrt{\frac{L}{C}}$), the lower the current load and power demands of the oscillator. Power consumption is also affected by the transconductances (gains) of each transistor [84]:

$$g_m = \sqrt{2\mu_n C_{ox} \frac{W}{L} I_D}\ ,$$

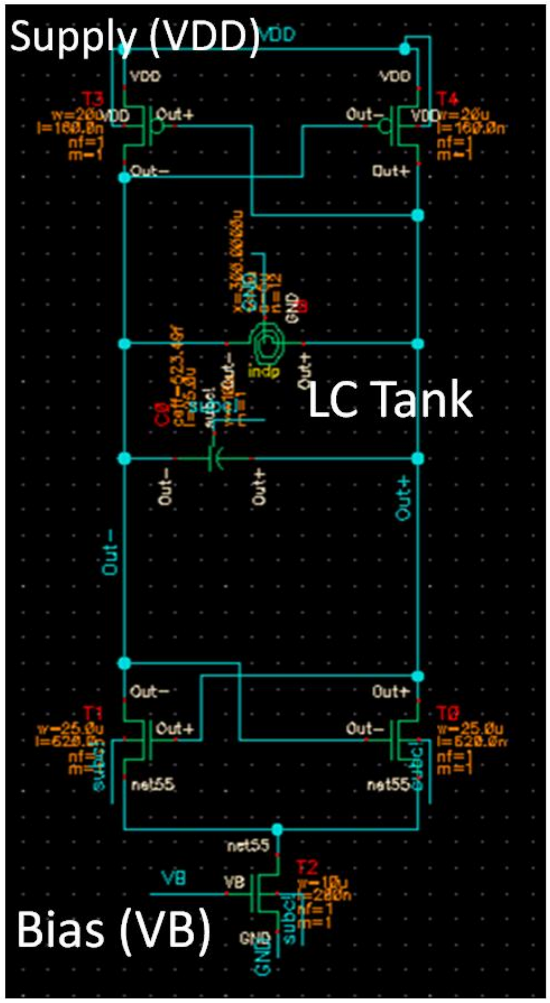

FIGURE 6.7: Colpitts Oscillator Schematic

as it decreases for increased gains [88]. This is why, to help oscillation begin, transistor dimensions with large $\frac{W}{L}$ ratios are chosen.

The oscillator inductor and capacitor are selected to set the oscillation frequency between 1 and 2 GHz, because this frequency range has been shown to be efficient for short distance wireless transmission through biological tissue [77]. For the purposes of simulation, the capacitor is given a value of 0.5 pF to represent the capacitance of a MEMS capacitive pressure sensor. The frequency range and capacitance then determine a range of possible inductor values, and a 12 turn spiral inductor with inductance 21.5 nH is selected for specificity.

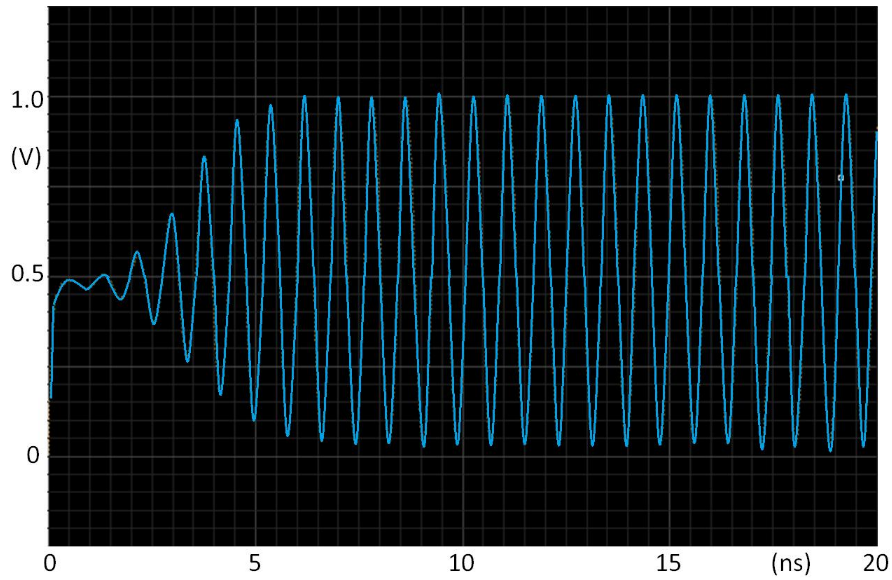

FIGURE 6.8: Oscillator Simulation, VDD = 1 V
Transient simulation of oscillator output Out+ for VDD = 1 V, VB = 0.6 V.

Fig. 6.8 shows a 20 ns transient simulation of the oscillator's Out+ voltage output for supply and bias voltages: VDD = 1 V, VB = 0.6 V. The output frequency is measured to be 1.22 GHz. This is smaller than the LC tank resonant frequency $f = \frac{1}{2\pi\sqrt{LC}} = 1.54$ GHz because of parasitic capacitance between the gate and source/drain in each of the transistors. This parasitic effect has the further negative consequence of reducing the dependence of the resonant frequency on changes in the sensor capacitance, but is necessary if a small sensor capacitance is used as a means of increasing the tank's quality factor and circuit power efficiency.

The average current drawn by the oscillator for a supply voltage of 1 V is several hundred µA, and can be significantly decreased without stopping oscillation. Fig. 6.9(a) shows the Out+ voltage waveform for VDD = 0.65 V, VB = 0.6 V. In this case, the oscillation takes longer to start, but the average current drawn is close to 100 µA (Fig. 6.9(b)), which is a more reasonable current load for the rectifier. This current is close to the minimum necessary for oscillator function, since lowering the supply voltage VDD below 0.6 stops oscillation all together. In this state, the output frequency is 1.25 GHz. The fact that the output frequency varies slightly with the supply voltage is an important effect limiting the pressure sensing resolution of the overall system.

6.2.3 Chip Level Design and Simulation

The physical layout of the rectifier, bias generator, and oscillator is shown in Fig. 6.10, where the red boxes in the view on the left indicate the positions of each primary cell, and the layout on the right shows all the intracellular detail. The layout covers an area of 0.32 mm X 0.42 mm, and is combined with test pad connections to form the final ASIC design shown in Fig. 6.11. The pads allow input of an RF power signal, and measurement of the rectifier, bias, and

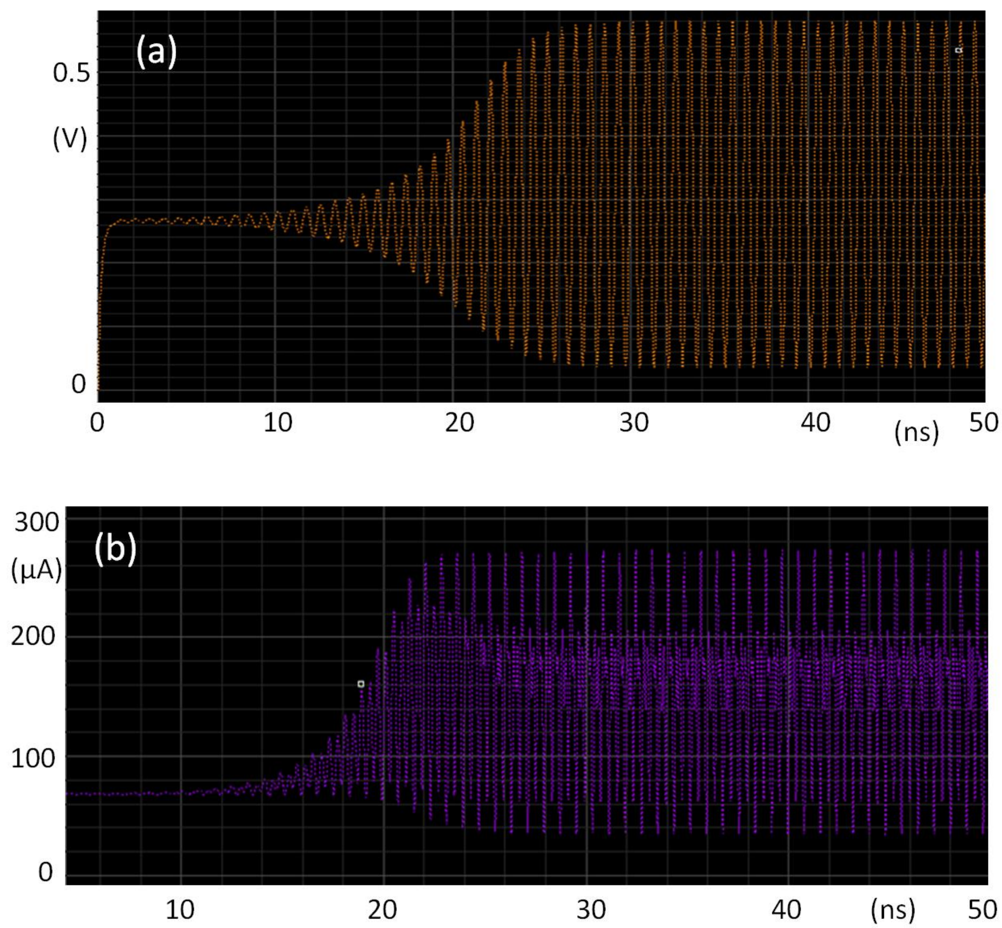

FIGURE 6.9: Oscillator Simulation, VDD = 0.65 V
Transient simulations of (a) oscillator output and (b) oscillator tail current for Out+ for VDD = 0.65 V, VB = 0.6 V.

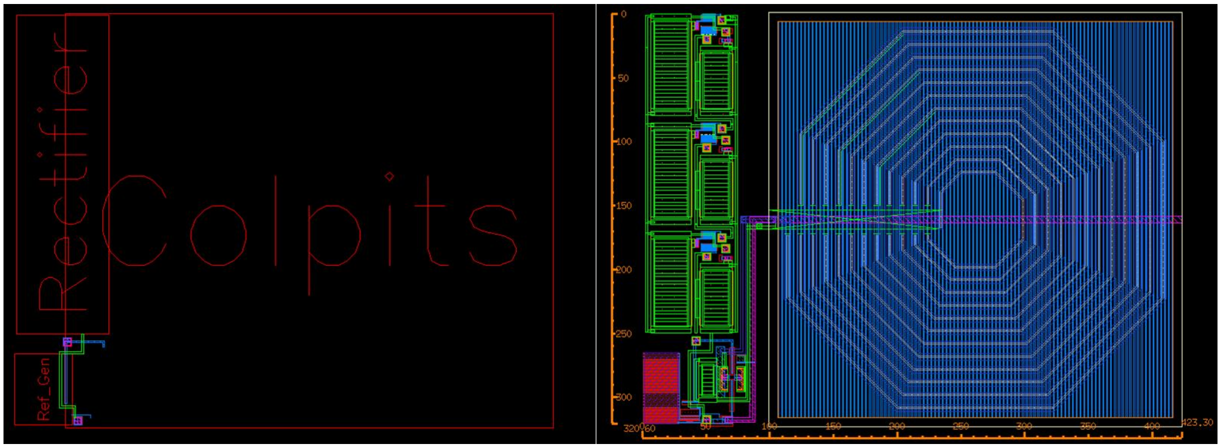

FIGURE 6.10: Layout of ASIC Primary Cells

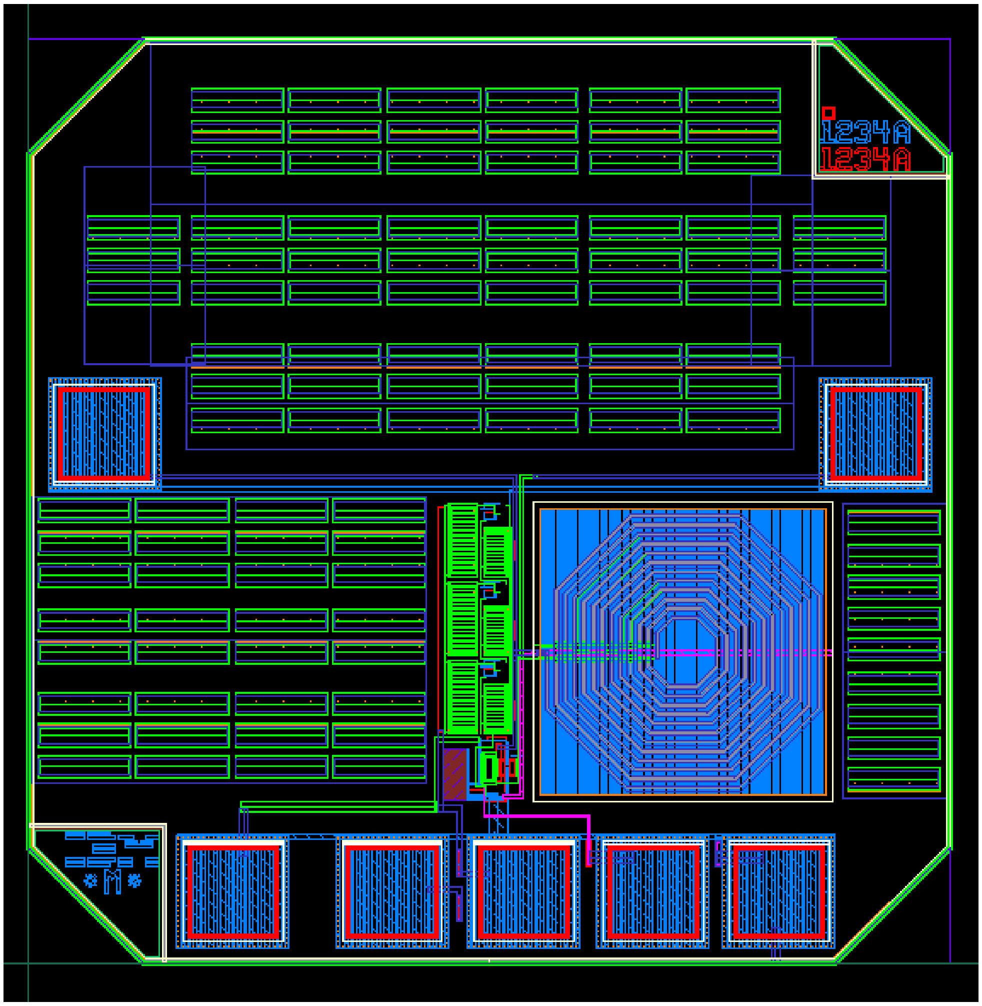

FIGURE 6.11: Chip Level ASIC Layout

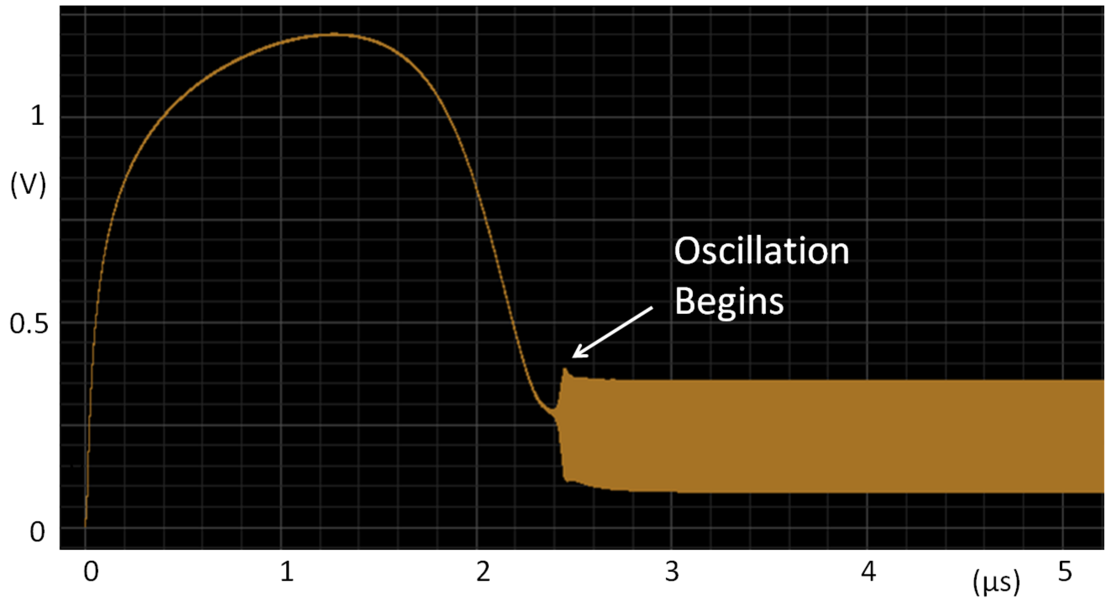

FIGURE 6.12: ASIC Output Oscillation for a 500 mV, 1 GHz RF Input Signal

and oscillator output voltages. The top metal layer (4 µm thick aluminum -IBM 130 nm process standard) in this layout is used to fill up 70% of the 1 mm X 1 mm chip area. This is so it can act as a ground plane for the stent antenna. Fig. 6.12 shows a simulation of the Out+ waveform when a 500 mV, 1 GHz RF input is applied to power the chip. Oscillation begins after ~2.5 µs has passed. The delay in start-up is due to the time required for the bias generator to reach a stable output.

Since the chip is intended to interface with a stent antenna providing the RF input signal, it is important to know its input impedance as a function of frequency. This input impedance is well defined for small input signals where transistor nonlinearity can be ignored [89], and can be computed by simulation. The real and imaginary parts of the input impedance vs frequency are shown in Fig. 6.13(a) and (b). Note that the imaginary part (reactance) is negative for frequencies between 0 and 3 GHz, corresponding to a capacitive impedance. A simple calculation shows this capacitance is 0.62 pF. This value will be used in the next section to devise a matching network for interfacing the antenna stent and ASIC.

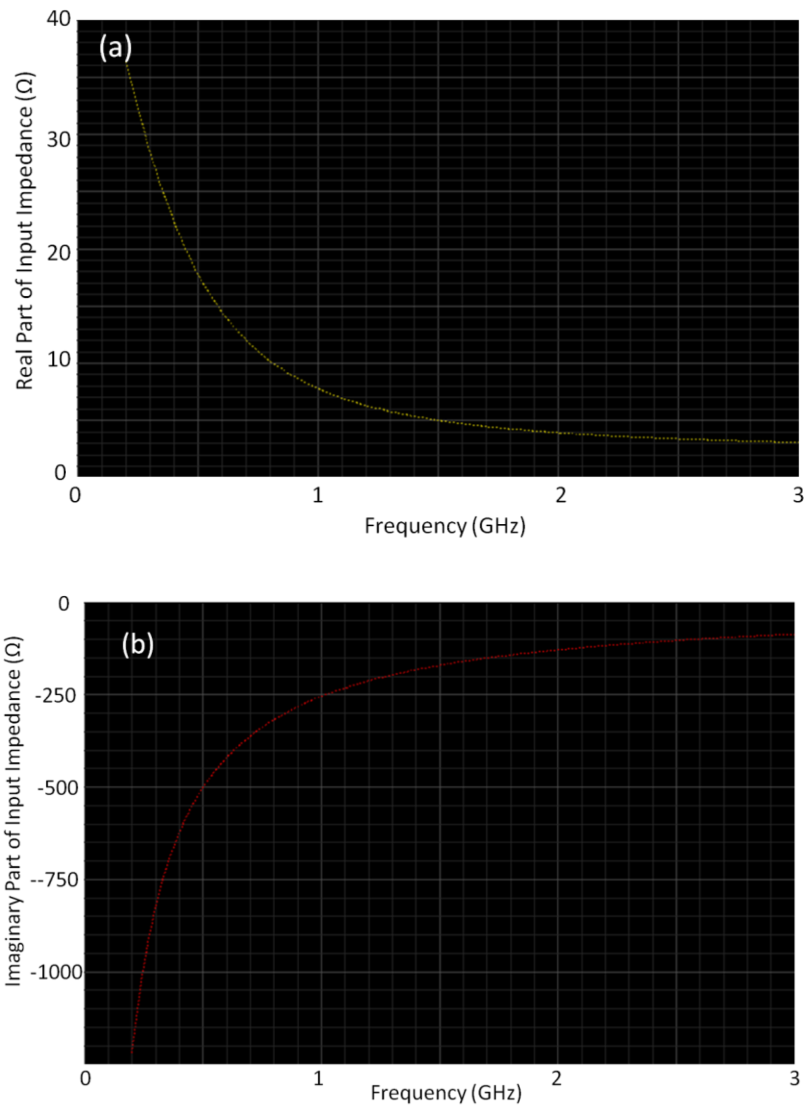

FIGURE 6.13: ASIC Input RF Input Impedance

(a) Real and (b) imaginary components of the chip input impedance from 0 - 3 GHz.

6.3 Stent Antenna

The integration of the sensor, ASIC, and stent is fundamental to electrical and mechanical performance of the overall device. To ensure efficient power harvesting, appropriate matching of the stent antenna and ASIC is required, and this in turn requires additional circuit elements at the stent-ASIC interface whose values depend on the frequency of operation, stent antenna design (including the design of the ASIC ground plane), and location of the ASIC on the stent. Thus, determination of the range at which the ASIC can be driven requires testing of different stent antennae and matching networks. To this end, only preliminary modeling (6.3.1) of an inductive stent antenna (see Chapter 3) has been performed to suggest how to best match it with the ASIC presented in Section 6.2. The decision to model the inductive stent antenna for integration with the ASIC was based on the availability of a Solid Works stent model, not because the absence of struts plays any essential role in wireless function. Further work is needed to model and directly test the power harvesting capabilities of fabricated ICs integrated with various other stent antennae and matching networks.

Mechanical integration is complicated by the need to electrically connect the ASIC to both the MEMS sensor and stent antenna. A proposal for how this might be achieved is given in Section 6.3.2, as well as explanation of any possible difficulties.

6.3.1 Electromagnetic Modeling

A Solid Works model of a stent antenna for powering and transmitting data from the ASIC is shown in Fig. 6.14. It incorporates the same helical (strutless) stent used in Chapter 3 to form LC tank devices, The other part of the stent antenna is the ASIC ground plane, modeled by the purple rectangle in the figure. The ground plane is made of aluminum, and is 5 µm thick with lateral dimensions of 1 mm X 0.75 mm. It is not intended as a perfect model of the ASIC ground plane, which is a complicated structure including many metal layers and the chip body, but merely as an approximation of the chip's top metal layers, filling up about 70% of the chip area.

Together, the stent body and ASIC ground plane form two poles of a highly asymmetric dipole antenna. Finite element simulations to compute the antenna input impedance as a function of frequency were conducted using HFSS. These simulations use the method of moments [90] to compute current distribution in the antenna for a prescribed voltage excitation between the stent and ground plane.

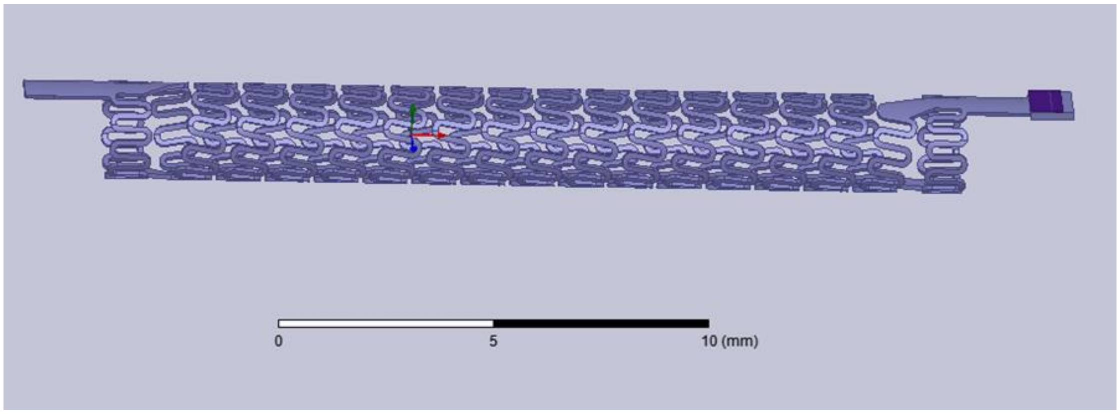

FIGURE 6.14: 3D Stent Antenna Model

The computed real and imaginary components of the antenna impedance are plotted in Fig. 6.15(a) and (b) for frequencies from 1 - 3 GHz. Like the ASIC, the antenna reactance is

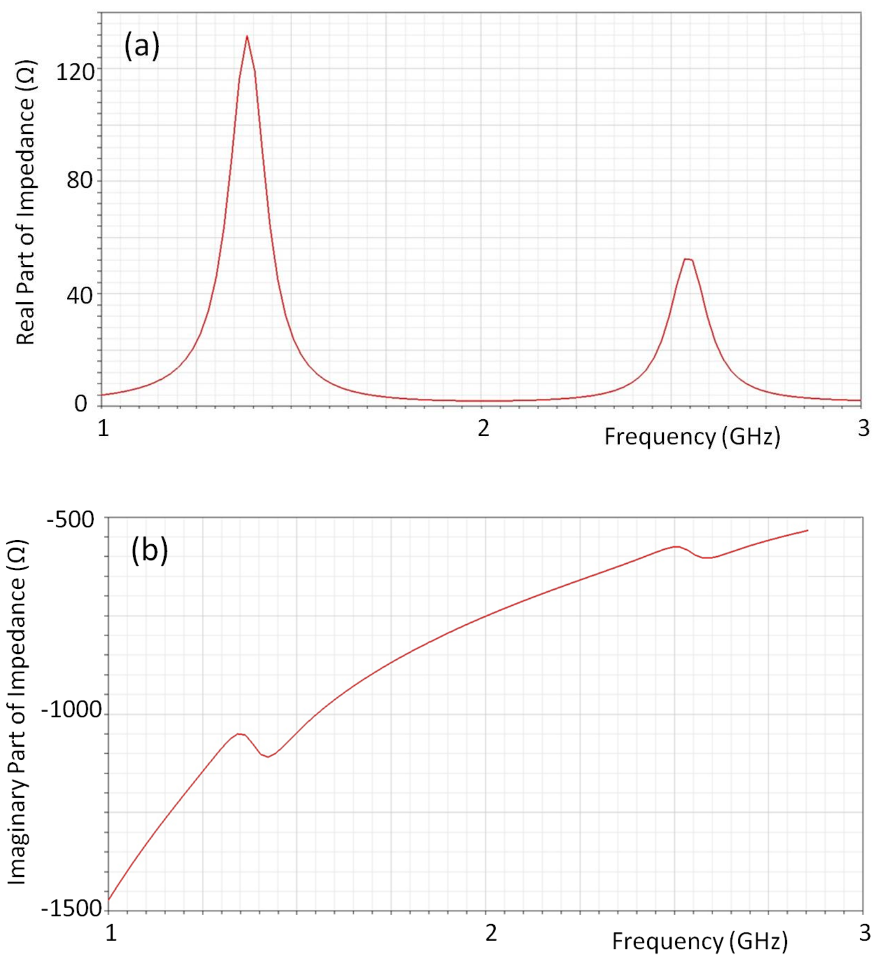

FIGURE 6.15: Stent Antenna Impedance
FEM simulated (a) real and (b) imaginary components of the stent antenna impedance (1 - 3 GHz)

negative (capacitive) over this range, so an inductor must be added at their interface to achieve matching. Matching is desirable because it amplifies the RF input signal to the rectifier from the stent, enabling wireless powering of the chip from longer distances.

One possible matching is shown schematically in Fig. 6.16(a), where a 159 nH inductor has been added to achieve matching at 1.3 GHz. At this frequency, the stent antenna has an impedance of $(30 - 1000j)\ \Omega$, which is taken as the source impedance in a simulation

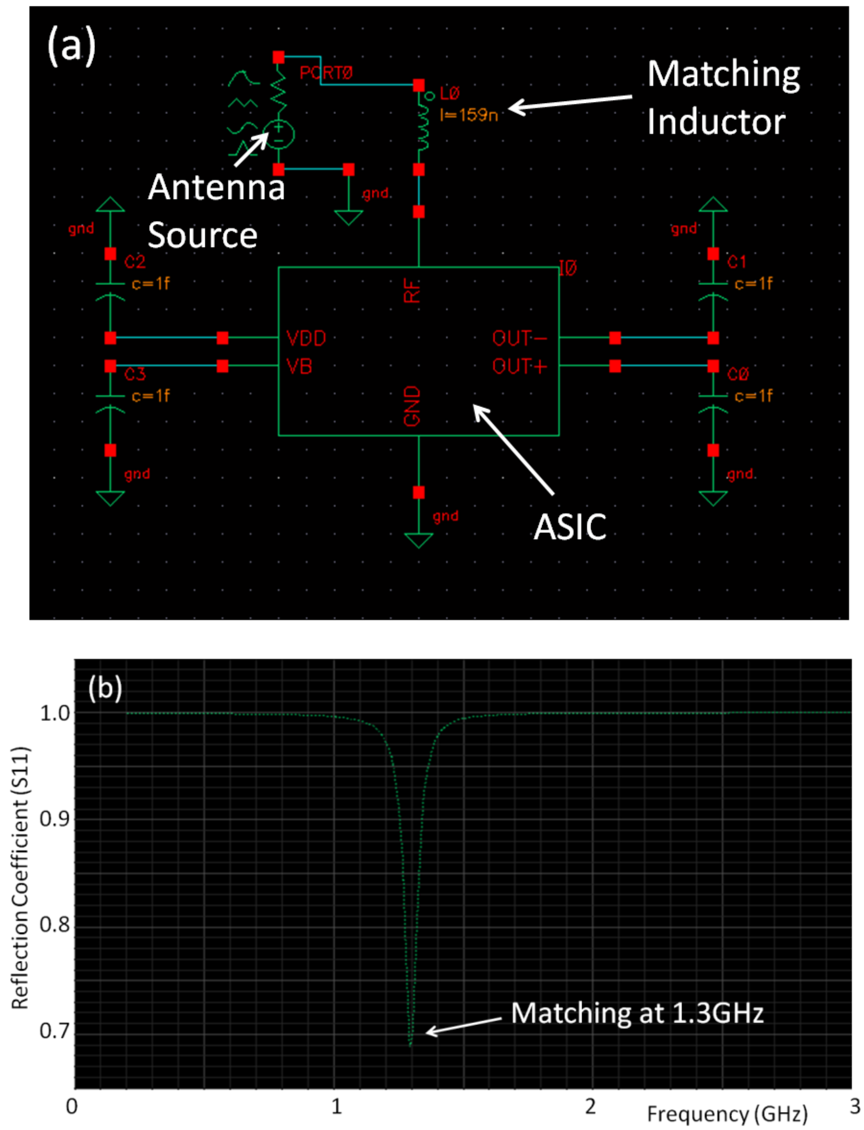

FIGURE 6.16: Stent Antenna-ASIC Matching

(a) Schematic showing the stent antenna source being matched to the ASIC at 1.3 GHz by addition of a 159 nH inductor. (b) Simulated reflection coefficient versus frequency (0 - 3 GHz).

calculating the reflection coefficient S11 as a function of frequency. The result shown in Fig. 6.16(b) verifies that matching occurs at 1.3 GHz. The width of the resonance peak depends on the sum of the real parts of the stent antenna and ASIC input impedances. When this resistance is decreased, the peak narrows and deepens, so that improved voltage amplification of the input signal is achieved over a narrower frequency band. This would suggest that matching at a higher frequency like 2 GHz where the real impedances are lower should be better for powering up the ASIC. However, further study by direct experimentation is needed to confirm this is the case.

6.3.2 Sensor-Stent-ASIC Integration

A typical method of electrically connecting CMOS integrated circuits to MEMS devices is wire bonding. However, this requires the IC and MEMS device be laterally displaced from each other rather than stacked on top of each other, which is preferable for in-stent restenosis monitoring where on-stent area for bonding chips is limited. Therefore, another method of integration that allows stacking of the MEMS sensor and IC is shown schematically in Fig. 6.17.

In this figure, the ASIC boundary and 2 of its pads for pressure sensor connection are indicated, together with the outline of a surface micromachined pressure sensor that has been fabricated on top of a through glass via (TGV) substrate. The suggestion is that the TGV substrate containing the pressure sensor could be flip chip bonded to the top of the CMOS IC for electrical and mechanical connection. Electrical and mechanical connection of the ASIC to the stent could be made by another copper via leading to the substrate surface, which could be AuSn soldered to the stent [16] for final integration. This scheme might also allow for fabrication of antenna-IC matching components (inductors) on the sensor substrate surface, to avoid having to fabricate any large matching inductor on the IC itself. Drawbacks of this approach are the

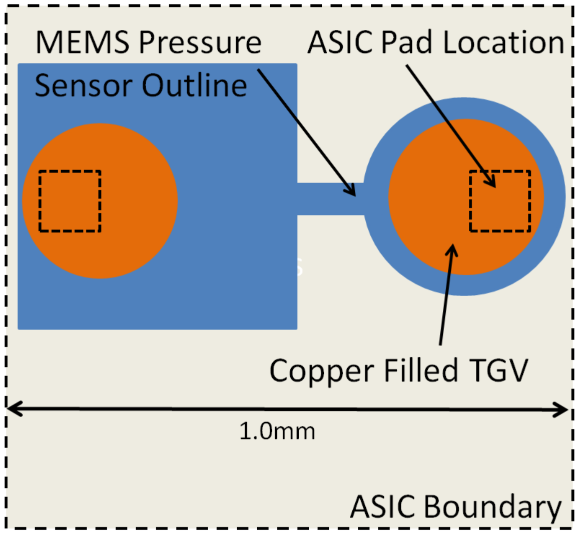

FIGURE 6.17: TGV Sensor-Stent-ASIC Integration Schematic

relatively high cost of purchasing custom TGV substrates, and that it requires additional post-processing of stents (electroplating) to enable AuSn bonding.

6.4 Discussion

The primary reason for using a CMOS based design approach to in-stent pressure monitoring is to increase the sensing range and resolution. The extent to which the ASIC designed in this chapter can enable sensing (compatible with the limits of biological radiation exposure [91]) at 2.5 cm away requires more in depth study. A study of the harvesting capabilities of stent antennae/ground planes for various commercial stents, matching networks, and ground plane dimensions would suggest an optimal frequency for wireless power transmission and give a ballpark estimate of the sensing range reasonably obtained. Redesign of ASIC rectifiers using self Vth cancellation [92-93] would allow ASICs to startup at lower RF input powers. Better understanding of the stent antenna harvesting capability and ASIC power demands would determine whether or not any external wiring is necessary for in-stent monitoring.

The question of whether or not suitable TGV substrates can be found for the integration scheme proposed in Section 6.3.2 is not known. Some commercial substrates do not have flat enough via surfaces to be used in MEMS processing, and most are quite expensive. Better understanding of matching requirements is required to determine whether or not stent antenna-IC matching components can be fabricated on MEMS sensor substrates for compact integration of all necessary components.

An important finding of the ASIC design process was that the capacitance to frequency conversion scheme for transmitting pressure data is not ideal. This is because the frequency of the oscillator depends weakly on the rectifier supply voltage, which changes with reader-stent distance and limits pressure sensing resolution. The ability to resolve the output resonant frequency also degrades with reader-stent distance. This suggests that a different means of reading and transmitting data is preferable. Other approaches [15] avoid using direct capacitance to frequency conversion, and do not require a metal-based capacitive pressure sensor with low series resistance for low power operation, enabling the possibility of using hybrid CMOS-MEMS ASICs for even more streamlined integration. Other data transmission schemes are also available, however, so in choosing the communication protocol the design requirements of the external reader should be taken into account to make a decision. For instance, an important consideration is how to probe 2 ASICs simultaneously without confusion caused by interference of their signals. If an RFID communication scheme were employed, this problem might be addressed by designing the 2 ASICs to transmit pressure information at different times, or by using more advanced anti-collision algorithms [94], although further analysis of the issue is necessary. An advantage of utilizing the RFID communication protocol for data transmission is that it allows use of pre-existing RFID readers for accelerated prototyping.

Chapter 7: Conclusion

Section 7.1 lists the original contributions to research I made during my doctoral studies and documented within this thesis. Since the goal of this research has to been to design a wireless pressure monitoring system for early restenosis detection, Section 7.2 assesses the extent to which this original objective has been achieved, and where future efforts are best directed to make further advances.

7.1 Contributions

Items 1 - 5 explain original contributions to research contained in Chapters 2 - 6:

1. Design and fabrication of a capacitive pressure sensor using stainless steel as a primary working material. This sensor uses non-standard micromachining and bonding techniques to work with materials that lower its series resistance and enable laser welding of it to a stent. This represents a new approach to capacitive pressure sensor fabrication. Description of sensor fabrication is given in Section 2.2. The results of characterizing sensor response to pressure and temperature are presented in Section 2.3.
2. The integration of a capacitive pressure sensor and custom designed stent to form an improved version of a previous telemetric stent system. Integrated devices have been tested *in vitro* (Section 3.4) to determine their clinical potential. The tests highlight difficulties with device deployment and communication range that must be addressed before use in humans is a possibility (Section 3.5). This is the first research to clarify the challenges faced by the inductive stent based approach to in-stent restenosis monitoring.
3. In depth review of methods for wirelessly reading an LC tank's resonant frequency. Tests are

conducted using the impedance phase (Section 4.1) and ring-down (Section 4.2) read methods. This is the first range test of inductive stent based devices, and results indicate that read range can be extended by using the ring-down method (Section 4.2.2). Results did not show any advantage in sensing range conferred by using inductive stent based devices instead of planar LC tanks a few square millimeters in area (Section 4.2.3). Planar tank devices tested also showed better performance in saline than inductive stent devices. Sensing range sufficient for carotid artery sensing (2.5 cm) may be achieved with improvements to the ring-down method (Section 4.2.4).

4. Design and fabrication (Sections 5.2 and 5.3) of a surface micromachined capacitive pressure sensor. The sensor uses a thick copper membrane to reduce its series resistance for incorporation in a proposed high quality factor LC tank pressure sensing system (Section 5.5). The sensor fabrication process developed represents a new approach to capacitive pressure sensor fabrication, and although further work is needed to realize the objective, it is intended to produce sensors with higher sensitivity than all previously fabricated all-metal capacitive pressure sensors.

5. A preliminary design of a CMOS based in-stent telemonitoring system is presented (Section 6.2), where the stent and ASIC ground plane act together as an asymmetric dipole antenna to power the IC. Electromagnetic modeling of the antenna's impedance and simulation of its matching withthe ASIC are performed for the first time (Sections 6.2 and 6.3), helping identify desirable features of a CMOS based approach to wireless in-stent pressure monitoring (Section 6.4). The primary research objectives of this work are to determine if external wiring is necessary to drive an IC from distances relevant to in-stent monitoring (2.5 cm), and investigate sensor-stent-ASIC integration possibilities. Further direct testing is needed to investigate these

issues.

7.2 Conclusions and Future Work

The goal of this thesis has been to find a means of wirelessly monitoring blood pressure inside a vascular stent, for early detection of in-stent restenosis. This condition endangers a significant percentage of stent recipients by re-blocking blood vessels stents have been deployed to hold open. Since most patients with coronary stents never receive an angiogram to monitor their stent status, an inexpensive and simple wireless monitoring system would be beneficial in providing early notification of severe restenosis for safer and more effective treatment.

The original focus of my doctoral research was to implement a monitoring system using a particular design approach proposed previously [14]. The objective in following this same approach was to make several modifications to the old design to enhance its performance and see if it could work clinically. After conducting tests *in vitro*, there are several clear problems with this approach that remain unaddressed. These problems are discussed at length in Section 3.5. Many of the problems are caused by the use of inductive stents in which all struts have been removed.

Range tests conducted using the impedance phase and ring-down methods showed that a small (2.5 mm $\times$ 2.5 mm) planar LC tank could be wirelessly interrogated from the same range as an inductive stent device deployed in a graft (Sections 4.1.4 and 4.2.2 - 4.2.3), and that such devices maintained their performance better in a conductive medium (Section 4.2.2). These tests also showed better sensing range using the ring-down method in all cases, and indicated that if ring-down excitation power can be increased and/or antenna switching transients reduced, a clinically relevant sensing range of $>$2.5 cm is obtainable (adequate for carotid artery monitoring). In this case, an expedient route to designing a smart stent may be to integrate two MEMs LC tank wireless pressure sensors on either end of a commercial stent. This approach removes the costly and time consuming process of re-designing the helical stent to solve the problems it introduces, and also removes the need for any additional wiring, making deployment less risky. Efforts directed towards development of a high Q MEMs LC tank are explained in Chapter 5. More work is necessary to improve the fabrication process to produce sensors with sensitivity in agreement with modeling, and realize operational LC tank pressure sensors. Hermetically sealing sensors with PECVD deposited SiO_2 and ALD deposited Al_2O_3 appears to be one way of doing this. However, until this progress is made and sensing range is extended, suitability of these devices for in-stent restenosis monitoring is not known.

Design approaches using CMOS integrated circuits appear promising for increasing sensing range, and, to this end, ASIC designs have been suggested by project collaborators. These ASICs can function with a typical commercial stent, but require an external wire. The advantage of having a wire is that it makes powering the integrated circuit easier, while the disadvantage is that it introduces new packaging and deployment issues that must be carefully considered. Design approaches that avoid the use of additional wiring face the challenge of how to design the IC ground plane and stent-chip interface to achieve a read range useful for *in vivo* monitoring. An initial attempt at such a design is presented in Chapter 6, based on one of the architectures published by project collaborators [28]. The primary motivations for designing this chip were to evaluate its start-up behavior with different stent antennae and matching networks, and experiment with sensor-stent-IC integration (see proposal in Section 6.3.2). These tests, which have not yet been conducted, might help determine whether or not additional wiring is necessary for a CMOS based solution to in-stent monitoring, and what practical difficulties exist with respect to device integration. Nevertheless, the IC design process has been instructive in pointing out which features of an IC design are and are not desirable for in-stent monitoring.

Evidently, the original objective of producing a practical in-stent blood pressure monitor has not yet been met. However, different design approaches have been evaluated, pointing out clear problems with the original inductive stent approach that must be overcome, and suggesting alternative approaches based on MEMS LC tank sensing and CMOS integrated circuit design. Of the two, the CMOS based approach has the advantage of longer wireless sensing range, although it is more complex in its electrical and mechanical design/integration. For instance, beyond the complications of IC design, a CMOS based restenosis monitor must use a wireless protocol enabling the reading of two separate ASIC pressure readings simultaneously, and must integrate three components (sensor, stent, and ASIC) electrically and mechanically rather than two (stent and MEMS LC tank) mechanically. CMOS integration also requires antenna-IC matching circuitry for optimal wireless performance, which complicates integration further if it cannot be incorporated as part of the IC design. Nevertheless, if the range of LC tank sensing cannot be significantly increased, CMOS based design may offer the only solution to in-stent monitoring, particularly in deeper blood vessels such as the coronary arteries.

From a wider perspective, there is the question of whether wireless in-stent pressure measurement is a useful tool for monitoring by patients at home or only usable under supervision of physicians. Studies have shown that measurements of fractional flow reserve (computed from pressure measurements) across a vessel best predict the presence of stenosis when the patient is in a state of maximum vasodilation, and induction of this state requires heavy exercise or administration of a drug in-hospital [95]. Given the age and condition of most patients receiving stents, this suggests that smart stents might only be effective as diagnostic tools for use inside hospitals. Therefore, to determine if smart stents have any utility to doctors, one simple solution is to build a prototype smart stent using MEMS LC tanks and conduct trials *in vitro* to evaluate its efficacy in predicting restenosis. Then, if results appear promising to medical professionals, further effort could be devoted to extending sensing range and/or developing a CMOS based system, since development of a CMOS system and/or redesigning the stent is much more time consuming and expensive. Ideally, for a CMOS system, an integrated CMOS/MEMS fabrication process should be used to produce the sensors directly on the ICs, and appropriate reader technology for communicating with the stent antenna should be developed. Such technology would enable FFR measurements in-hospital with administration of vasodilators, allowing evaluation of the efficacy of smart stents as restenosis monitors.

References

1. Y. Gurevich, A. McFarlane, K. Morris, A. Jokovic, G. Peterson, and G. Webster, “Estimating the number of coronary artery bypass graft and percutaneous coronary intervention procedures in Canada: A Comparison of cardiac registry and Canadian Institute for Health information data sources,” *Canadian Journal of Cardiology*, vol. 26(7), 2010, pp. 249 - 253.
2. R. Riley, C. Don, W. Powell, C. Maynard and L. Dean, "Trends in Coronary Revascularization in the United States from 2001 to 2009,” *Circ Cardiovasc Qual Outcomes*, vol. 4(2), 2011, pp. 193 - 197.
3. Wikipedia contributors. (2014, February 2). *Restenosis*. [Online]. Available: http://en.wikipedia.org/wiki/Restenosis (accessed April 9, 2014)
4. M. Brown, and J. Goldstein, “Lipoprotein Metabolism in the Macrophage: Implications for Cholesterol Deposition in Atherosclerosis,” *Ann. Review Biochem.*, vol. 52, 1983, pp. 223 - 261.
5. J. McGarry, B. O’Donnell, P. McHugh, and J. McGarry, “Analysis of the mechanical performance of a cardiovascular stent design based on micromechanical modelling,” *Computational Materials Science*, vol. 31, 2004, pp. 421 - 438.
6. N. Scott, “Restenosis following implantation of bare metal coronary stents: Pathophysiology and pathways involved in the vascular response to injury,” *Advanced Drug Delivery Reviews*, vol. 58, 2006, pp. 358 - 376.
7. J. Moses, M. Leon, J. Popma, P. Fitzgerald, D. Holmes, C. O’Shaughnessy, R. Caputo, D. Kereiakes, D. Williams, P. Teirstein, J. Jaeger, and R. Kuntz, “Sirolimus-Eluting Stents versus Standard Stents in Patients with Stenosis in a Native Coronary Artery,” *The New England Journal of Medicine*, vol. 349(14), 2003, pp. 1315 - 1323.
8. G. Stone, S. Ellis, D. Cox, J. Hermiller, C. O’Shaughnessy, J. Tift Mann, M. Turco, R. Caputo, P. Bergin, J. Greenberg, J. Popma, and M. Russell, “One-Year Clinical Results with Slow-Release, Polymer-Based, Paclitaxel-Eluting TAXUS Stent: The TAXUS-IV

Trial," *Circulation*, vol. 109, 2004, pp. 1942 - 1947.

9. H. Brunner-La Rocca, C. Kaiser, A. Bernheim, M. Zellweger, R. Jeger, P. Buser, S. Osswald, and M. Pfisterer, "Cost-effectiveness of drug-eluting stents in patients at high or low risk of major cardiac events in the Basel Stent KostenEffektivitäts Trial (BASKET): an 18 month analysis," *the Lancet*, vol. 370, 2007, pp. 1552 - 1559.
10. T. Lüscher, J. Steffel, F. Eberli, M. Joner, G. Nakazawa, F. Tanner, and R. Virmani, "Drug-Eluting Stent and Coronary Thrombosis: Biological Mechanisms and Clinical Implications," *Circulation*, vol. 115, 2007, pp. 1051 - 1058.
11. G. Dangas, F. Kuepper, "Restenosis: repeat narrowing of a coronary artery: prevention and treatment," *Circulation*, vol. 105(22), 2002, pp. 2586 - 2587.
12. B. Heilbron, G. Andrews, S. Isserow, and B. Forster, "Coronary computed tomographic angiography in British Columbia: A review," *BC Medical Journal*, vol. 49(2), 2007, pp. 78 - 84.
13. G. Dangas, and F. Kuepper, "Restenosis: repeat narrowing of a coronary artery: prevention and treatment," *Circulation*, vol. 105(22), 2002, pp. 2586 - 2587.
14. M. Fenster, and A. Govari, "Pressure-Sensing Stent," U.S. Patent 6,053,873, issued April 25, 2000.
15. K. Takahata, A. DeHennis, K. Wise, and Y. Gianchandani, "Stentenna: A Micromachined Antenna Stent for Wireless Monitoring of Implantable Microsensors," *Proceedings of the 25th Annual International Conference of the IEEE EMBS*, 2003, pp. 3360 - 3363.
16. E. Chow, A. Chlebowski, S. Chakraborty, W. Chappell, and P. Irazoqui, "Fully Wireless Implantable Cardiovascular Pressure Sensor Monitor Integrated with a Medical Stent," *IEEE Transactions on Biomedical Engineering*, vol. 57(6), 2010, pp. 1487 - 1496.
17. N. Pijls, J. van Son, R. Kirkeeide, B. De Bruyne, and K. Gould, "Experimental basis of determining maximum coronary, myocardial, and collateral blood flow by pressure measurements for assessing functional stenosis severity before and after percutaneous transluminal coronary angioplasty," *Circulation*, vol. 87(4), 1993, pp. 1354 - 1367.
18. B. De Bruyne, J. Bartunek, S. Sys, and G. Heyndrickx, "Relation Between Myocardial Fractional Flow Reserve Calculated from Coronary Pressure Measurements and

Exercise-Induced Myocardial Ischemia," *Circulation*, vol. 92(1), 1995, pp. 39 - 46.

19. T. Donahue, M. Kern, F. Aguirre, R. Bach, T. Wolford, C. Bell, and J. Segal, "Assessing the hemodynamic significance of coronary artery stenosis: Analysis of translesional pressure-flow velocity relations in patients," *JACC*, vol. 22(2), 1993, pp. 449 - 458.
20. K. Takahata, Y. Gianchandani, and K. Wise, "Micromachined Antenna Stents and Cuffs for Monitoring Intraluminal Pressure and Flow," *Journal of Microelectromechanical Systems*, vol. 15(5), 2006, pp. 1289 - 1298.
21. W. Eaton, and J. Smith, "Micromachined Pressure Sensors: Review and Recent Developments," *Smart Materials and Structures*, vol. 6(5), 1997, pp. 530 - 541.
22. E. Park, J. Yoon, and E. Yoon, "Hermetically sealed inductor-capacitor (LC) resonator for remote pressure monitoring," *Japan Journal of Applied Physics*, vol. 37, 1998, pp. 7124 - 7218.
23. O. Akar, T. Akin, and K. Najafi, "A wireless batch sealed absolute capacitive pressure sensor," *Sensors and Actuators A*, vol. 95, 2001, pp. 29 - 38.
24. M. Allen, "Micromachined endovascularly-implantable wireless aneurysm pressure sensors: from concept to clinic," *Transducers*, vol. 1, 2005, pp. 275 - 278.
25. P. Chen, D. Rodger, S. Saati, M. Humayun, and Y. Tai, "Microfabricated implantable parylene-based wireless passive intraocular pressure sensors," *J. Microelectromech. Syst.*, vol. 17(6), 2008, pp. 1342 - 1351.
26. H. Yoon, J. Jung, and S. Yang, "Micro devices for a cerebrospinal fluid (CSF) shunt system," *Sensors and Actuators A: Physical*, vol. 110, 2004, pp. 68 - 76.
27. B. Paden, B. Norling, and J. Verkaik, "Telemetry Method and Apparatus Using Magnetically-Driven MEMs Resonant Structure," WIPO Patent 2008060649, issued May 23, 2008.
28. G. Fonarow, "Heart failure: Wireless hemodynamic monitoring - a new approach for managing HF," *Nature Reviews Cardiology*, vol. 8, 2011, pp. 245 - 246.
29. Courtesy of CardioMEMs Inc.
30. K. Keikhosravy, P. Kamalinejad, S. Mirabbasi, K. Takahata, and V. Leung, "An Ultra-Low-Power Monitoring System for Inductively Coupled Biomedical Implants," *IEEE International Symposium on Circuits and Systems*, 2013, pp. 2283 - 2286.

31. N. Najafi, and C. Rich, “Systems for monitoring the physiologic parameters of patients with congestive heart failure,” US Patent 7,615,010, issued Nov. 10, 2009.
32. K. Stangel, S. Kolnsberg, D. Hammerschmidt, and B. Hosticka, K. Trieu, and W. Mokwa, “A Programmable Intraocular CMOS Pressure Sensor System Implant,” *IEEE Journal of Solid State Circuits*, vol. 36(7), 2001, pp. 1094 - 1100.
33. R. Schlierf, M. Gortz, T. Schmitz Rode, W. Mokwa, U. Schnakenberg, and K. Trieu, “Pressure Sensor Capsule to Control the Treatment of Abdominal Aortic Aneurysms,” *13th International Conference on Transducers*, 2005, pp. 1656 - 1659.
34. T. van den Boom, D. Tessmann, R. Lerch, G. Vom Bogel, D. Hammerschmidt, J. Amelung, B. Hosticka, and P. Mahdavi, “Remote CMOS pressure sense chip with wireless power and data transmission,” *IEEE International Solid-Sate Circuits Conference*, 2000, pp. 186 - 187.
35. P. Fletter, S. Majerus, Peng Cong, M. Damaser, W. Ko, D. Young, and S. Garverick, “Wireless Micromanometer System for Chronic Bladder Pressure Monitoring,” *International Conference on Networked Sensing Systems*, 2009, pp. 1 - 4.
36. A. DeHennis, and K. Wise, “A Fully Integrated Multisite Pressure Sensor for Wireless Arterial Flow Characterization,” *Journal of Microelectromechanical Systems*, vol. 15(3), 2006, pp. 678 - 685.
37. A. Ginggen, Y. Tardy, R. Crivelli, T. Bork, and P. Renaud, “A Telemetric Pressure Sensor System for Biomedical Applications,” *IEEE Transactions on Biomedical Engineering*, vol. 55(4), 2008, pp. 1374 - 1381.
38. M. Frischholz, “Wireless pressure monitoring systems,” *Medical Device Technology*, vol. 17(7), 2006, pp. 24 - 27.
39. P. Nikitin and K. Rao, “Theory and Measurement of Backscattering from RFID Tags,” *IEEE Antennas and Propagation Magazine*, vol. 48(6), 2006, pp. 212 – 218.
40. P. Chen, S. Rohit Varma, M. Humayun, and YC Tai, “Wireless intraocular pressure sensing using microfabricated minimally invasive flexible-coiled LC sensor implant,” *Journal of MEMS*, vol. 19, 2010, pp. 721 - 734.

41. MicroFAB Bremen GmbH, *Capacitive Pressure Sensor E1.3N*. [Online]. Available: http://www.microfab.de/downloads/20080109datasheete1.3na4.pdf (accessed April 9, 2014)

42. G. Voskerician, M. Shive, R. Shawgo, H. von Recum, J. Anderson, M. Cima, and R. Langer, "Biocompatibility and biofouling of MEMs drug delivery devices," *Biomaterials*, vol. 24, 2003, pp. 1959 - 1967.

43. D. Brox, A.R. Mohammadi, and K. Takahata, "Non-lithographically microfabricated capacitive pressure sensor for biomedical applications." *Electronics Letters*, vol. 47(18), 2011, pp. 1015 - 1017.

44. D. Brox, A.R. Mohammadi, K. Takahata, "Non-Lithographically Micromachined Capacitive Pressure Sensor Based on Stainless Steel for Biomedical Applications," *IEEE Sensors,* 2011, pp. 312 - 315.

45. D. Ziegler, T. Suzuki, and S. Takeuchi, "Fabrication of flexible neural probes with built-in microfluidic channels by thermal bonding of parylene," *J. Microelectromech. Syst*., vol. 15(6), 2006, pp. 1477 - 1482.

46. F. Niklaus, P. Enoksson, E. Kalvesten, and G. Stemme, "Low-temperature full wafer adhesive bonding," *J. Micromech. Microeng.*, vol. 11, 2001, pp. 100 - 107.

47. W. Ko, and Q. Wang, "Touch mode capacitive pressure sensors," *Sens. Actuators A, Phys.*, vol. 75(3), 1999, pp. 242 - 251.

48. J. Licari, *Coating materials for electronic applications*, Norwich, William Andrew Publishing, 2003.

49. B. Assadsangabi, X. Chen, D. Brox, "Microfabrication of Capacitive Pressure Sensors using Ferrofluid Sacrificial Layers*," IEEE Sensors,* 2013, pp. 703 - 706.

50. B. Assadsangabi, X. Chen, D. Brox, and K. Takahata, "Ferrofluid Sacrificial Microfabrication of Capacitive Pressure Sensors," *IEEE Sensors*, accepted, 2014.

51. C. Chaitanya, and K. Takahata, "MEMs-based batch-mode micro-electro-discharge-machining using microelectrode arrays actuated by hydrodynamic force," *Proceedings of the IEEE 22nd International Conference on MEMs*, 2009, pp. 705 - 708.

52. X. Chen, D. Brox, B. Assadsangabi, Y. Hsiang, and K. Takahata, "Intelligent Telemetric Stent for Wireless Monitoring of Intravascular Pressure and its In-Vivo Testing,"

Biomedical Microdevices, (2014), doi: 10.1007/s10544-014-9879-8.

53. A.R. Mohammadi, M. Mohamed Ali, D. Lappin, C. Schlosser, and K. Takahata, "Inductive antenna stent: design, fabrication, and characterization," *J. Micromech. Microeng*, vol. 23, 2013, pp. 1 - 9.
54. D. Lappin, A.R. Mohammadi, and K. Takahata, "An experimental study of electrochemical polishing for micro-electro-discharge-machined stainless-steel stents," *Journal of Materials Science: Materials in Medicine*, vol. 23(2), 2012, pp. 349 - 356.
55. A. Fontaine, K. Koeling, S. Passos, J. Cearlock, R. Hoffman, and D. Spigos, "Polymeric surface modifications of tantalum stents," *J. Endovasc. Surg.*, vol. 3, 1996, pp. 276 - 283.
56. M. Strozzi, and D. Anic, "Comparison of stent graft, sirolimus stent, and bare metal stent implanted in patients with acute coronary syndrome: clinical and angiographic follow-up," *Croat Med J.*, vol. 48, 2007, pp. 348 - 352.
57. P. Chen, S. Saati, R. Varma, M. Humayun, and Y. Tai, "Wireless intraocular pressure sensing using microfabricated minimally invasive flexible-coiled LC sensor implant," *J. Microelectromech. Syst.*, vol. 19(4), 2010, pp. 721 - 734.
58. C. Lambert, F. Gayzik, and J. Stitzel, "Characterization of the carotid and adjacent anatomy using non-contrast CT for biomechanical model development," *Biomed. Sci. Instrum.*, vol. 43, 2007, pp. 330 - 335.
59. B. Lal, K. Beach, G. Roubin, H. Lutsep, W. Moore, M. Malas, D. Chiu, N. Gonzales, J. Burke, M. Rinaldi, J. Elmore, F. Weaver, C. Narins, M. Foster, K. Hodgson, A. Shepard, J. Meschia, R. Bergelin, J. Voeks, G. Howard, and T. Brott, "Restenosis after carotid artery stenting and endarterectomy: a secondary analysis of CREST, a randomised controlled trial," *Lancet Neurol.*, vol. 11(9), 2012, pp. 755 - 763.
60. Microchip Application Note AN678, *RFID coil design*. [Online]. Available: http://ww1.microchip.com/downloads/en/appnotes/00678b.pdf (accessed April 9, 2014)
61. L. Lorenz, "Über die Fortpflanzung der Elektrizität," *Annalen der Physik*, VII, 1879, pp. 161 - 193.
62. Agilent Technologies, *Agilent Spectrum Analyzer Basics*. [Online]. Available: http://cp.literature.agilent.com/litweb/pdf/5952-0292.pdf (accessed April 9, 2014)

63. C. Moler, *Numerical Computing with MATLAB*. [Online]. Available: http://www.mathworks.com/moler/chapters.html (accessed April 9, 2014)
64. J. Skewchuk, *An introduction to the conjugate gradient method without the agonizing pain*. [Online]. Available: http://www.cs.cmu.edu/~quake-papers/painless-conjugate-gradient.pdf (accessed April 9, 2014)
65. K. Ong, C. Grimes, C. Robbins, and R. Singh, "Design and application of a wireless, passive, resonant-circuit environmental monitoring sensor," *Sens. Actuators A, Phys.*, vol. 93(1), 2001, pp. 33 - 43.
66. R. Simons, D. Hall, and F. Miranda, "RF Telemetry System for an Implantable bio-MEMs sensor," *2004 International Microwave Symposium*. Fort Worth, Texas (USA), June 6 - 11, 2004, pp. 1433 - 1436.
67. D. Brox, X. Chen, S. Mirabbasi, and K. Takahata, "Ring-Down Wireless Reading of Resonant Smart Stents," under review, 2014.
68. J. Joy, J. Kroh, M. Ellish, M. Allen, M. Pyle, "Communicating with Wireless Implanted Sensor," US Patent 7,245,117, issued July 17, 2007.
69. M. Fonesca, M. Allen, J. Kroh, J. White, "Flexible Wireless Passive Pressure Sensors for Biomedical Applications," *Tech. Dig. Solid-State Sensor, Actuator, and Microsystems Workshop*. Hilton Head, 2006.
70. M. Habibi, E. Lueder, T. Kallfass, and D. Horst, "A surface micromachined capacitive absolute pressure sensor array on a glass substrate," *Sensors and Actuators A: Physical*, vol. 46(1), 1995, pp. 125 - 128.
71. S. Chang, and M. Allen, "Demonstration for integrating capacitive pressure sensors with read-out circuitry on stainless steel substrate." *Sensors and Actuators A: Physical*, vol. 116(2), 2004, pp. 195 - 204.
72. J. Bergqvist, and J. Gobet, "Capacitive microphone with a surface micromachined backplate using electroplating technology," *Journal of MEMS*, vol. 3(2), 1994, pp. 69 - 75.
73. A. Chavan, and K. Wise, "Batch-processed vacuum-sealed capacitive pressure sensors," *Journal of MEMS*, vol. 10(4), 2001, pp. 580 - 588.
74. R. Levy, L. Chen , J. Grow, and Y. Yu, "A comparative study of plasma enhanced chemically vapor deposited SiOH and SiNCH films using the environmentally benign

precursor diethylsilane," *Materials Letters*, vol. 54, 2002, pp. 102 - 107.

75. A. Ghosh, L. Gerenser, C. Jarman, and J. Fornalik, "Thin-film encapsulation of organic light-emitting devices," *Applied Physics Letters*, vol. 86(22), 2005, pp. 223503.
76. S. Mohan, M. Hershenson, S. Boyd, and T. Lee, "Simple Accurate Expressions for Planar Spiral Inductances," *IEEE Journal of Solid State Circuits*, vol. 34(10), 1999, pp. 1419 - 1424.
77. A. Poon, S. O'Driscoll, and T. Meng, "Optimal frequency for wireless power transmission into dispersive tissue," *IEEE Transactions on Antennas and Propagation*, vol. 58(5), 2010, pp. 1739 - 1750.
78. E. Chow, Y. Ouyang, B. Beier, W. Chappell, and P. Irazoqui, "Evaluation of Cardiovascular Stents as Antennas for Implantable Wireless Applications," *IEEE Transactions on Microwave Theory and Techniques*, vol, 57(10), 2009, pp. 2523 - 2532.
79. A. Beriain, I. Rebollo, I. Fernandez, J. Sevillano, and R. Berenguer, "A Passive UHF RFID Pressure Sensor Tag with a 7.27 bit and 5.47pJ Capacitive Sensor Interface," *Microwave Symposium Digest*. Montreal, Quebec (CA), June 17 - 22, 2012, pp. 1 - 3.
80. A. Beriain, A. Vaz, I. Rebollo, I. Zalbide, J. Sevillano, and R. Berenguer, "Wireless patient monitorization using fully passive devices," *3rd International Symposium on Applied Sciencesin Biomedical and Communication Technologies*. Rome, Italy, November 7 -10, 2010, pp. 1 - 5.
81. S. Lee, J. Hong, C. Hsieh, M. Liang, and J. Kung, "A Low-Power 13.56MHz RF Front-End Circuit for Implantable Biomedical Devices," *IEEE Transactions on Biomedical Circuits and Systems*, vol. 7(3), 2013, pp. 256 - 265.
82. A. Yakovlev, S. Kim, and A. Poon, "Implantable Biomedical Devices: Wireless Powering and Communication," *IEEE Communications Magazine*, vol. 50(4), 2012, pp. 152 - 159.
83. J. Lee, S. Lee, S. Lee, and J. Park, "Wafer Level Packaging for RF MEMS Devices using Void Free Copper Filled Through Glass Via," *IEEE 26th International Conference on MEMS*. Taipei, Taiwan, Jan. 20 - 24, 2013, pp. 773 - 776.
84. H. Greinacher, "The Ionometer and its Application to the Measurement of Radium and Rontgen Rays," *Physikal. Zeitsch.*, vol. 15, 1914, pp. 410 - 415.

85. B. Razavi, “MOS I/V Characteristics,” in *Design of Analog CMOS Integrated Circuits*, New Delhi, Tata McGraw-Hill Publishing Company Limited, 2001, ch. 2, sec. 2, pp. 13 – 23.
86. B. Razavi, “Bandgap References,” in *Design of Analog CMOS Integrated Circuits*, New Delhi, Tata McGraw-Hill Publishing Company Limited, 2001, ch. 11, sec. 2, pp. 377 - 381.
87. A. Hajimiri, and T. Lee, “Design Issues in CMOS Differential LC Oscillators,” *IEEE Journal of Solid State Circuits*, vol. 44(5), 1999, pp. 717 - 724.
88. D. Rutledge, “Oscillators,” in *The Electronics of Radio*, New York, Cambridge University Press, 1999, ch. 11, sec. 1, pp. 204 - 207.
89. S. Mandal, and R. Sarpeshkar, “Low-Power CMOS Rectifier Design for RFID Applications,” *IEEE Transactions on Circuits and Systems*, vol. 54(6), 2007, pp. 1177 - 1188.
90. W. Stutzman, and G. Thiele, “Moment Methods,” in *Antenna Theory and Design*, John Wiley & Sons, Inc., 1981, ch. 7, pp. 306 - 374.
91. J. Osepchuk, and R. Petersen, “Safety standards for Exposure to RF electromagnetic fields,” *IEEE Microw. Mag.*, vol. 2(2), 2001, pp. 57 - 69.
92. K. Kotani, and T. Ito, “High Efficiency CMOS Rectifier with Self-Vth-Cancellation and Power Regulation Functions for UHF RFIDs,” *IEEE Asian Solid-State Circuits Conference*, Jeju, Korea. November 12 - 14, 2007, pp. 119 - 122.
93. K. Keikhosravy, D. Brox, P. Kamalinejad, S. Mirabbasi, and K. Takahata, “An Ultra-Low-Power 35nW Wireless Monitoring System for Biomedical Applications,” under review, 2014.
94. D. Shih, P. Sun, D. Yen, and S. Huang, “Taxonomy and survey of RFID anti-collision protocols,” *Computer Communications*, vol. 29, 2006, pp. 2150 - 2166.
95. N. Pijls, B. de Bruyne, K. Peels, P. van der Voort, H. Bonnier, J. Bartunek, and J. Koolen, “Measurement of fractional flow reserve to measure the functional severity of coronary-artery stenoses,” *The New England Journal of Medicine*, vol. 334(26), 1996, pp. 1703 - 1708.

Appendices

Appendix A
Range Test PCB Design

Schematic diagrams for the Switch and Amplifier PCBs used in single loop antenna tests (Section 4.2.3) are shown in Figs. A.1 and A.2, respectively. The components used in the PCBs, excluding SMA connectors and pins, are listed in Table A.1.

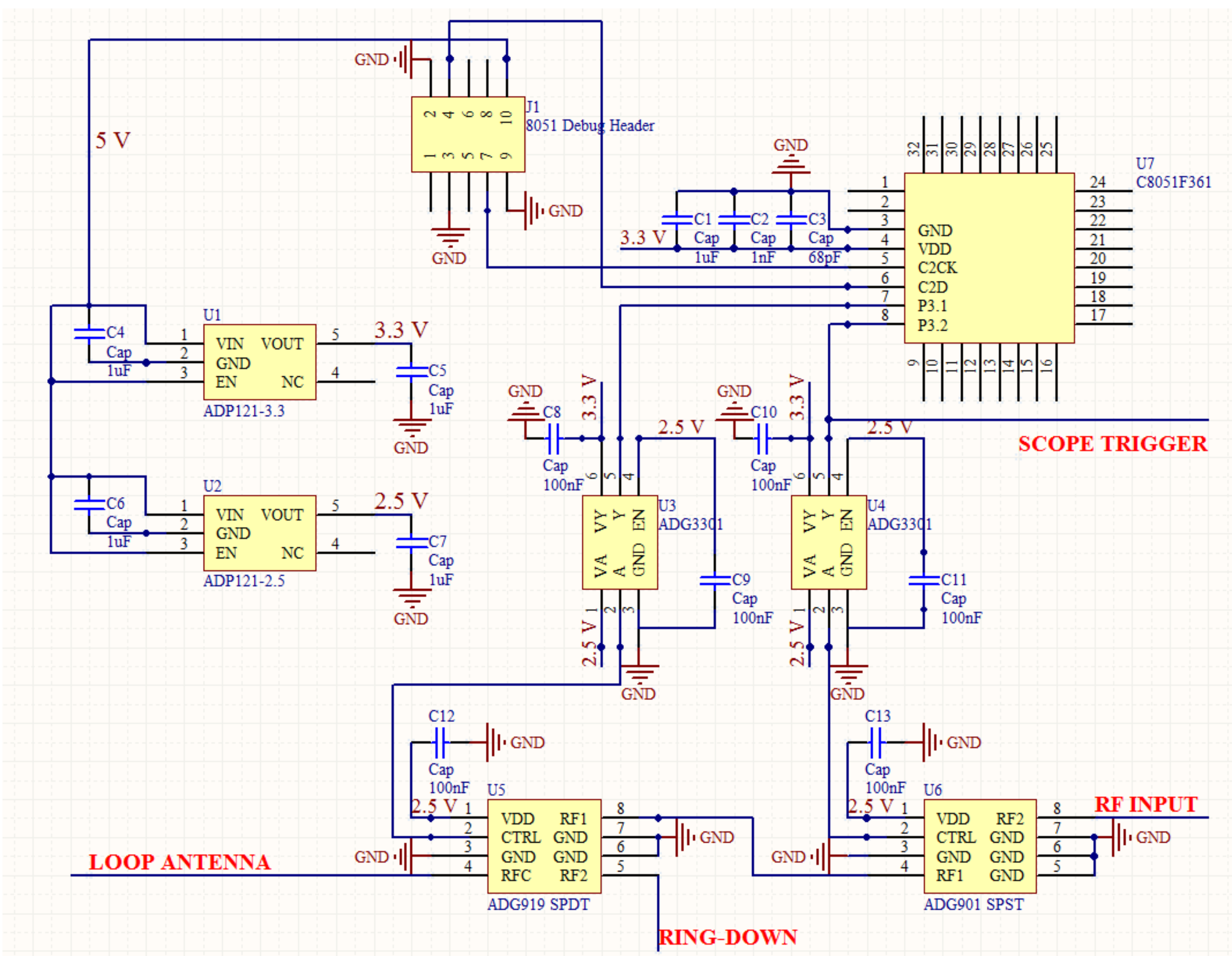

FIGURE A.1: Switch PCB Schematic Diagram

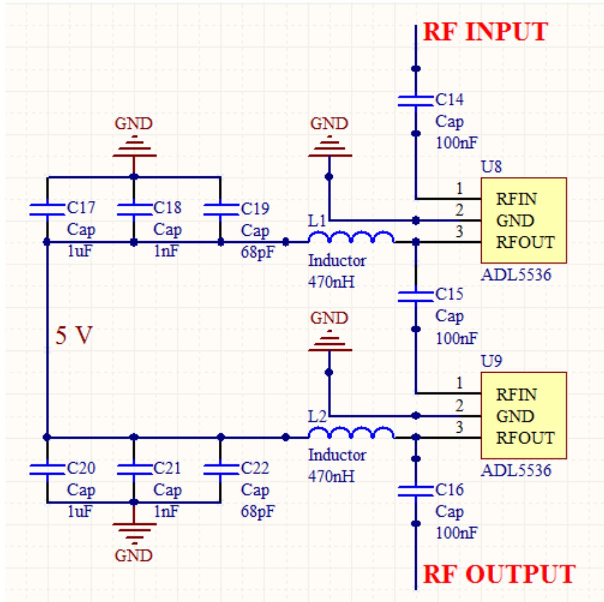

FIGURE A.2: Amplifier PCB Schematic Diagram

TABLE A.1: PCB Components List

Identifier	**Component**
U1	ADP121 Voltage Regulator IC: 5-3.3 V
U2	ADP121 Voltage Regulator IC: 5-2.5 V
U3-4	ADG3301 Level Translator IC
U5	ADG919 SPDT RF Switch IC
U6	ADG901 SPST RF Switch IC
U7	C8051F361 Microcontroller IC
U8-9	ADL5536 20 dB RF Amplifier IC
C1, C4-7, C17, C20	1 µF Surface Mount Capacitor
C8-16	0.1 µF Surface Mount Capacitor
C2, C18, C21	1 nF Surface Mount Capacitor
C3, C19, C22	68 pF Surface Mount Capacitor
L1-2	470 nH Surface Mount Inductor